מכון ויצמן למדע
WEIZMANN INSTITUTE OF SCIENCE

Thesis for the degree
Doctor of Philosophy

עבודת גמר (תזה) לתואר
דוקטור לפילוסופיה

Submitted to the Scientific Council of the
Weizmann Institute of Science
Rehovot, Israel

מוגשת למועצה המדעית של
מכון ויצמן למדע
רחובות, ישראל

By
Yinnon Glickman

מאת
ינון גליקמן

שזירת יון-יון ויון-פוטון במערכת יונים לכודים

Ion-Ion and Ion-Photon Entanglement in Trapped Ions System

Advisor:
Dr. Roee Ozeri

מנחה:
ד"ר רועי עוזרי

August, 2012

אלול, תשע"ב

תקציר

יונים לכודים ממשים מערכת קוונטית המבודדת במידה מרבית מהסביבה והמאופיינת בזמן קוהרנטיות ארוך. יחד עם זאת, מערכות אלו מאפשרות גם שליטה במצבן הקוונטי באמינות גבוהה. לכן, כיום, הן אחת מהפלטפורמות המבטיחות ביותר למימוש מחשבים קוונטיים. עבודה זו חוקרת שני נושאים הנוגעים לעיבוד מידע קוונטי באמצעות יונים לכודים. המשותף לשני נושאים אלו היא שזירה (entanglement) בין המצבים הפנימיים של שתי מערכות קוונטיות. הנושא הראשון שהעבודה דנה בו היא שזירה בין שני מצבים קוונטיים פנימיים של שני יונים לכודים באמצעות שער סורנסון-מולמר (Sorensen-Molmer). השער יושם באמצעות קרן לייזר צרת פס שהופקה על ידי דיודת לייזר. סחיפות איטיות של תדר הדיודה, בשילוב עם רעש פאזה מהיר של האלומה, הגבילו את אמינות השער שהופעל ל-84%. הנושא השני שנדון כאן עוסק בנביעה של בסיס מדידה ביון לכוד המפזר פוטון בודד באופן ספונטני. תהליך זה ממופה באמצעות טומוגרפיית תהליך קוונטית (Quantum Process Tomography). דינמיקת התהליך חושפת קריסה של מצבי ספין היון ל"בסיס מצבי חץ" (pointer state basis). כשהיון מאותחל לאחד מהמצבים הללו ניתן לראות התאמה קלאסית בין מצבו הפנימי למצב קיטוב הפוטון המפוזר. אתחול היון למצב שאינו שייך לבסיס הנ"ל מוביל לשזירה בין מצבו של היון (לאחר תהליך הפיזור) למצב קיטוב הפוטון המפוזר. אנו מראים ששזירה זו קשורה לגדילה באנטרופיה של הספין, כתוצאה מהפיזור, כך שמדובר בתהליך איבוד קוהרנטיות של היון. תהליך זה אינו הפיך.

Abstract

Trapped ions are extremely isolated quantum systems which offer long coherence time combined with high fidelity quantum control. Therefore they are, currently, one of the most promising platforms for realization of quantum computer. This work investigates two issues concerning quantum information processing using trapped ions. The common to these issues is the emergence of entanglement between two quantum parties. The first work was the entanglement of the internal states of two ions by the Sørensen-Mølmer entangling gate. The gate was implemented using a narrow-linewidth diode laser beam. A gate fidelity of 0.84 was achieved, limited by the laser slow frequency drift on one hand and fast phase noise on the other. The second reported work was the observation of a measurement basis emergence in an ion which spontaneously scattered a photon. This process was analyzed by quantum process tomography. The observed dynamics reveals a collapse of the ion spin on a pointer state basis. When initialized to one of these states the ion spin is shown to be in classical correlation with the scattered photon polarization states. Other initial spin states become entangled by the interaction with the scattered photon polarization. We show that this entanglement is related to the increase of spin entropy following scattering, i.e. its irreversible decoherence.

To my wife Danit and our daughter Ruth

Acknowledgments

I would like to thank my supervisor Dr. Roee Ozeri for patiently teaching me the fascinating craft of ions trapping. He introduced me to an exciting world of knowledge and to a world-wide community that is dedicated to this art.

I am grateful for the help I received from my group members: Nitzam Akerman, Shlomi Kotler, Yehonatan Dallal and Anna Kesselman. Their teamwork and support were crucial for the completion of this thesis work. I also received a lot of professional know-how from the people of the Weizmann Institute Faculty of Physics: Dr. Rostyslav Baron, Dr. Michael Rappaport, Yossi Drier, Yeruham Shimoni, Elazar Gershon, Guy Han, Yosef Shopen, David Leibovitz and Benjamin Sharon.

Finally I want to thank my parents Simcha and Yehiel Glickman for the love and support they gave me. Their constant care and involvement in my life has shaped the way I am. In this ongoing journey I'm lucky to have my brothers David and Rei by my side, along with my uncle Yanai and the Gilad dynasty of Mishmar HaEmek.

Contents

List of abbreviations

AOM	Acusto Optical Modulator
BSB	Blue Side Band
BS	Beam Splitter
CF	Con Flat
CNOT	Controlled NOT
CPU	Central Processing Unit
DDS	Direct Digital Synthesizers
DFB	Distributed Feedback
DL	Diode Laser
DFS	Decoherence Free Subspaces
ECDL	External Cavity Diode Laser
EFL	Effective Focal Length
EMCCD	Electron Multiplying Charge Coupled Device
FC	Fiber Collimator
FPGA	Field Programmable Gate Array
FWHM	Full Width Half Maximum
GSC	Ground State Cooling
IR	Infra Red
NEG	Non Evaporable Getters
PBS	Polarizing Beam Splitter
PMT	Photo Multipliers
PPKTP	Periodically Poled KTP
PRU	Polarization Rotation Unit
PSD	Power Spectral Density
QPT	Quantum Process Tomography
QST	Quantum State Tomography
qubit	Quantum Bit
rf	Radio Frequency

RMS	Root Mean Square
RWA	Rotating Wave Approximation
RSB	Red Side Band
SH	Second Harmonic
SHG	Second Harmonic Generation
TAC	Time to Amplitude Converter
TLS	Two Levels System
TSP	Titanium Sublimation Pump
TTL	Transistor Transistor Logic
ULE	Ultra Low Expansion
UV	Ultra Violet
VCO	Voltage Controlled Oscillator

1 Introduction

A research, which is based on highly isolated physical systems, can investigate fundamental mechanisms and interactions in nature. Trapped single ions provide a good platform for this type of research since they are highly isolated from the environment, yet, can be well manipulated and controlled. Internal and motion states of trapped ions can be coherently and readily manipulated and probed using electro-magnetic radiation in the optical or radio-frequency (rf) regimes of the spectrum.

The ability to isolate a single ion and to fix its position in space is the key technology for the field of experimental physics with trapped ions. Two major discoveries made experiments with single trapped ions feasible: the ability to confine ions in an ions-trap and the ability to cool them down by laser cooling. Experiments in trapped ions rely on the ability to spatially confine them for inspection. The devices that are built to do that, namely ions traps, are designed to generate a confining potential for charged particles. This is done by a configuration of electric and magnetic fields that are induced in a specific configuration. The first suggested ion trap was the Kingdon trap [1] in 1923. These days, however, the ions traps that are in popular use are the Paul [2] and Penning [3] traps that were invented correspondingly by Wolfgang Paul and Hans Dehmelt. These traps offer a long life time (up to months) and tight confinement (down to nanometers). The Penning trap is based on a static magnetic field and static quadruple electric field. The Paul trap is about applying a configuration of static and rf oscillating electric fields. The traps are designed to trap an ion with a specific charge-to-mass ratio. In this work we use an rf Pual trap to trap singly ionized Strontium ions.

Laser cooling is a technique for cooling atoms and to localize their motion in space. Laser cooling of trapped atomic ions was suggested [4] and demonstrated [5] by both the Wineland and Dehmelt groups. The basic scheme, which is also known as Doppler cooling, allows cooling of the trapped ions to their Lamb-Dicke regime where they are highly localized with respect to an optical radiation wavelength. With these two technologies researches succeeded to use trapped ions for spectroscopy [6], cooling ions to their ground state of motion [7, 8] and observing quantum jumps [9, 10, 11].

Due to their isolation and long coherence time trapped ions are an appealing platform for quantum computation. The increasing interest in quantum computation followed Peter Shor's discovery of a quantum factoring algorithm in 1994 [12]. This algorithm, when implemented by a quantum computer, allows determination, in a process which scales polynomially with the number size, whether a number is prime. Other quantum algorithms offer efficient database search [13] and simulation of complex physical systems [14]. In 2000 David DiVincenzo listed criteria for the physical realization of quantum computer [15]. He stated that (a) such a computer would have to rely on scalable array of well defined qubits, (b) that it will be possible to initialize this computer to a deterministic state, (c) that this computer will have a coherence time which is much longer then a gate operation time and (d) that it will offer a qubit-specific readout capability. Another criteria which was given is that such a computer will be able to apply a universal gate set to the qubits. It was shown that such a universal set can be composed of single qubit rotations and a two-qubits entangling gate [16]. Single qubit rotations can be directly performed by coupling the two qubit levels with resonant radiation, as is well described in the theory of Two Levels System (TLS) [17].

The first proposal for implementing two-ions entanglement gate, by Cirac and Zoller in 1995 [18], lead to the increasing interest in trapped ions for the purpose of quantum computation. Their proposal for entangling two qubits is based on coupling between two ions internal states through one of their common vibration modes. Following them, in 1999, Sørensen and Mølmer proposed a σ_ϕ entangling phase gate [19] which is based on applying state dependent forces to trapped ions, again, by relaying on a common vibration mode. The Cirac-Zoller gate was implemented by the Blatt group in 2003 [20] with a fidelitiy of 0.71. The Sørensen-Mølmer gate was initially implemented by the NIST group in 2000 [21] with a fidelity of 0.83 and recently in the Blatt group with an astonishing 0.993 fidelity [22]. The recent gate perfomance is bellow the estimated error threshold for fault tolerant quantum computing. That means that, theoretically, quantum gates on trapped ions qubits can be cascaded for a full implementation of a quantum algorithm.

The main obstacle which remains for building a trapped ions based quantum computer regards scalability. Due to limitations of the trapping technology it is infeasible to trap and manipulate large number (grater then 10^2) of ions simultaneously in the same trap. The architecture which is proposed to solve this difficulty are multi trapping-regions structures where ions are stored and manipulated in different locations [23]. In this concept ions are shifted from their storage regions to a joint trapping region (the "processor") where they are manipulated by quantum gates. Several ions can be brought together to the same trapping region for the application of multi-qubit gates. Following gate application the ions are shifted back to their storage locations. This solution performance is limited by the trapped ions heating [24]. All ions traps induce a heating rate on the trapped ions. Shifting the ions between trapping regions worsens this effect. This problem cannot be solved by Doppler cooling or other cooling scheme since they all demolish any coherent state of the ions during cooling. The decoherence mechanism which is applied by the cooling methods is spontaneous scattering of photons by the ions. One possible solution is the sympathetic cooling of logic ions by another species of coolant ions [25].

Decoherence of open systems in general, and particularly due to spontaneous photon scattering, is a fundamental study in the theory of quantum information. By decoherence theory [26] it is suggested that decoherence stems from entanglement of the system and environment states. Entanglement occurs due to system-environment interaction. When the environment is measured the system collapses to a mixed state and its entropy increases. Observation of progressive decoherence of the measurement apparatus in quantum measurement, due to interaction between system and environment, was observed in atoms and a microwave cavity [27]. By this model decoherence can be related to the emergence of classicality in macroscopic bodies. Not all the system states decohere due to interaction with the environment. There are system states that are correlated with the environment but are not entangled with it. These states were predicted by Zurek [28] in 1981, they are referred to as the system pointer states. These states are determined by the interaction with the environment in a process which is called einselection, they remain pure under the measurement of the environment.

Related entities that remain unaffected by interaction with an environment are Decoherence Free Subspaces (DFS). These subspaces are spanned by states that are eigenstates of an operator which commutes with the applied environment interaction Hamiltonian. Encoding qubits information in these spaces was shown to be effective in increasing their coherence time drastically [29, 30].

In this work section 2 gives a brief theoretical introduction to the basic aspects of trapping and manipulating single ions. Section 3 describes the components of the experimental apparatus that were used for this work. Section 4 describes the basic techniques that are used for establishing qubits in trapped ions. Section 5 describes our implementation of two qubits entangling gate using a narrowed linewidth diode-laser optical beam. Section 6 describes our observation of a measurement basis emerging when a single qubit spontaneously scatters a photon.

2 Theory

In this section the theoretical foundations of ions trapping and manipulation are discussed. The mechanism of a linear Paul trap, which is the core technology in our experiment, is briefly reviewed. Quantum information studies, in the context of this work, deal with the trapped ion valence-electron states. Manipulation of the electronic population between these states is done by introducing electro-magnetic radiation to the ion. This coupling is analyzed in analogy to the interaction between a two-states spin and an oscillating resonant magnetic field. This interaction results in a set of coherent population manipulation tools.

2.1 Ions trapping by a linear Paul trap

Ion traps are devices for trapping single ions. Unlike optical atomic traps, these devices apply forces on the ions' charge by applying a configuration of electric voltages for confinement. It can be shown, by the Laplace equation, that a single static electric potential cannot confine in all the three dimensions, simultaneously. This can be demonstrated by considering a trivial electric potential $\Phi\left(x,y,z\right)=Ax^2+By^2+Cz^2$. This potential is supposed to apply a returning force on a charged particle for any direction displacement from equilibrium. However, by applying the Laplace law on Φ: $\nabla\vec{E}=-\nabla^2\Phi=-2A-2B-2C=0$ it can be seen that, to fulfill this law, at least one of the A,B,C coefficients is required to be negative. Hence, Φ cannot confine a charged particle, simultaneously, in all the three dimensions.

In a linear rf Paul trap [2] a trapped ions string is aligned along a line - the trap axis $\hat{z}_t$. In this trap the three dimensional confining potential is generated by a superposition of two confining potentials:

1. A static longitudinal potential along the trap axis.
2. A quadrupole oscillating potential in the trap transverse plane (the $\hat{x}_t-\hat{y}_t$ plane).

A generic design of a linear Paul trap is shown in Fig.1. The static potential is achieved by applying a common voltage U_0 on the end-caps electrodes. These electrodes reside on the $\hat{z}_t$ axis, one from each side of the trapping region. The spatial potential which they induce is:

$$\Phi_{DC}(x,y,z)=\kappa U_0\left(z^2-\frac{1}{2}(x^2+y^2)\right)=\frac{1}{2e}m\omega_z^2\left(z^2-\frac{1}{2}(x^2+y^2)\right), \qquad (2.1.1)$$

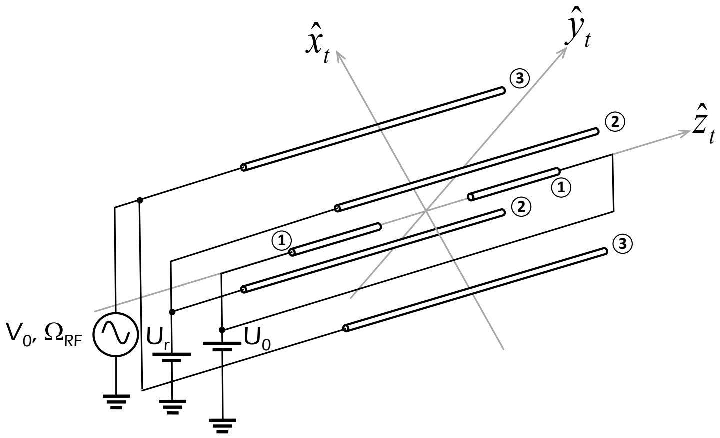

Figure 1: Schematic diagram of a linear rf Paul trap. Axial confinement is provided by the trap end-caps (1). Applying higher DC potential to the end-caps, relative to the DC electrodes (2), provides a potential minimum along the trap axis. An oscillating potential is applied to the rf electrodes (3) producing an approximate quadrupole electric field pattern in the $\hat{x}_t - \hat{y}_t$ plane. This provides radial confinement of the ions to the rf electric field null along the $\hat{z}_t$ axis. Stronger radial confinement then an axial leads to ions alignment along the trap axis.

where, κ is a geometrical parameter, e is the electron charge, m is the trapped ion mass and x,y,z are the coordinates along the corresponding trap axes. For $U_0 > 0$, Φ_{DC} is a trapping potential along the trap axis and a repealing potential along the transverse plane. It is responsible for trapping ions along the axial direction with and harmonic oscillation frequency of $\omega_z = \sqrt{2e\kappa U_0/m}$. The anti-confinement of Φ_{DC} in the transverse plane is compensated by the applied quadrupole oscillating potential.

The quadruple potential is generated by the trap four electrodes, that are arranged in a quadrupolar configuration, parallel to $\hat{z}_t$. Two opposite electrodes, out of the four, are biased by a constant voltage U_r above the ground. The other two electrodes are driven by an oscillating voltage: $V_0\cos(\Omega_{RF}t)$, where, V_0 and Ω_{RF} are the oscillating voltage amplitude and frequency. U_r is introduced, as we shell see, to remove the degeneracy between the ion frequencies along the $\hat{x}_t$ and $\hat{y}_t$ axes. This yields the oscillating electric potential,

$$\Phi_{RF}(x,y,z) = \frac{1}{2}\kappa_{RF}\left(V_0\cos(\Omega_{RF}t) + U_r\right)\left(1 + \frac{x^2 - y^2}{R^2}\right), \tag{2.1.2}$$

where, κ_{RF} is a geometrical factor and R is an electrode distance from $\hat{z}_t$. The equation of motion in the transverse plane is dictated by the derived electric fields forces of Φ_{DC} and Φ_{RF}:

$$\ddot{x}_i = -\frac{e}{m}\frac{\partial}{\partial x_i}\left(\Phi_{DC} + \Phi_{RF}\right), \qquad i \in \{x, y\}. \tag{2.1.3}$$

These equations can be written in the form of homogenous differential equations of the Mathieu [31] type:

$$\frac{d^2 x_i}{d\tau^2} + \left(a_i + 2q_i \cos(2\tau)\right) x_i = 0. \tag{2.1.4}$$

The normalized parameters in the equation manifest physical properties of the ion trap: $\tau = \Omega_{RF} t/2$ is a dimensionless time, the a_i's quantify the static trap potentials and the q_i's measure the rf potential strength. They are written as:

$$\begin{aligned}
a_x &= -\frac{4e}{m\Omega_{RF}^2}\left(\kappa U_0 - \frac{\kappa_{RF} U_r}{R^2}\right), \\
a_y &= -\frac{4e}{m\Omega_{RF}^2}\left(\kappa U_0 + \frac{\kappa_{RF} U_r}{R^2}\right), \\
q_x &= -q_y = \frac{2e\kappa_{RF} V_0}{m\Omega_{RF}^2 R^2}.
\end{aligned}$$

Note that for breaking the degeneracy among the motions in the $\hat{x}_t$ and $\hat{y}_t$ directions a $U_r \neq 0$ is needed. A general solution of the Mathieu equation can be achieved by using the Floquet theorem [32]. Trapping of an ion in the transverse plane is possible when the solutions to the two Mathieu equations are stable. These solutions emerge for a and q parameters pair that are in the stable regions of Fig. 2. Under the assumption that $a, q \ll 1$ the solutions can be well approximated, to the lowest order, by:

$$\begin{aligned}
x_i(t) &= x_i^0 \cos(\omega_i t + \phi_i)\left(1 + \frac{q_i}{2}\cos(\Omega_{RF} t)\right) \\
&= x_i^0 \cos(\omega_i t + \phi_i) + \frac{x_i^0 q_i}{2}\cos(\omega_i t + \phi_i)\cos(\Omega_{RF} t).
\end{aligned} \tag{2.1.5}$$

This expression describes, reliably, the ion motion in the trap transverse plane. The first term describes the trapped ion secular motion with an amplitude x_i^0, phase ϕ_i and frequency $\omega_i = (1/2)\Omega_{RF}\sqrt{a_i + q_i^2/2}$, which, is much smaller the the trap rf drive frequency. Practically speaking, the extent of the ions motion about their equilibrium positions is on the order of a few tens of nanometers. The second term of (2.1.5) describes the trapped ion micromotion. This motion amplitude is smaller, by $q_i/2$, relative to the secular motion. Therefore, it is proportional to the

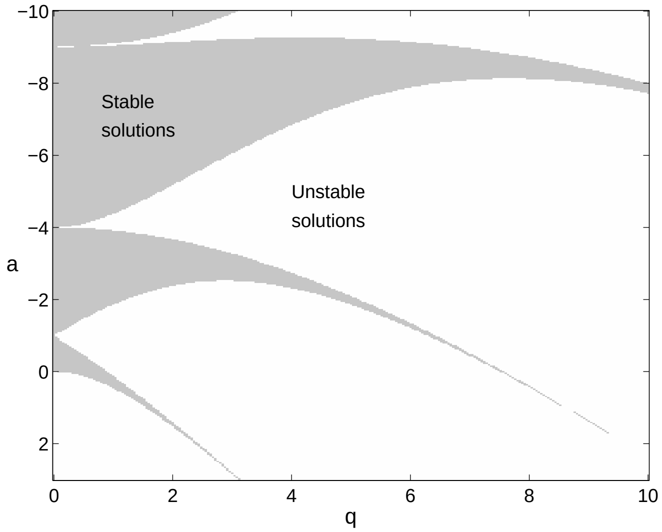

Figure 2: Taken from [33]. Stability diagram of the Mathieu equation. Shaded areas stand for parameter values that lead to stable, bounded, solutions. Usually traps parameters are selected to reside in the two lowest stable regions (along the a axis).

ions distance from the trap center. Micromotion vibrations are faster than the ion secular motion. Usually, single-trapped-ions experiments are harmed by the presence of micromotion as it introduces unwanted Doppler shifts. The common causes to micromotion are stray electric fields that arise, for example, from dielectric charged materials in the vicinity of the trapping region. These fields deflect the trapped ions equilibrium position from the trap rf null to a location where the driving frequency oscillations don't cancel. Minimizing micromotion is done by applying DC potentials for compensation. It is done by biasing the rf voltage U_r, applying a differential voltage between the trap end-caps and raising the grounded electrodes voltage.

Overall, the trap generates an harmonic pseudo-potential to trap an ion. This potential is of the form:

$$V = \frac{1}{2} m \sum_j \omega_j^2 x_j^2, \qquad j \in \{x, y, z\}, \tag{2.1.6}$$

where, ω_j are the trapped ion oscillation frequencies in the axial and transverse axes. In a linear Paul trap, a trapping depth of few eV can be easily achieved, allowing for the trapping of ions from an atomic hot jet. The ratio between the secular frequencies ω_x and ω_y can be changed by varying the static potential U_r. It is imperative to maintain all secular frequencies of the trap non-degenerate to simplify the ions normal oscillation modes and for the effectiveness of Doppler-cooling. In practice, the axial trap frequency ω_z is kept lower than the transverse secular frequencies to align several trapped ions along $\hat{z}_t$.

2.2 Doppler cooling to the Lamb-Dicke regime

Coherent manipulation of ions with laser radiation requires cooling to the Lamb-Dicke regime, in which the ion motion is bound to a size smaller than the radiation wavelength. As a result, trapped ions does not "feel" gradients of the laser field and momentum is not transferred from an absorbed photon to the ion. Instead, in this regime, the momentum is transferred to the trap, which is a macroscopic structure that remains unaffected by photon absorption. Ions that are trapped from a hot thermal jet are tremendously hot. Their energy is manifested to high mean level occupation numbers ($\bar{n}_j$). Following trapping $\bar{n}_j$ is of the order of 10^8. As is elaborated in the next section, ions in this state are far from being in an optical-radiation Lamb-Dikie regime and therefore are not fit for coherent interactions.

Trapped ions laser cooling [34] is done by scattering photons with frequency which is red-detuned relative to an allowed optical transition. In the case where the trap oscillation frequency ω_j is smaller than the transition linewidth Γ the period of the ions center-of-mass oscillation is larger then the optical decay time. Considering an ion motions as classical, with a velocity $v(t) = v_0 \cos(\omega t)$, it behaves like a free particle seeing time-dependent Doppler-shifted laser frequency. The corresponding radiation pressure force on the ion is:

$$F = \frac{\hbar k \Gamma \Omega^2}{(\Delta - kv(t))^2 + \Gamma^2}, \tag{2.2.1}$$

where, k is the radiation k-vector magnitude, Ω is the transitions Rabi frequency and Δ is the radiation detuning from the transition frequency. If the detuning is such that transition occurs preferentially when the motion is towards the source of radiation (where $\Delta > 0$) the ion loses a recoil velocity ($\hbar k/m$) on the average every time a photon is scattered. Hence, the velocity-dependent radiation pressure can provide cooling, called Doppler cooling. Unlike the case of cooling neutral atoms, tapped ions Doppler cooling can be preformed by shining a single laser beam [35] on the ions. This beam k-vector is required to have components on all the trap major axes.

The Doppler cooling is physically bounded by uncorrelated spontaneous emission events. For cooling using scattering photons on the ion dipole transition the minimal temperature to which the ion can reach is [36]:

$$T_{min} = \frac{7\hbar\Gamma}{20k_B}, \tag{2.2.2}$$

where k_B is the Boltzmann constant. This temperature can be translated to an oscillator mean occupation number by assuming a Maxwell-Boltzmann distribution for the harmonic oscillator levels. By this distribution the probability of a particle to posses the oscillator energy n is:

$$p_{n_j} = \frac{1}{\sum p_{n_j}} e^{-\frac{\hbar\omega_j n_j}{k_B T}} = \frac{1}{\bar{n}_j + 1}\left(\frac{\bar{n}_j}{\bar{n}_j + 1}\right)^{n_j}, \tag{2.2.3}$$

where, $\bar{n}_j$ is equal to:

$$\bar{n}_j = \frac{1}{e^{\frac{\hbar\omega_j}{k_B T}} - 1} = \frac{1}{e^{\frac{20\omega_j}{7\Gamma}} - 1}. \tag{2.2.4}$$

On typical systems Doppler cooling reduces the mean level occupation number to $\bar{n}_j \simeq 10$. Further cooling, by resolved sideband ground state cooling, can reduce $\bar{n}_j$ by two orders of magnitude, as will be shown in section (4.7).

2.3 Coherent interaction with cold trapped ions

Ions are composite quantum systems. Their electronic population can be distributed among many states, each featured by its own quantum numbers and energy. The discipline of exploiting trapped ions, as platforms for quantum information studies, seeks to simplify the dealing with those systems while maintaining their quantum nature. One step in this direction is achieved by working with ions that belong to the group of alkaline earth metals. This group, listed in possess the second column of the periodic table have two electrons in their outer most shell. When one of these elements is singly ionized it is left with a single valence electron which makes it resemble the Hydrogen atom. Such an ion has a relatively simple electronic energy levels structure which is accessible with coherent radiation sources such as lasers. Interaction between coherent electro-magnetic radiation and the valence electron is treated by the elegant theory of quantum TLS [17]. The electron two states that match the radiation photon energy can be designated as $|\uparrow\rangle$ and $|\downarrow\rangle$ by analogy with spin-1/2 systems. While internal states of the ion are represented as a superposition of these states, a more comprehensive description of the ion wavefunction also includes its external degrees of freedom, i.e. its vibrational states. Though, as can be seen in equation 2.1.6, a single trapped ion vibrates in three modes, here we consider a single vibration mode only (for example, the longitudinal vibration mode). Therefore, a general ion time-dependent wavefunction can be expressed as:

$$|\Psi(t)\rangle = \sum_{n=0}^{\infty} \left(a_{\uparrow,n}(t)|\uparrow\rangle + a_{\downarrow,n}(t)|\downarrow\rangle\right)|n\rangle, \tag{2.3.1}$$

where, $a_{\uparrow,n}(t)$ and $a_{\downarrow,n}(t)$ are the amplitudes of the $|\uparrow\rangle$ and $|\downarrow\rangle$ states, respectively, with a vibration mode occupation number n. In the absence of interaction with radiation $|\Psi\rangle$ is the eigenfunction of the Hamiltonian:

$$H_0 = \frac{\hbar\omega_0}{2}\sigma_z + \hbar\omega_1(a^\dagger a + \frac{1}{2}), \tag{2.3.2}$$

where, $\hbar\omega_0$ is the energy spacing between the $|\uparrow\rangle$ and $|\downarrow\rangle$ states, ω_1 is the vibration mode frequency and $a^\dagger$, a are the harmonics oscillator raising and lowering operators, respectively.

Coherent interaction between an ion and electro-magnetic radiation is a prime tool for manipulating ion intrinsic electronic population and external degrees-of-freedom. The coupling between internal ion states and the radiation (for dipole transitions) is by the electric dipole Hamiltonian $H_{dip} = -\boldsymbol{d}\cdot\boldsymbol{E}$, where, $\mathbf{d}$ is the transition electric dipole operator and $\mathbf{E}$ is the radiation electric field. In analogy with spin 1/2 systems, this interaction is modeled as a spin under an oscillating magnetic field. The field is considered to be polarized perpendicularly to the quantization axis. In this model, the interaction Hamiltonian is written as:

$$H_1(t) = -\boldsymbol{\mu}\cdot\boldsymbol{B} = -\boldsymbol{\mu}\cdot\boldsymbol{\varepsilon}B_0 cos(\boldsymbol{k}\cdot\boldsymbol{z} - \omega_l t + \phi), \tag{2.3.3}$$

were, $\mathbf{B}$ is a magnetic field, propagating with the k-vector $\mathbf{k}$ at frequency ω_l, phase ϕ and polarization $\boldsymbol{\varepsilon}$. $\boldsymbol{\mu}$ is a fictitious magnetic moment ($\boldsymbol{\mu} = \mu_m\boldsymbol{S}$) which manifest the dipole interaction strength. It should be noted that here $\boldsymbol{z}$ stands for the ion displacement from its point of equilibrium in the trapping potential. The product $\boldsymbol{S}\cdot\boldsymbol{\varepsilon} = S_x \propto S_+ + S_-$. H_1 can be written as:

$$H_1 = \Omega\left(S_+ + S_-\right)\left(e^{i(\boldsymbol{kz}-\omega_l t+\phi)} + h.c.\right), \tag{2.3.4}$$

where, Ω is the coupling strength between the radiation and the ion. By writing the scalar product $\boldsymbol{k}\cdot\boldsymbol{z}$ in term of a and $a^\dagger$ we get $\boldsymbol{k}\cdot\boldsymbol{z} = \boldsymbol{k}\cdot\hat{z}_t z_0(a + a^\dagger) = \eta(a + a^\dagger)$, where, z_0 is the ions wavefunction spread at the ground level of the axial oscillation mode, for example. η is the Lamb-Dicke parameter which is defined as $\eta = k\cos(\theta)\sqrt{\hbar/2m\omega_1}$, where, $\theta = \cos^{-1}(\hat{\boldsymbol{k}}\cdot\hat{z}_t)$ is the angle between the radiation k-vector and the axis of vibration. This parameter quantifies the momentum of the incident radiation photons relative to ion trapping strength by the trap. The smaller this parameter is the more momentum, following photon absorption, will be transferred to the trap and less momentum will be translated to change in the ion vibrational level. The Lamb-Dicke scales as the radiation frequency making rf radiation almost incapable of changing an ion vibrational state. Using the Rotating Wave Approximation (RWA) H_1 can be written as:

$$H_1 = \hbar\Omega \left(e^{i\eta(a+a^{+})} S_+ e^{-i\omega_l t} + h.c. \right). \tag{2.3.5}$$

This Hamiltonian can be represented in the interaction picture as $H_I = UHU^{\dagger}$, where, $U = e^{(iH_0 t/\hbar)}$, as:

$$H_I = \frac{1}{2}\hbar\Omega \left(e^{i\eta(ae^{i\omega_1 t}+a^{\dagger}e^{-i\omega_1 t})} S_+ e^{-i(\delta t+\phi)} + h.c. \right), \tag{2.3.6}$$

where, $\delta = \omega_l - \omega_0$. We work in the Lamb-Dicke regime where $\eta^2(2n+1) \ll 1$. In this regime the extension of the ions wavefunction is much smaller then the applied wavelength. When the Lamb-Dicke criteria is met we aproximate $e^{i\eta(ae^{i\omega_1 t}+a^{\dagger}e^{-i\omega_1 t})} \simeq 1 + i\eta(ae^{i\omega_1 t} + a^{\dagger}e^{-i\omega_1 t})$. Hence, H_I can be decomposed to three terms:

$$H_I = H_I^{(c)} + H_I^{(RSB)} + H_I^{(BSB)}, \tag{2.3.7}$$

where each term describes spin 1/2 flipping with different influence on the vibration-mode occupation n. The effective Rabi frequency $\Omega_{n,n'}$ is a product of the free Rabi frequency and the Debye-Waller factor as

$$\Omega_{n,n'} \equiv \Omega |\langle n' | e^{i\eta(a+a^{\dagger})} | n \rangle|. \tag{2.3.8}$$

In details, the terms are:

1. $H_I^{(c)} = \hbar\Omega_{n,n}/2 \left(S_+ e^{-i(\delta t+\phi)} + h.c. \right)$ is the carrier transition Hamiltonian. For $\delta = 0$ ($\omega_l = \omega_1$) it describes a coherent population transfer between states without changing their vibration energy level ($|\downarrow, n\rangle \leftrightarrow |\uparrow, n\rangle$). This transition Rabi frequency depends on the states vibrational number as $\Omega_{n,n} = \Omega(1 - \eta^2 n)$.

2. $H_I^{(RSB)} = \hbar\Omega_{n,n-1}/2 \left(aS_+ e^{-i((\delta+\omega_1)t+\phi)} + h.c. \right)$ is a Jaynes-Cummings red-sideband transition Hamiltonian. For $\delta = -\omega_1$ ($\omega_l = \omega_0 - \omega_1$) it describes spin raising while removing a phonon ($|\downarrow, n\rangle \leftrightarrow |\uparrow, n-1\rangle$) and vice versa. This transition Rabi frequency is $\Omega_{n,n-1} = \eta\sqrt{n}\Omega$, it is used for cooling the ion to the trap ground-state as will be discussed in section (4.7).

3. $H_I^{(BSB)} = \hbar\Omega_{n,n+1}/2 \left(a^{\dagger} S_+ e^{-i((\delta-\omega_1)t+\phi)} + h.c. \right)$ is an anti-JaynesCummings blue-sideband transition Hamiltonian. For $\delta = \omega_1$ ($\omega_l = \omega_0 + \omega_1$) it describes both raising of the spin and

the vibration level ($|\downarrow, n\rangle \leftrightarrow |\uparrow, n+1\rangle$) and vice versa. This transition Rabi frequency is $\Omega_{n,n+1} = \eta\sqrt{n+1}\Omega$.

The carrier Hamiltonian, once applied on the wavefunction $|\Psi\rangle$, For the carrier transition, the $a_{\uparrow,n}$ and $a_{\downarrow,n}$ obey the differential equation (at $n = 0$):

$$\begin{aligned} \dot{a}_{\uparrow,n} &= -i\Omega e^{-i\delta t+\phi} a_{\downarrow,n} \\ \dot{a}_{\downarrow,n} &= -i\Omega e^{i\delta t+\phi} a_{\uparrow,n}. \end{aligned} \tag{2.3.9}$$

For on-resonance coupling ($\delta = 0$) this interaction can be presented with the time-evolution operator $U(t)$, where, $|\Psi(t)\rangle = U(t)|\Psi(0)\rangle$ can be written, in the $\{a_{\uparrow,n}, a_{\downarrow,n}\}$ basis, as:

$$U(t) = \left(\begin{array}{cc} \cos\left(\frac{\Omega t}{2}\right) & -ie^{-i\phi}\sin\left(\frac{\Omega t}{2}\right) \\ -ie^{i\phi}\sin\left(\frac{\Omega t}{2}\right) & \cos\left(\frac{\Omega t}{2}\right) \end{array} \right) = R(\Omega t, \phi), \tag{2.3.10}$$

where, $R(\Omega t, \phi)$ is a rotation matrix of a spin Bloch vector $\boldsymbol{\rho}$. It is defined as:

$$\rho_x = a^*_{\uparrow,n} a_{\downarrow,n} + a_{\uparrow,n} a^*_{\downarrow,n}, \qquad \rho_y = i(a_{\uparrow,n} a^*_{\downarrow,n} - a^*_{\uparrow,n} a_{\downarrow,n}), \qquad \rho_z = |a_{\uparrow,n}|^2 - |a_{\downarrow,n}|^2. \tag{2.3.11}$$

On-resonance rotation is done by an angle Ωt around an axis which lies on the Bloch sphere equator and tilted by ϕ relative to the sphere x axis, as can be seen in Fig. 3. Similar rotations can be preformed by the red and blue sidebands coupling to the radiation. In these cases the spin state (the Bloch vector) rotation will be accompanied with phonon absorption and emission.

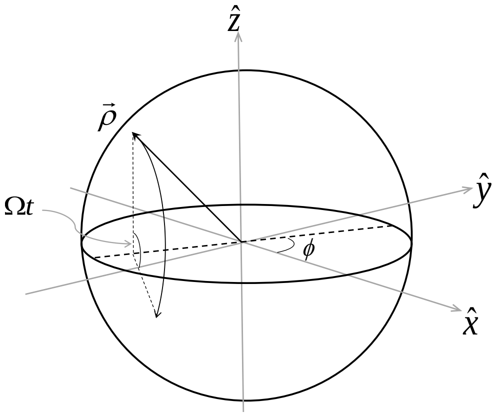

Figure 3: The Blcoh vector, representing the spin 1/2 state, which is the analogy for the two levels that are coupled by electro-magnetic radiation. Applying a resonant field rotates the vector around an axis which resides on the sphere equator. The rotation angle is set by the coupling strength (the Rabi frequency Ω) and the exposure duration t.

3 Experimental Apparatus

This chapter gives a comprehensive description of the building and the structure of the experimental setup with which the work described in this thesis was performed. For ^{88}Sr atom and ^{88}Sr^{+} ion, all the required beam wavelengths can be generated by diode lasers. This simplifies and reduces the size of the setup design.

The experimental setup is constructed on two optical tables in a, temperature and humidity stabilized, lab. The first optical table hosts the vacuum chamber that encapsulated the ions trap, its pumps and vacuum components, the imaging system and the magnetic field regulation systems. The second optical table hosts the lasers and their frequency stabilization optical and electrical circuits. Laser beams are guided by optical fibers from the lasers table to the trap table. Both optical tables ”float” on pneumatic dampers for passive vibrations isolation.

3.1 Atomic Structure

Strontium (Sr) is an alkali earth element. Once it is singly ionized, a Sr^{+} ion is left with a single valence electron. Therefore, its energy level structure is similar to that of neutral alkali atoms including the Hydrogen atom. The ^{88}Sr isotope has no nuclear spin and therefore no hyperfine energy levels structure.

Figure 4 shows a scheme of the three lowest energy levels of the valence electron states. The electron ground state is an S-orbital. This state has a Landé factor $g_J = 2$, its Zeeman manifold (the $m_J = \pm 1/2$ states) splits under magnetic field by $2\mu_B = 2.8$ MHz/Gauss. The lowest excited state is the D-orbital with the two metastable states $4d^2D_{3/2}$ and $4d^2D_{5/2}$ that have a mean life time of 0.44 sec and 0.38 sec, respectively. The second excited state is a P-orbital. This state can be coupled to the ground state using electromagnetic radiation via the electric dipole moment. The $5P_{1/2}$ life time is 7.4 nsec and it has a corresponding spectral line-width of $\Gamma/2\pi = 21.5$ Mhz. Under a small magnetic field of few Gauss this line-width is larger then the ground state Zeeman splitting. decay from the $5p^2P_{1/2}$ and $5p^2P_{3/2}$ states has a branching ratio of 1:14 of decaying to the D levels or the $S_{1/2}$ ground state.

3.2 The Ion trap

The ion-trap is a linear Paul trap [37]. It is constructed of four conducting cylindrical parallel electrodes that are arranged in a quadrupolar configuration, as can be seen in Fig. 5(a). The electrodes are made of tungsten and are 0.3 mm in diameter. The end-caps are two electrodes that are mounted along the trap longitudinal axis, between the four quadrupole electrodes, separated by 1.3 mm. Two more electrodes run bellow the trap. The first electrode functions as an antenna for radiating rf fields in the trap (the rf electrode). The second electrode is used to compensate for stray static electric fields (micromotion compensation) by applying a DC voltage on it. All the electrodes are mounted and supported by four laser-machined alumina wafers that keep them parallel in a constant distance from each other. The center of two neighboring electrodes are separated by 0.6 mm.

Two diagonal opposite electrodes, of the quadrupolar four, are kept at a constant voltage while the other two opposite electrodes are connected to an oscillating (21 MHz) rf source. These electrodes are driven through a helical rf resonator ($Q \sim 70$), which amplifies the supplied rf voltage. The trap consumes less then 1 W power. With this power the radial oscillation frequencies in the trap ,ω_x and ω_y, are roughly 2.5 MHz and 2.35 MHz, respectively. The trap longitudinal oscillation frequency is $\omega_z = 1$ MHz with an end-caps common voltage of $U_0 = 50$ V. The trap pseudo-potential nonlinearity was characterized. This potential generates a cubic force $F_{nl} = \alpha_{NL} z^3$ along the trap

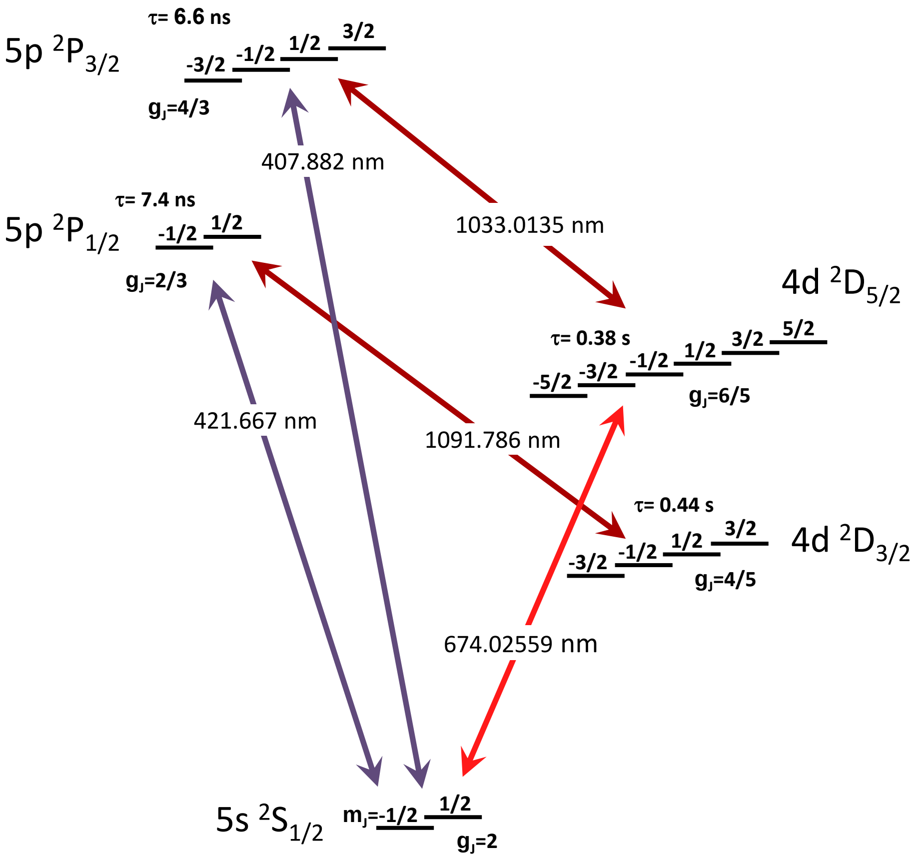

Figure 4: The valence electron states of the ^{88}Sr$^+$ ion. This isotope has no nuclear spin and therefore no hyperfine states structure. The arrows specify the addressed transition wavelength.

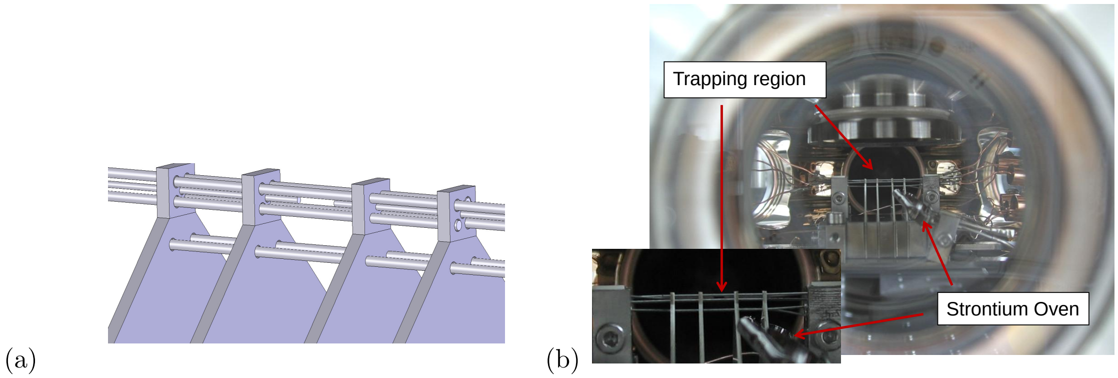

Figure 5: (a) A sketch of our linear Paul trap. The trap is made of six tungsten rods held by four laser-machined alumina wafers. The ions trapping zone is in the gap between the two end-caps in the trap center. (b) An image of the trap and its surroundings, taken through one of the vacuum chamber optical ports. In the figure and the inset one can spot the trap electrodes, the trapping region and the Strontium ovens.

$\hat{z}_t$ axis. The parameter α was measured to be $\alpha_{NL} = 1.24 \pm 0.03 \cdot 10^18Hz^2/m^2$ [38]. The trap heating rate was measured to be $\dot{\bar{n}}_z = 0.0158/msec$ for the trap axial vibration mode, as is elaborated in section 4.7.

The ^{88}Sr^{+} ions are loaded into the trap by photo-ionization of neutral Strontium atoms, as can be seen in Fig 5(b). Grains of Strontium are encapsulated in ovens tubes that are directed toward the trapping region. Driving a 2 A current through these tubes evaporates a jet of hot Strontium atoms to the trap. There are two Strontium ovens in the vacuum chamber. During the loading sequence, only one oven is heated.

3.3 The vacuum vessel

The ion trap is mounted inside a vacuum vessel in an Ultra High Vacuum (UHV) environment. This tremendously low pressure is crucial for keeping the ions trapped for long periods of time. As the probability for ions to escape due to a collision with background gas molecules is negligible (due to the trap depth relative to the kinetic energy of background gas). Ions can however be lost by chemical re-combination with background molecules. The prime candidates for that are Hydrogen molecules that have a large cross section for re-combination with the Strontium ions.

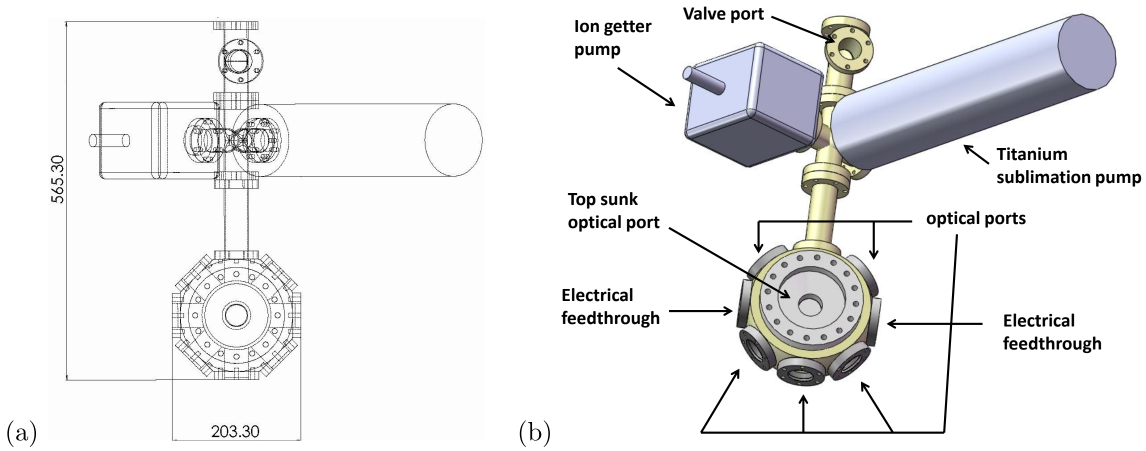

Figure 6: Top- (a) and tilted (b) views of the vacuum vessel. Units are in mm. The TSP is roughly represented by a cylinder with the same dimensions. A valve was fitted to the valve port. It allowed rough pumping of the vessel by the turbo pump and unplugging it once the process was utilized.

The vacuum vessel core, as can be seen in Fig. 6, is an octagon shaped vacuum chamber made of stainless-steel (Kimball physics MCF600-SphOct-F2C8). It has 2.75 Inch Conflat (CF) port in each one of its eight circumferential faces. Two 6 inch CF ports reside on the chamber top and bottom faces. The top port hosts a costume-made sunk optical window for observing, by the imaging system (section 3.4), the trapped ions. The bottom port is sealed. One of the eight circumferential ports is used for pumping, two other are used for electrical feedthroughs and the other five are used as optical windows for beams transmission into the trap. The pumping port serves as a junction for three pumps:

1. A turbo pump (Varian Mini-Task) for reducing the vessel air pressure from one atmosphere to $\sim 10^{-8}$ Torr. This pump is connected to the vessel through a valve. The valve allows for the removal of the pump once it has reached its threshold.
2. A 20 L/S ion getter pump (Varian Vaclon Plus 20).
3. A Titanium Sublimation Pump (TSP).

In addition, stripes of Non-Evaporable Getters (NEG) (SAES St707) where attached to the chamber floor. These getters are especially efficient in absorbing residual Hydrogen molecules.

The sequence of depressurizing the vacuum vessel begins by rough pumping of its atmosphere by the turbo pump. As the air pressure reached to 10^{-8} torr the pump valve was closed and the pump was disattached. The vessel was backed at a temperature of 200 °C for two weeks. Baking accelerated out-gasing of the chamber walls and content. The ion pump was kept running during baking. At the end of the bake-out, and cooling back to room temperature, the chamber vapors pressure reached 10^{-10} Torr. The TSP and NEG were activated to absorb residual gases. After several days of combined ion pump, TSP and NEG operation the pressure in the chamber dropped to below our vacuum gauge baseline at 8×10^{-12} Torr.

3.4 The Imaging system

The imaging system functions both as a microscope (for monitoring ion crystals during the loading stage) and as a photon counter. The system is mounted above the vacuum chamber on an optically sealed breadboard. Scattered photons fluorescence is collected by an objective lens (NA=0.3) which is focused on the trapped ions. The objective lens is positioned outside the vacuum chamber which creates two difficulties. Firstly, a working distance of a few cm is forced; a relatively long distance for this NA. Secondly, the vacuum chamber optical window introduces spherical aberrations. The objective was designed [39] and manufactured (LENS-Optics) to correct for spherical aberrations of the optical port as well as those of the objective lenses themselves. Figure 7 shows section views of the objective structure. It was designed to collimate 422 nm photons, scattered by the $5s^2S_{1/2} \rightarrow 5p^2P_{1/2}$ ion transition. The design process itself, as can be seen, was made in a reverse order by trying to minimize the abberations of focusing a collimated beam (a planar wavefront) through the optical port window. The objective has an Effective Focal Length (EFL) of 25 mm and is made of 1 inch diameter lenses. It is diffraction limited to an Airy disc diameter, at the focal plane, of 0.8 μm. All the objective lenses were made of standard BK7 glass with surface scratch-dig quality of 20-10. Table 1 specifies the dimensions of the objective optical surfaces. The distances between the lenses were iterated to minimize the objective overall spherical abberations up to the 7^{th} order.

The second part of the imaging system includes a magnification optics, polarization analysis components and detectors. These are encapsulated on optical breadboard which is mounted above the vacuum chamber, as can be seen in Fig. 8(a). Light is delivered to this part by the objective which collimates upward the ion scattered photons. Figure 8(b) shows the beam path through the

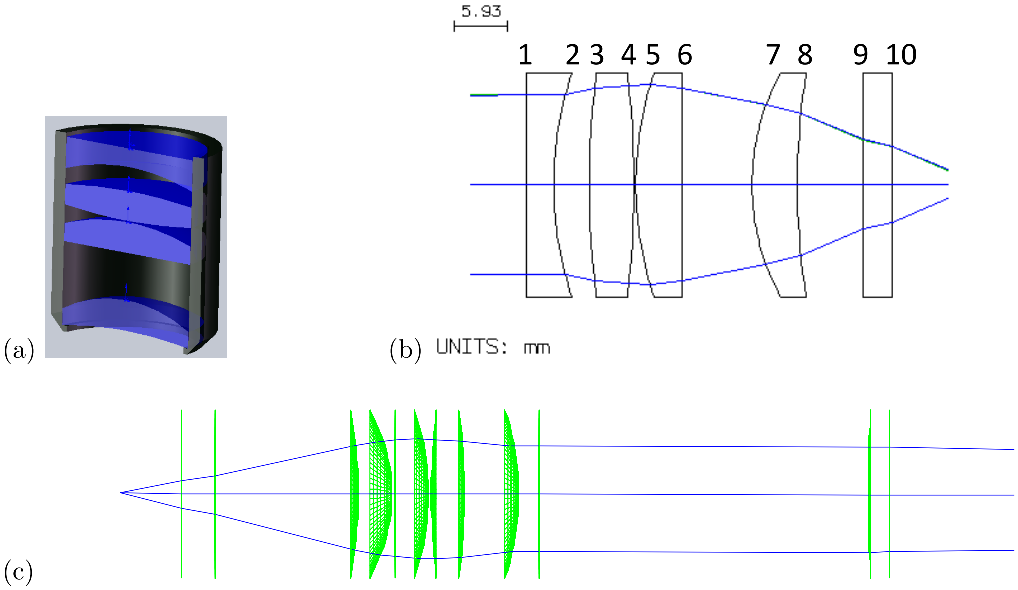

Figure 7: (a) Section view of the imaging system objective. It is made of four BK7 1-Inch-diameter lenses that were mounted in an cylinder. (b) A deign draw of the objective refracting surfaces. Each lens is represented by its two surfaces, the last two surfaces of the array (9,10) represent the optical port window which is flat. The surfaces radius of curvature and relative distances are given in Table 1. (c) A plot of ray tracing through the imaging system objective. The rays source is the ion, the two last surfaces on the plot other side are a focusing 500 mm doublet. This setup is mounted vertically to deliver light to the magnification and analysis instruments of the imaging system on the top breadboard.

Surface No.	Radius of curvature	Distance to next surface	Material
1	∞	3.08	BK7
2	39.08	4	air
3	103.29	4.97	BK7
4	-103.29	0.2	air
5	39.08	5.12	BK7
6	∞	7.862	air
7	26	5.07	BK7
8	78.16	7.3	air
9	∞	3.3	Fused Sillica
10	∞	10	vacuum

Table 1: The objective optical surfaces radius of curvature (∞ stands for flat surface) and relative distance. All units are in mm. The objective lenses are made of standard BK7 glass while the vacuum chamber flange window is made of Fused Sillica.

optical components. The mirror M_1 bends the light coming from the objective to the breadboard plane. The doublet pair D_1 focuses the beam (reflecting of mirrors M_2 and M_3) through iris I_1. This iris functions as a spatial filter, it blocks light that is scattered from objects in the trap region (such as the trap electrodes). The polarization rotation unit (PRU) rotates the photons polarization by using $\lambda/4$, $\lambda/2$ wave-plates. This unit, together with the following Polarizing Beam Splitter (PBS), projects the arriving photons polarization state on an arbitrary polarization basis, dictated by the wave-plates orientation. The flipping mirror M_4 selectively routes the beam between an EMCCD camera (Andor Luca^{EM}) and two photo-multipliers tubes (PMT_1, PMT_2). Two PMTs (Hamamatsu H7360) are necessary to measure the two components of the polarization basis. The breadboard and the tube, in which the light travels from the objective, are optically sealed to minimize noise from background lights.

Figure 9 shows an image, taken by the EMCCD camera, of three trapped ions. This image actually shows the diffraction Airy discs that are centered around each trapped ion. These discs image is magnified by 40 when it is generated in the camera. Each disc diameter is larger then the camera pixel size which is 10×10 μm. Ions can be resolved as long as the distance between them

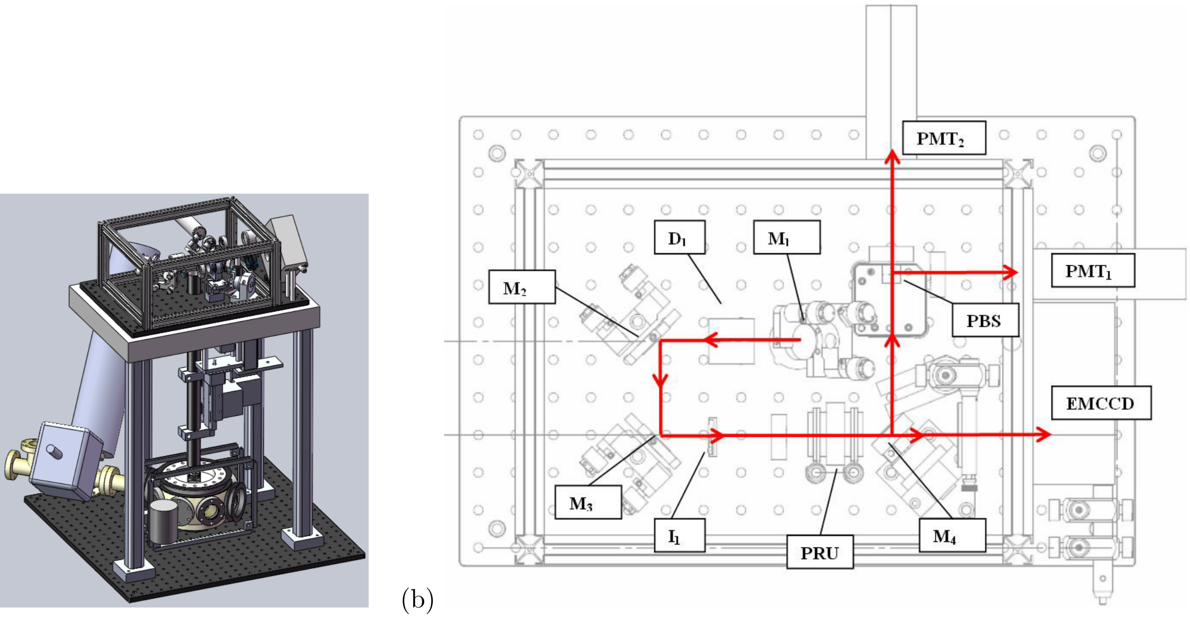

(a) (b)

Figure 8: (a) The whole imaging system. Light is gathered by the objective (which can be hardly seen on the top of the vacuum chamber) and collimated upward to the optical breadboard. Unlike how it looks in the image, the breadboard is sealed against light. (b) the light path through the components of the magnification, polarization analysis and detection.

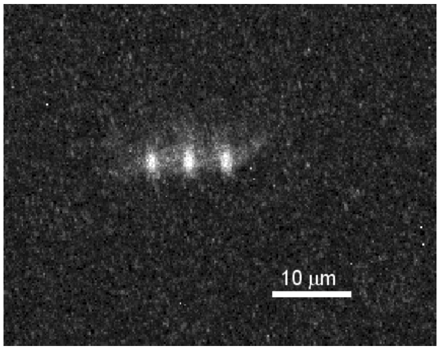

Figure 9: Three trapped ions. The ions image size is determined by the system diffraction limit, which is 0.8 μm. This image was taken using the EMCCD camera after it was magnified by 40 by the imaging system.

(determined by the trap spring constant and their Columb repulsion) is greater then the objective Airy disc radius.

3.5 The Magnetic field stabilization system

In the absence of light, magnetic field noises are the main source for ion-qubit decoherence. This problem is especially severe for superpositions of states within the same Zeeman manifold (states that are differ only by their m_F). The magnetic-field main noise source is the electric power line currents that oscillate at a frequency of 50 Hz and its harmonics. In our setup this issue is tackled by two methods:

1. Preforming measurements in a specific phase of the power line current only. An experiment is triggered by a zero crossing of the power line voltage. This fixes the induced magnetic field in all the experiment iterations. The constant resulting detuning can be compensated by counter detuning of radiation frequency. This method, while being relatively simple, has a major disadvantage which is reducing the measurement repetition rate to 50 iterations per second. This rate is significantly slower than the typical repetition rate.
2. Actively stabilizing the magnetic field on the ion. In this method a servo system uses magnetic field detectors in the ion vicinity and feedback electronics and inductors. Magnetic field oscillations that are faster than $\sim$ 1 Hz, are canceled along the setup quantization axis. Two

detection coils, 3 inch in diameter, are mounted symmetrically on the octagon flanges along this axis 10 cm before and after the trapping region. A weighted average of the detectors signal estimates the magnetic field on the ion. The compensating inductors are two additional square coils, with a side length of 1.5 m, that are held symmetrically along the quantization axis 0.5 m from the trapping region.

For achieving coherence time of 1 msec the magnetic field RMS fluctuations, in the bandwidth between 0.1 to 10 Hz, cannot exceed $\sim 100\ \mu$Gauss. The servo system reduces, by about a factor of 500, the magnetic field noise amplitude at 50, 100 and 150 Hz to the few μGauss level. A coherence time of 2.5 ms was measured in a Ramsey experiment (see section 4.8). To simplify the magnetic field regulation, great care was taken in selecting the setup components materials near the trap. Only non-magnetic materials could be used in the building of the trap and the vacuum chamber. For that the trap spacers where made of titanium, the trap electrodes from tungsten and the vacuum chamber from non-magnetic stainless steel (316).

The static magnetic field on the trap is ideally the quantization field. It is induced by three concentric pairs of coils that are driven by DC current supplies. The coils pair which its axis is aligned with the quantization direction sets the strength of the quantization field, which is typically of the order of few Gauss. The other two pairs currents are manually tuned to cancel static magnetic field components that are perpendicular to the quantization axis. As can be seen in Fig. 10, the quantization field direction is tilted by 45° relative to the trap axis.

3.6 The lasers

Ions are loaded into the trap and manipulated using lasers. This setup requires six different lasers that differ by their wavelength and frequency stability. ^{88}Sr^{+} is considered to be a "soft" ion, with relevant transition frequencies all in the visible and IR (no UV) spectrum. All the wavelengths necessary for the laser cooling and manipulation of ^{88}Sr^{+} ions are available either directly with or by doubling diode lasers (DL). Most of our DL's are mounted in external cavities (ECDL) that assist in reducing their linewidth. Further spectral narrowing is achieved by locking the lasers to Fabry-Perot cavities. Locked laser radiation is guided by single-mode optical fibers to the octagon chamber, as can be seen in Fig. 10. There, the beams are focused, through optical ports, on the trapped ions. Table 2 gives a comprehensive list of the beams that are used in our experiments and

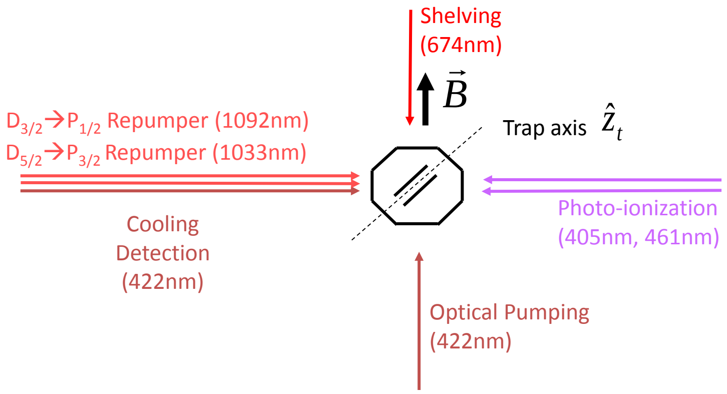

Figure 10: The orientation of the each beam which is used in the experiment relative to the octagon vacuum chamber and the trap axis. The 461 and 405 nm beam co-propagate as they are coupled to the same fiber. The 422 nm and the IR beams are combined and enter the vacuum chamber through the same optical port using a dichroic mirror. All the beams axes are in a surface which is parallel to the optical table which is spanned by the setup quantization and the trap axes. It is lifted by 4 inches above the table "slicing" the trap end-caps in the middle.

their main features. The following section will elaborate on the optical and electrical setups that produce each beam.

3.6.1 The photo-ionization beams

$^{88}Sr^{+}$ ions are loaded into the trap by photo-ionization of neutral Strontium atoms [40]. Figure 11 shows the schematics of a two-color Sr photo-ionization scheme. A 461 nm laser excites one of the ^{88}Sr atom valence electrons from their ground level ($5s^{2 1}S_0$) to an excited level ($5s5p^1P_1$). This beam is a second harmonic (SH) of a 921 nm ECDL. Frequency doubling is done by periodically poled KTP (PPTKP) non-linear crystal which has a poling period of 5.3 μm and length of 30 mm

Wavelength [nm]	Purpose	Polarization	Trap focus waist [μm]	Intensity on the ion [10^3 Watt/m^2]
422	detection	elliptical	176	3.08
422	optical pumping	left / right circular	20	4.55
422	on-resonance cooling	elliptical	176	0.044
422	off-resonance cooling	elliptical	176	3.76
674	shelving	linear-vertical	16	1000
1092	repumper	elliptical	52	0.81
1033	repumper	elliptical	50	0.06
461	photo-ionization	random	73	1.07
405	photo-ionization	random	64	195

Table 2: A list of all the beams that are used in the variety of the executed experiment protocols. The beams intensities were calculated by averaging their power of the area of a circle with the focus waits radius. The 422 nm off-resonance beam is 360 MHz red-detuned relative to the on-resonance and detection beams, that are in the frequency of the $S_{1/2} \rightarrow P_{1/2}$ transition frequency.

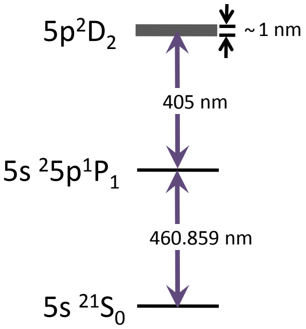

Figure 11: The two-photons resonance of ^{88}Sr atom ionization. The $5p^2D_2$ level is a broad auto-ionizing level.

(Raicol Crystals Ltd.). The crystal is mounted in a thermally stabilized housing. A single pass of a 80 mW fundamental beam produces a SH radiation which, after coupling to a single mode fiber, has a power of 30 μW. This power is enough to saturate the $5s^{21}S_0 \rightarrow 5s5p^1P_1$ transition (with $I_{sat} = 428$ W/m^2). A 405 nm free running diode laser (InGaN) excites the electron from the $5s5p^1P_1$ level to an auto-ionizing level (with $I_{sat} = 3.9 \cdot 10^5$ W/m^2). The two photo-ionization beams are coupled by the same single-mode optical fiber. The fiber output is collimated near the vacuum chamber and focused on the trap. The beams orientation is such that their k-vectors are perpendicular to the hot neutral Sr atoms jet, that crosses the trapping region, to minimize Doppler broadening of the ionization transitions.

3.6.2 The resonance fluorescence beams

The main transition of the ^{88}Sr$^+$ ion which we use is the $5s^2S_{1/2} \rightarrow 5p^2P_{1/2}$ transition near 422 nm as shown in Fig. 4. Scattering (absorbtion and re-emission) photons on this transition is used for ion detection, doppler cooling and optical pumping. This transition has a natural linewidth of 21.5 MHz which is larger then the typical Zeeman splitting of the $5s^2S_{1/2}$ Zeeman states under magnetic field of few Gauss. Hence, the different Zeeman states are un-resolved, and a single 422 nm beam can address all the $\{m_F, m_{F'}\}$ transition lines, simultaneously. Here m_F and $m_{F'}$ stand for the electron spin projection on the quantization axis of the $5s^2S_{1/2}$ and $5p^2P_{1/2}$ states, respectively. A specific $\Delta m = m_{F'} - m_F$ transition can be addressed by shining a purely linearly or circularly (left/right) polarized beam as done in optical pumping (see section 4.2).

A 422 nm beam is generated by frequency doubling 844 nm ECDL (Toptica DL 100 SHG). Figure 12 shows the frequency doubling and frequency stabilization circuit of this laser. The diode supply current is rapidly (20 MHz) modulated to allow Pound-Drever-Hall [41] locking of its frequency to a cavity and vice versa. The frequency doubler is a BBO nonlinear crystal which is mounted inside a butterfly cavity for conversion efficiency enhancement. The resonance frequency of the doubler cavity is locked to the laser diode frequency for optimal coupling. On the other side, the diode laser frequency itself is locked to an external Fabry-Perot cavity. This cavity is of plano-concave type, its two mirrors are glued to a 7.5 cm Zerodur spacer were the flat mirror is mounted on a piezo-electric stack. The cavity has a finesse of roughly 100. The diode is kept locked to the cavity by a regulator feedback to its external cavity piezo-electric stack and current supply. This narrows the diode linewidth and gives it short term frequency stability.

Long term frequency stability is achieved by locking the Zerodur cavity resonance, to an atomic reference, to correct for its thermal expansion. The ion $5s^2S_{1/2} \rightarrow 5p^2P_{1/2}$ transition has the serendipitous spectral proximity to the $5s^2S_{1/2}(F'' = 2) \rightarrow 6s^2P_{1/2}(F' = 2, 3)$ transition line of neutral ^{85}Rb [42]. The Rubidium line is 440 MHz red detuned and functions as an atomic reference. Saturation-absorption spectroscopy [43] is used to generate an electronic error-signal and locks the cavity length (and hence, it resonance frequency) to the Rb line.

Due to experimental geometric considerations the 422 nm beam is split to two optical channels that are guided in different fibers and focused on the ion from two different orientations (Fig. 10).

1. Doppler-cooling and detection of an ion are preformed by a beam with k-vector perpendicular to the quantization axis. This beam contains all the ion spherical coordinates polarizations $\{\pi, \sigma^+, \sigma^-\}$, hence, it couples all the $5s^2S_{1/2} \rightarrow 5p^2P_{1/2}$ transitions. This beam frequency can be varied between being close to or on-resonance or 360 MHz red-detuned relative to the ion transition frequency. Initial Doppler cooling is done with the far-red-detuned beam while, for advanced Doppler cooling and ion detection, the close to or on-resonance beam is used, respectively. Switching between these two beam is done by the 80 and 220 MHz Acusto-Optical Modulators (AOM) as can be seen in Fig. 12.

2. Optical pumping is preformed by a beam with a k-vector along the quantization axis. This beam is in a pure state of either σ^+ or σ^- polarization, allowing optical pumping of the ion population to the $5s^2S_{1/2}(m_F = 1/2)$ and $5s^2S_{1/2}(m_F = -1/2)$ states, respectively. Optical

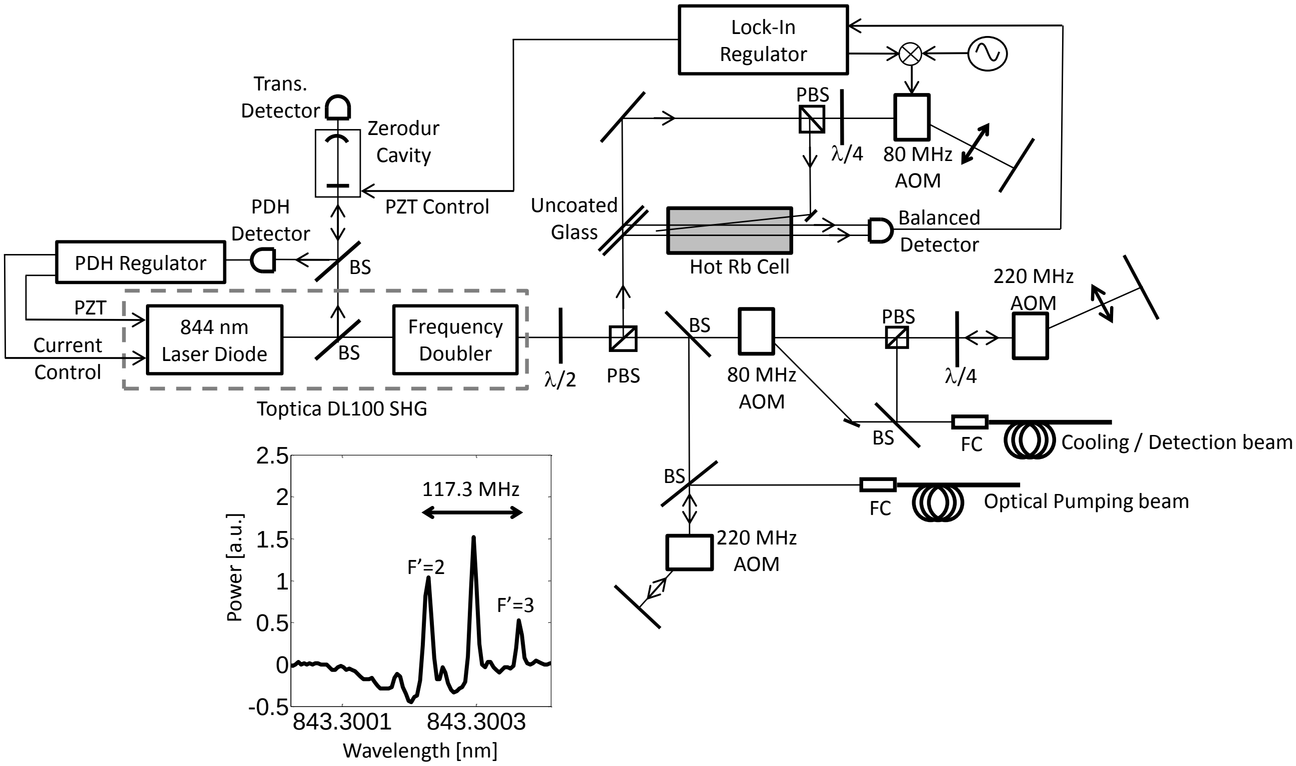

Figure 12: The frequency locking and tuning circuit of the 422 nm beam. The IR DL is locked by the PDH method to the Zerodur cavity. The frequency doubler is locked to the diode by using the same modulation of the previous lock. The Zerodur cavity length is regulated by absorption saturation spectroscopy of the hot (∼120°) ^{85}Rb atoms. The inset shows the saturation signal where the two external peaks represent the two hyperfine transitions in the atoms. The cavity is locked to the middle crossover peak. Differen switching combinations, of the modulators in the lower right corner, deliver beams to different ports of the trap vacuum chamber. The cooling beam frequency can be red-detuned by 360 MHz from the $5S_{1/2} \rightarrow 5P_{1/2}$ transition.

pumping is described in section (4.2). This beam frequency is on-resonance. It is switched by turning on and off the corresponding 220 MHz AOM.

3.6.3 The quadruple transition beam

The $^{88}\text{Sr}^+$ energy-level structure includes two D-orbital states. A dipole transition from these states to the ground state is forbidden. Quadrupole transition is the lowest radiation moment that can couple these states and therefore the $4d^2D_{3/2}$ and $4d^2D_{5/2}$ states are metastable. Their long life time T_1, of almost 0.5 sec, makes them suitable for coherent quantum information storage. Coherent population transfer from the ground state to the $4d^2D_{5/2}$ state ("electron shelving", or just "shelving") is preformed by a 674 nm narrow linewidth diode-laser beam.

Figure 13 shows the frequency stabilization and switching circuit of the diode laser (Toptica DL 100). This ECDL has an extended external cavity of 10 cm length to achieve a narrow fast linewidth of 200 kHz. The diode is locked, by a feedback on its current and grating PZT control, to a high finesse cavity (made by Advanced Thin Film) which can be seen in Fig. 14(a). This cavity is 7.7 cm long, its spacer is made of Ultra Low Expansion (ULE) glass which has a thermal expansion coefficient $\alpha = \Delta l/l \simeq 10^{-8}/^\circ\text{C}$ at room temperature. The cavity mirrors (plano-concave) are highly reflecting. Figure 14(b) shows the cavity ring-down signal. In this measurement the laser frequency was rapidly swept across one of the cavity resonances while the transmitted beam power, through the cavity, was measured. The exponential power decay has a characteristic half time of 7 μsec indicating a corresponding cavity linewidth of 22.7 kHz. The cavity Free Spectral Range (FSR) is $c/(2l) = 1.94$ GHz, where c is the speed of light, its finesse is therefore 85,756. The cavity is mounted inside a vacuum chamber (10^{-8} Torr) on a soft Viton suspensor for thermal, pressure and vibrations isolation. Yet, due to temperature drifts the cavity resonance frequency drifts by a typical rate of 10 Hz/sec. A periodic, every 2 minutes, gauging of the laser frequency, using the ion transition, limits the beam detuning to below 1 kHz. Since usually the $5s^2S_{1/2} \rightarrow 4d^2D_{5/2}$ transition is power broadened to ~ 100 kHz this thermal drift is not a major limitation for effective electron shelving. Section 4.6.1 elaborates on the 674 nm beam frequency drift due to thermal noise. The 674 nm beam is guided to the trap region using a single-mode polarization-maintaining optical fiber. A control loop regulates the output power from the fiber (noise-eater) by a feedback to the acusto-optical switch rf power. This switch has fast response to the rf signal amplitude. It allows modulation of the beam power by a frequency of up to 1 MHz. It is also the device with is

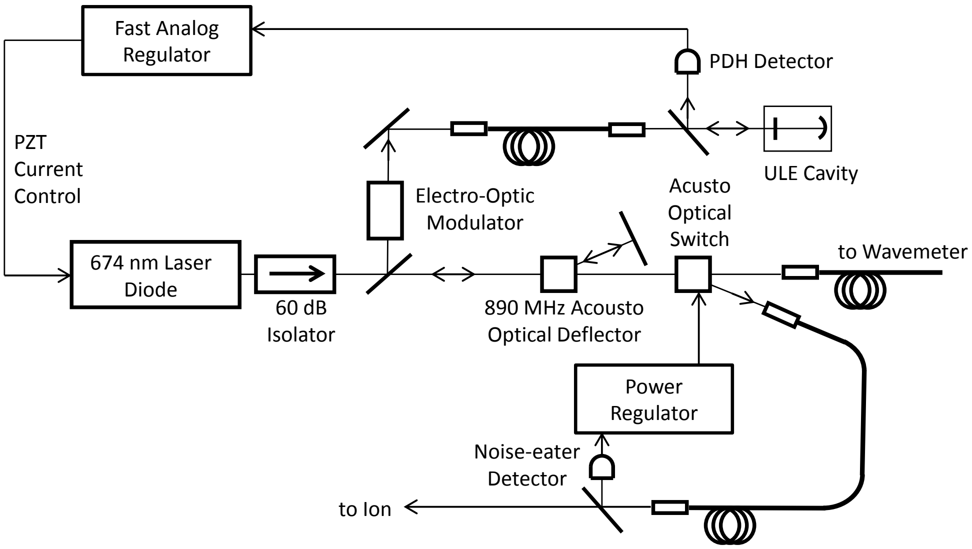

Figure 13: The 674 nm beam frequency stabilization circuit. The DL is locked to a high-finesse ULE cavity which reside in a vacuum chamber for thermal, pressure and vibration isolation. Fast acusto-optical switch can generate short beam pulses (down to 1 μsec duration) while regulating their power envelope.

used for fine tuning of the frequency of the beam which is shined on the ion.

The 674 nm beam that is shined on the ion has a k-vector that is aligned with the quantization axis and is tilted by 45° from the trap $\hat{z}_t$ as can be seen in Fig. 10. It is linearly polarized, vertically to the surface which is spanned by the trap and the quantization axes. The Lamb-Dike parameters of this beam and the trap axial and radials vibrations modes are 0.05 and 0.0354, respectively.

Figure 15 shows the laser noise Power Spectral Density (PSD) while being free running and while being locked to the ULE cavity. The regulation circuit feedback shrinks the beam linewidth from roughly 200 kHz to 80 Hz. This is achieved by suppressing noise, in the spectral domain, from DC to the unity gain frequency at roughly 1 MHz. The beam linewidth was verified in Ramsey measurements using the ion $S_{1/2} \rightarrow D_{5/2}$ transition as can be seen in section 4.6.2. At the unity-gain frequency the feedback loop phase delay is accumulated to π (180°). The contribution to the phase delay comes from the following loop components by the bill: the cavity response (90°), delays in the detection and regulation electronics ($\simeq$ 50°), optical fiber and transmission lines delays (10°) [44].

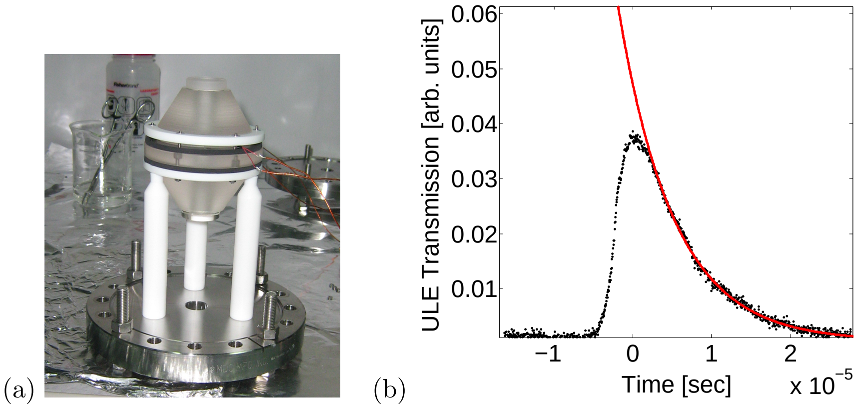

Figure 14: (a) The ULE cavity on its Viton suspensor before introducing to the vacuum chamber. (b) The ring-down signal which was measured on the cavity transmission while shifting the laser frequency rapidly along its resonance. The decay time and the cavity length set its finesse on 85,756.

The rest of the phase margin is assumed to be the phase difference between current and frequency modulation in the diode laser due to thermal effects. At the unity gain frequency amplification of the fast phase noise can be spotted (referred to as "servo bump"). Increasing the gain above this point causes the emergence of oscillations of the laser frequency. The frequency stabilization system and the diode linewidth narrowing are limited by this phenomenon. Off-resonance stimulation of the ion population due to this phase noise is presented in section 4.6.3.

3.6.4 The Repumpers beams

Both the $5p^2P_{1/2}$ and the $5p^2P_{3/2}$ ion states have a branching ratio of 1:14 to the meta stable states $4d^2D_{3/2}$ and $4d^2D_{5/2}$, respectively. Electronic population decay to one of the meta-stable states forces a long pause in the laser cooling sequence. To avoid these unwanted delays, repumper beams are applied to extract population from the D-orbital states back to the excited P-orbital states. Population is pumped from the $4d^2D_{3/2}$ ($4d^2D_{5/2}$) to the $5p^2P_{1/2}$ ($5p^2P_{3/2}$) state by a 1092 (1033) nm beam. These two beams are the only Infra-Red (IR) lasers in the setup. They share the same Fabry-Perot cavity for frequency stability and narrowing. Figure 16 shows the joint frequency stabilization circuits of the two laser diodes. The 1092 nm beam is produced by a Distributed Feed-Back (DFB) diode laser and the 1033 nm beam is produced by an ECDL.

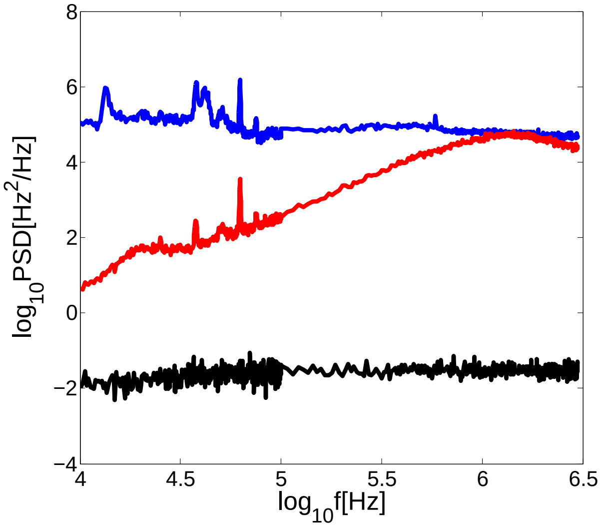

Figure 15: The 674 nm beam PSD when free running (blue) and frequency locked to the ULE cavity (red). The black line the spectral noise floor. The locked laser PSD reaches to maximal value at 1 Mhz where the stabilization transfer function reaches a π phase delay. The energy in this portion of the spectrum reflects the beginning of frequency oscillation of the laser.

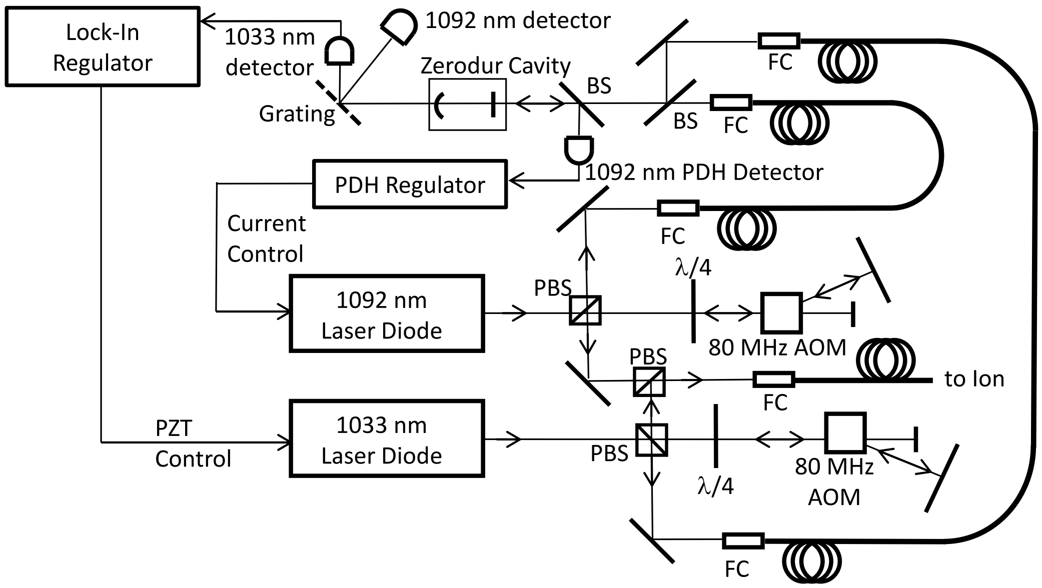

Figure 16: The frequency stabilization circuit. The 1092 and 1033 nm beams are locked simultaneously to the Zerodur cavity by a lock-in and PDH methods, respectively. These beams are combined together, on a PBS, and coupled to a single single-mode polarization-maintaining fiber.

For locking, the two beams are coupled to a Zerodur cavity (finesse of 100) which is mounted in the same vacuum chamber as the ULE cavity for the 674 nm laser. The ECDL is locked to the cavity by a lock-in method in which the beam frequency is slightly modulated. The corresponding transmission amplitude variation, through the cavity, produces an error signal which is feedback to the diode external cavity PZT. The DFB diode is locked by the PDH method to the cavity. For that its current is modulated at 20 MHz. The PDH detector is not disrupted by the 1033 beam, though they reside on the same optical axis, because these beams are modulated at different frequencies. The frequency gaps between the cavity resonances and the ion transitions frequencies are bridged by two AOMs that also function as the beam switchs. The beams are coupled together to a single-mode polarization-maintaining IR optical fiber. They co-propagate and shined along the same optical axis on the ion. The thermal drifts of the Zerodur cavity shift the beams frequencies by a negligible detuning (1 MHz/hour) as compared with the transitions linewidth.

3.7 RF sources and experiment control

Several rf generators are embedded in the setup. The trap oscillating voltage is generated by a dedicated signal generator (HP 8640B) at frequency of 21.8 Mhz. This signal is amplified by a 30 dB rf amplifier (IntraAction) and is fed to the rf helical resonator for voltage amplification and impedance matching with the trap. The beams acusto-optical switches and modulators (Brimrose) are driven in the frequency range between 70 to 220 MHz. Their rf sources are Voltage Controlled Oscillators (Minicircuits VCOs) that are amplified by wide spectrum 30 dB rf amplifiers (Minicircuit ZHL-1-2W). Two Direct Digital Synthesizers (DDS) are used to drive the 674 nm beam switch and the trap rf electrode. These devices (Analog Devices AD9854 chips mounted on NovaTech DDS8m board) generated frequency, amplitude and phase can be modified in a real time by fast parallel communication interface. They can supply rf signal at frequencies of up to 100 MHz, sampled in a digital resolution of 14 bits.

An experiment is a deterministic sequence of optical beams and rf pulses that manipulate the trapped ions. This sequence is executed, in real time, by a Field Programmable Gate Array (FPGA) which follows a pre-defined protocol. This hardware is supplied by National Instruments (PCI-7813R) and is programmed by LabView®. This array implements a simple CPU core which switches devices, in a temporal resolution of 25 nsec, on and off by TTL (Transistor Transistor Logic) signals. This core also controls the DDS generated signal, reads the PMT photon detections and controls the PRU waveplates orientation in the imaging system.

4 Basic qubit operations

This section describes experiments, where electro-magnetic radiation interacts with the trapped ions. In these experiments we benchmarked all quantum information processing operations. These experiments concern the selection of a TLS, out of the ion internal states, and the ability to coherently manipulate it. This TLS is referred to as a qubit (quantum-bit), two types of qubits are realized with a single trapped $^{88}\mathrm{Sr}^{+}$ ion:

1. An optical qubit where the two states are states in the $S_{1/2}$ ground level and the meta-stable level $D_{5/2}$ and are optically seperated. We will denote this qubit levels as $|0\rangle = |S\rangle$ and $|1\rangle = |D\rangle$ corresponding to the $S_{1/2,1/2}$ and $D_{5/2,3/2}$ states, respectively. This qubit is coherently manipulated by the 674 nm laser beam.
2. A Zeeman qubit where the two qubit states are the two electronic spin states of the $S_{1/2}$ manifold. We will denote these levels as $|0\rangle = |\downarrow\rangle$ and $|1\rangle = |\uparrow\rangle$ corresponding to the $S_{1/2,-1/2}$ and $S_{1/2,1/2}$ states, respectively. This qubit is coherently manipulated by a rf fields.

Working with each qubit type has advantages and disadvantages. For example, An optical qubit had a limited lifetime (T_1), it also requires, for example, a nontrivial laser frequency stability of $\sim 10^{-15}$ for achieving a coherence time of 1 sec. It is, however possible to address a single optical qubit in a string of trapped ions using a focused laser beam. Moreover, due to relatively high Lamb-Dicke parameter in optical qubit-beam interaction, sideband transitions can be driven. This is especially crucial for entangling two qubits states as will be described in section 5. The Zeeman qubit, on the other hand, has practically infinite lifetime but it is more susceptible to magnetic field noises. Mapping of one qubit state to another is possible by applying the 674 nm beam.

The characterization of any qubit operation is done by repeating it and measuring its outcome many times to gain statistical significance. A characterization protocol, typically starts with state initialization followed by a sequence of laser or rf pulses with constant timing and ends by projecting the qubit post-protocol state by measurement.

4.1 Loading the trap and maintaining an ion trapped

The trap is loaded by driving current through a Sr oven. Simultaneously, the trap is shined by photo-ionization (461, 405 nm), off-resonant cooling (red-detuned 422 nm) and the 1092 nm repumper laser beams. Simultaneously, the trapping region is imaged onto the EMCCD camera. Once an ionized Sr atom is trapped it is detected by its fluorescence of 422 nm photons. The oven current is tuned to give a typical delay of ∼1.5 minutes between beginning the loading sequence until a single trapped ion is observed. Following trapped ion detection, the photo-ionization beams and the oven current are shut down to stop the loading process. A flipping mirror in the imaging system blocks the camera and the arriving photons are channeled to the PMTs.

The $^{88}\mathrm{Sr}^{+}$ isotope has a low cross section to chemical reaction with residual gasses in the vacuum chamber (particularly H_2). Together with the very low pressure in the chamber, the probability of loosing an ion by re-combination with Hydrogen is negligible. As long as the trap is driven and the off-resonant cooling beams remain locked a trapped ion remains. We have observed trapped ion for periods exceeding three days. The constant off-resonant cooling is necessary to cancel the trap heating which, otherwise, would gradually boil the ion out of the trap. The off-resonance cooling beam is effective in cooling hot atoms from a jet and keeping ions trapped but does not cool the ions to the Doppler limit. Further cooling is applied before protocol execution. A short ($\sim 50\ \mu$ sec) on-resonance cooling beam pulse is applied and cools the trapped ions to a temperature of ∼1 mK. at the Doppler limit. When protocol execution is complete the off-resonant cooling and the 1092 nm beams are turned on again for ion maintenance.

4.2 Qubits initialization

Qubits are initialized to a well-known pure state by optically pumping the electronic population to a dark state. Further coherent manipulations can bring the qubit state to any coherent superposition of the states $|0\rangle$ and $|1\rangle$.

Optical pumping is preformed by a 422 nm beam that propagates along the quantization axis, and is left (right) circularly polarized. Under photon scattering from this beam the electronic population is pumped to the $S_{1/2,m_F=1/2}$ ($S_{1/2,m_F=-1/2}$) dark state. Figure 17 illustrates the process of optical pumping. Due to angular momentum conservation considerations the left-circularly-polarized beam, σ^{+} in the ion spherical coordinates, transfers population from the $S_{1/2,m_F=-1/2}$ state to the excited $P_{1/2,m_F=1/2}$ state. Decay re-distributes the population between the $5s^2S_{1/2}$ Zeeman manifold states. However, since only the $S_{1/2,m_F=-1/2}$ dark state is excited, gradually, population is trapped in the $S_{1/2,m_F=1/2}$ state. Optical pumping pulse of 50 μsce transfers 99.9% of the qubit population to the $S_{1/2,m_F=1/2}$ state. Zeeman (optical) Qubit initializing to other state

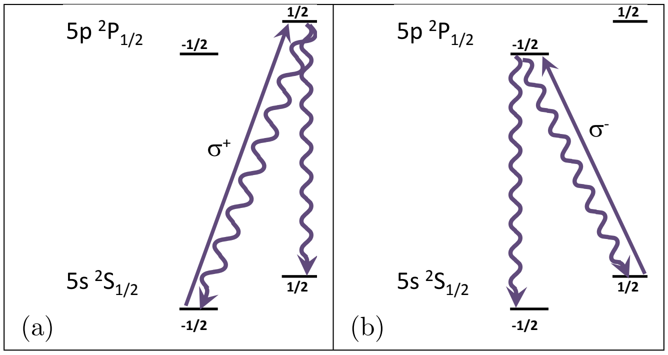

Figure 17: Optical pumping scheme. On application of the optical-pumping beam, which is (a) σ^+ or (b) σ^- polarized, population converges to the dark states $P_{1/2,m_F=1/2}$ and $P_{1/2,m_F=-1/2}$, respectively.

then the $|\uparrow\rangle$ ($|S\rangle$) state is done by applying a rf (674 nm beam) pulse, on resonance with the qubit transition, and rotates its state to the desired superposition (Eq. 2.3.10). Appendix (50) shows a quantum process tomography (QPT) of the optical pumping process.

4.3 Qubits readout

Most protocols end with readout of the qubit final state. This is done by projecting the state on a measurement basis denoted as the qubit $|0\rangle$ and $|1\rangle$ states. Correspondingly, the outcome of a single application of quantum protocol and measurement is either 0 or 1. For state measurement in a different basis, a rotation pulse precedes qubit state projection in the measurement basis. By iterating a protocol, and its final state readout, one can statistically estimate the final state populations. Considering a qubit final state $|\Psi_f\rangle = \alpha|1\rangle + \beta|0\rangle$, averaging many readouts outcomes yields the absolute values $|\alpha|^2$,$|\beta|^2$, up to a statistical error which equals $|\alpha||\beta|/\sqrt{N}$, where N is the number of iterations.

Zeeman qubit readout is preformed by mapping one of its states onto an optical qubit state and projecting it on the $|S\rangle$ and $|D\rangle$ states. This mapping is done by the "electron shelving" technique [45], in which, a 674 nm beam π pulse transfers the qubit $|\uparrow\rangle$ state population to the optical qubit $|D\rangle$ state. An optical qubit readout is done by applying the detection 422 nm on-resonance beam. This beam leads to resonance fluorescence scattering of 422 nm photons by the ion, conditioned on being in the $|S\rangle$ state. Hence, it projects the ion to a "bright" and "dark" states with a

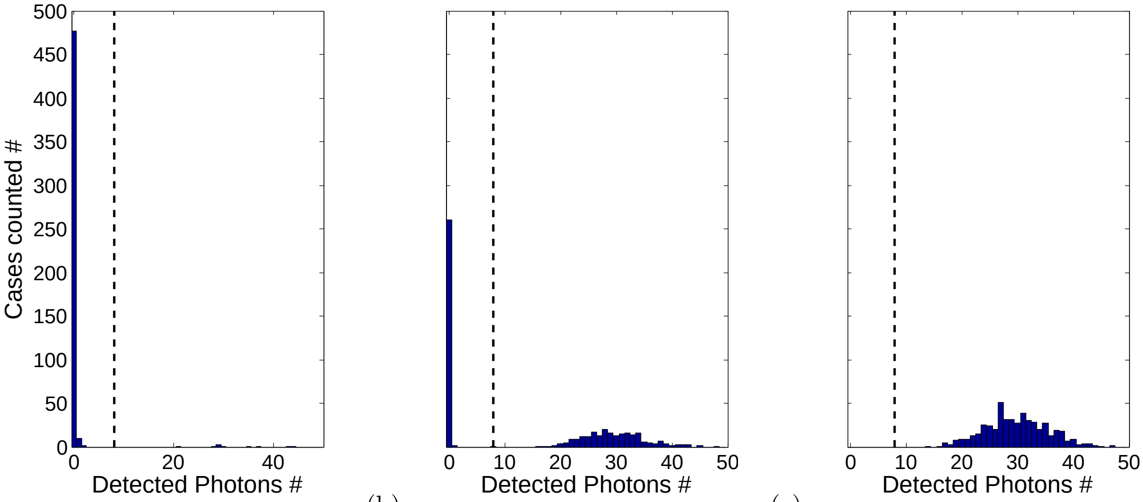

(a) (b) (c)

Figure 18: Resonance fluorescence photon detection histograms of (a) 2%, (b) 47 % and (c) 100 % bright ion states. Each histogram was measured with 500 readout repetitions of the ion state. In each event the qubit was exposed for 500 μsec to the 422 nm detection beam. On average, 30 photons were detected by the imaging system PMT for a bright qubit, for this exposure time. An ion is considered to be "bright" is more then 8 photons were detected on the application of detection beam.

probability that matches the qubit $|S\rangle$ and $|D\rangle$ states populations, respectively. Scattered 422 nm photons are detected by the imaging-system PMTs. The number of scattered photons during a fixed excitation duration, follows a Poisson distribution. The "dark" and "bright" ion states generate two distributions with different mean values of detected photons. A 500 μsec detection pulse leads to counting of $\bar{n}_{bright} \simeq 30$ and $\bar{n}_{dark} \simeq 1$ photons when the qubit is in "bright" and "dark" states, respectively. Figure 18 show three photon detection histograms for 2% (almost completely "dark"), 47% and 100% "bright" ions. In each of the histograms the qubit states were measured 500 times. The ratio $|\alpha|^2/|\beta|^2$ is estimated by $n_{>th}/n_{<th}$, where, $n_{<th}$ and $n_{>th}$ are the number of iterations in which the detected number of photons was bellow or above a pre-determined threshold $th = 8$, respectively.

The process of Zeeman qubit initialization and readout was deeply studied and optimized in

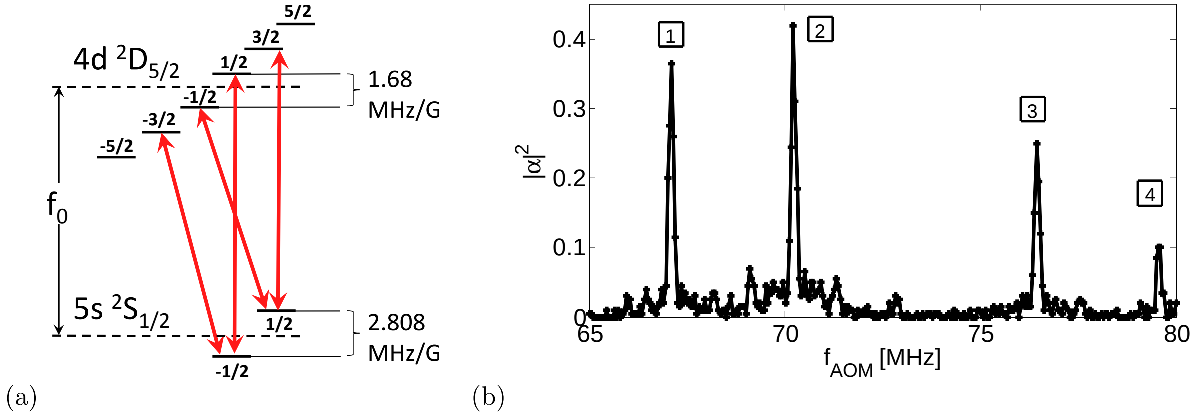

Figure 19: (a) The $5s^2S_{1/2}$ and $5d^2D_{5/2}$ states Zeeman manifolds and the accessible transitions for our 674 nm beam geometry. (b) A frequency scan of the $5d^2D_{5/2}$ population by the 674 nm beam when a 2.78 Gauss magnetic field is applied on the ion. The designated peaks are the 1.($m_F = -1/2,\ m_{F'} = 1/2$), 2.($m_F = 1/2,\ m_{F'} = 3/2$), 3.($m_F = -1/2,\ m_{F'} = -3/2$) and 4.($m_F = 1/2,\ m_{F'} = -1/2$) transitions. None of the excitation reaches $|\alpha|$=1 (a complete electron shelving) because the initial electronic population was distributed between the ground state manifold levels.

our system [46]. The main sources of error in this process are qubit initialization and readout shelving infidelities. By Applying extensive techniques a 0.9997 initialization and readout fidelity was demonstrated.

4.4 Spectroscopy of the $S_{1/2} \rightarrow D_{5/2}$ transition

For optical qubit manipulations and electron shelving of Zeeman qubit states one has to drive the $5s^2S_{1/2} \rightarrow 4d^2D_{5/2}$ optical transition. The Rabi frequency for this transition can be expressed in terms of the reduced matrix element $\langle 5S_{1/2}||r^2C^(2)||4D_{5/2}\rangle$ and the Wigner 3-j symbols.

$$\Omega_0 = \left| \frac{eE_0\omega_0}{2\hbar c} \langle 5S_{1/2}||r^2C^(2)||4D_{5/2}\rangle \sum_{q=-2}^{2} \begin{pmatrix} 1/2 & 2 & 5/2 \\ -m & q & m' \end{pmatrix} c_{ij}^{(q)} \varepsilon_i n_j \right| . \tag{4.4.1}$$

Here ε_i, n_j are the vector components of the polarization and the beam normalized $\vec{k}$-vector, respectively. The tensors $c_{ij}^{(q)}$ are 2^{nd} order tensors given explicitly in [47]. As can be seen in Fig. 10, the 674 nm beam $\vec{k}$-vector is parallel to the quantization axis. In this case the geometrical factor $c_{ij}^{(q)}\varepsilon_i n_j$ is non-zero only for $q = \pm 1$, thus allowing only $\Delta m_F = m - m' = \pm 1$ transitions. Therefore, only four transitions between these levels manifolds are accessible. Figure 19 (a) shows the allowed transitions between the Zeeman manifolds. Each transition frequency is slightly different due to finite magnetic field and the variation between ground state and the $D_{5/2}$ states Landé factors. It is calculated, in MHz, by:

$$f(m_F, m_{F'}) = f_0 + (-2.802 \cdot m_F + 1.68 \cdot m_{F'}) \cdot B, \tag{4.4.2}$$

where, m_F and $m_{F'}$ are the ground and $D_{5/2}$ states spin projections, respectively. The transition frequency in zero magnetic field is f_0 and B is the magnetic field on the ion, in Gauss. Figure 19 (b) shows a frequency scan of the 674 nm beam across these transitions. In each step of this scan the ions initial state was in an equal statistical mixture of the ground manifold states. A following 674 nm pulse was applied for a fixed time. The optical qubit readout shows probability of a transition to the $D_{5/2}$ level. A scan of the pulse frequency shows four sharp transition peaks in the figure. By the relative frequency gaps between the peaks one can estimate the magnetic field on the ion, which was a 2.78 Gauss in this scan.

When narrowing a frequency scan on one of the transitions, spectral features that arise from the ion motion can be detected. Figure 20 shows a frequency scan of the 674 nm beam near the $5s^2S_{1/2}(m_F = 1/2) \rightarrow 4d^2D_{5/2}(m_{F'} = 3/2)$ ($|S\rangle \rightarrow |D\rangle$) transition. Here, the qubit was initialized to the $S_{1/2}(m_F = 1/2)$ state. The three peaks in the figure correspond to the Carrier, RSB and BSB transitions that were described in Eq. 2.3.7. The center-lobe corresponds to the carrier transition. There, almost all of the qubit population was excited to the $|D\rangle$ state by a $T_\pi = 10$ μsec π pulse. The lobe Full Width Half Maximum (FWHM) is $\Omega_0 = 2\pi \times 57$ kHz and is power-broadened by the Rabi frequency. The $|D\rangle$ state population near the main-lobe follows:

$$|\alpha|^2 = \frac{\Omega_0^2}{\Omega_0^2 + 4\pi^2\delta^2} \sin^2\left(\frac{\sqrt{\Omega_0^2 + 4\pi^2\delta^2}}{2} T_\pi\right), \tag{4.4.3}$$

where, δ is the detuning between the beam and the transition frequencies. The trap axial and radial vibrations generate red and blue side-lobes around the carrier separated by distances that match their corresponding harmonic frequencies. These sideband transitions have lower Rabi frequencies in the Lamb-Dicke regime, as predicted by Eq. 2.3.8. As a result, the side-lobes are narrower and lower than the carrier. During this measurement we had axial $\omega_z = (2\pi) \cdot 1$ MHz and radial $\omega_x = (2\pi) \cdot 1.9$, $\omega_y = (2\pi) \cdot 1.94$ MHz vibration frequencies. The two radial vibration frequencies are very close and, therefore, unresolved.

4.5 Qubit Rabi oscillations

Carrier transitions in optical and Zeeman qubits are driven by exposing them to coherent on-resonance radiation. As a consequence, electronic population oscillates between the qubit states at the resulting Rabi frequency. This frequency is determined by the radiation-qubit coupling strength, and is proportional to the square of the radiation power. Figure 21 shows optical qubit Rabi oscillations at a frequency of $\Omega_0 = (2\pi) \cdot 183$ kHz using a single, laser-cooled, ion. Oscillations were measured after initializing the qubit to the $|S\rangle$ state and applying a 674 nm resonant pulse for up to 170 μsec. For each pulse duration the population transfer to the $|D\rangle$ state was measured. Here, a π pulse of $T_\pi = 2.77$ μsec transferred 99% of the $|S\rangle$ state population to the $|D\rangle$ state. Qubit decoherence appears as decay of the oscillations contrast with increasing pulse duration. The coherence half life time was reached after $\simeq$13 Rabi oscillations. Variation of the Rabi frequencies of different vibration harmonic oscillator levels (due to the Debye-Waller coefficient; Eq. 2.3.8) is the main source for this decay. Here the axial oscillation levels were distributed with a mean occupation number $\bar{n}_z \simeq 20$, measured by fitting the qubit $|D\rangle$ population during the oscillations to,

$$|\alpha|^2 = \frac{1}{2}\left(1 - \frac{\cos(2\Omega_0 t) + (2\Omega_0 t\eta^2 \bar{n}_z)\sin(2\Omega_0 t)}{1 + (2\Omega_0 t\eta^2 \bar{n}_z)^2}\right), \tag{4.5.1}$$

where, $\eta = 1/20$ is the Lamb-Dicke parameter of the 674 nm beam and the trap $\hat{z}_t$ axis and t is the pulse duration. This equation is a good approximation for Rabi oscillations where the qubit population is distributed, by the Maxwell-Boltzmann distribution, between the vibration mode energy levels. The value of $\bar{n}_z$ is in rough agreement with what is expected by Doppler cooling. Rabi oscillations can also be driven on non-carrier transitions like red- and blue-sideband transitions. There, however, less nutation cycles can be driven coherently, roughly by η, due to

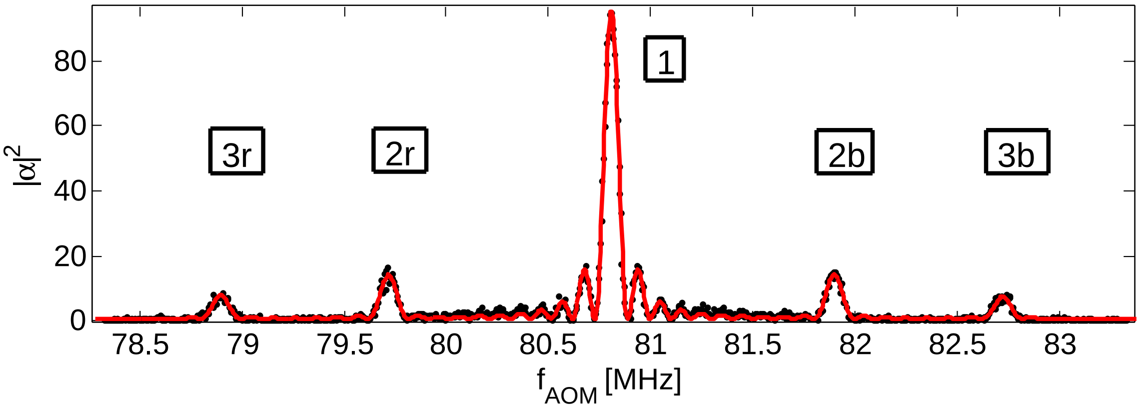

Figure 20: Frequency scan of the $5s^2S_{1/2}(m_F = 1/2) \rightarrow 4d^2D_{5/2}(m_{F'} = 3/2)$ transition by the 674 nm beam. The main-lobe (1) stands for the carrier transition and its side-lobes are for the trap axial (2r,2b) and radial (3r,3b) vibration modes transitions. Here $\omega_z = (2\pi) \cdot 1$ MHz ,$\omega_x = (2\pi) \cdot 1.9$ MHz and $\omega_y = (2\pi) \cdot 1.94$ MHz. The two radial side-bands cannot be resolved due to their spectral proximity.

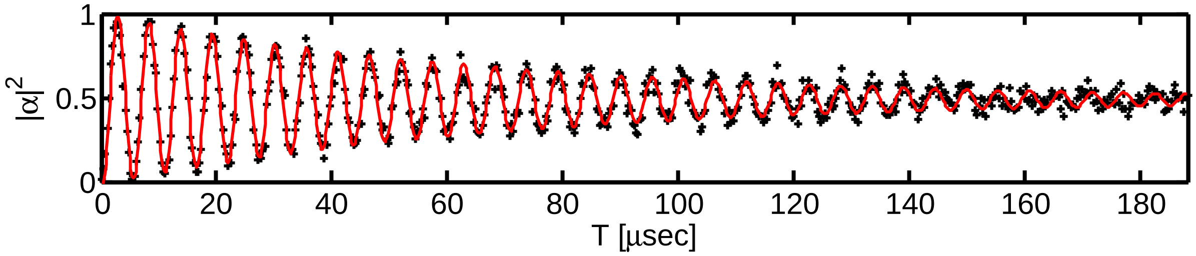

Figure 21: Optical qubit Rabi oscillation with Rabi frequency of $\Omega_0 = (2\pi) \cdot 183$ kHz. A 99% shelving efficiency was accepted for a π pulse with duration of 2.77 μsec. Here the mean level number of the axial vibration mode harmonic oscillator is $\bar{n}_z \simeq 20$.

wider variation in the the Rabi frequencies of the oscillator levels. Usually on a sideband transition, with only Doppler cooling, only a single oscillation is observed (Fig. 29 (a)). This decoherence rate is proportional to the ions temperature which dictates it population distribution width between the vibration mode energy levels. Cooling of optical qubits to the ground state (see section 4.7) allows for coherent Rabi oscillations in these transitions.

Rabi oscillations of a Zeeman qubit between the $|\uparrow\rangle$ and $|\downarrow\rangle$ states are shown in Fig. 22. Here the qubit was initialized, by an optical pumping, to the $|\uparrow\rangle$ state. A 3.3 MHz rf field was generated, by driving oscillating current through the trap rf electrode. The oscillating magnetic field leads to oscillations at a Rabi frequency of $\Omega_0 = (2\pi) \cdot 118$ kHz and a π pulse time of and 4.21 μsec. As the rf radiation wavelength is much longer then the variance in ion position, the corresponding Lamb-Dicke parameter is negligible. Therefore, the mechanism of multi oscillator levels decoherence is not relevant for Zeeman qubit Rabi nutation. The coherence half life time was measured to be equivalent to ≃120 Rabi oscillations. It was induced by amplitude noise of the rf field.

4.6 Characterization of the 674 nm laser frequency stability using an optical qubit

The trapped ion $S_{1/2} \rightarrow D_{5/2}$ transition is a highly stable frequency discriminator. It is used to characterize the 674 nm beam frequency stability and noise in three spectral regimes:

1. In the very low frequency regime where the beam frequency stability is governed by thermal

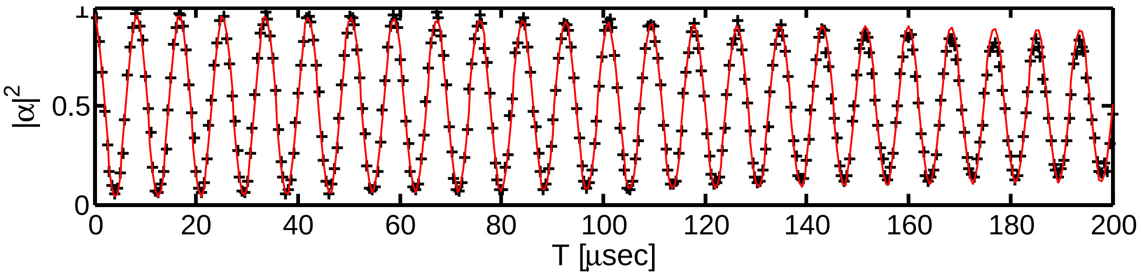

Figure 22: Zeeman qubit Rabi oscillations under regulated magnetic field by the servo system.

expansion of the ULE cavity.

2. Up to the beam fast linewidth. This linewidth is defined over a short integration time, of the order of a second, before systematic noises like thermal drifts affect the laser.
3. In the high frequency regime, up to roughly 1 MHz, which is dominated by fast phase noise of the beam.

4.6.1 Beam carrier frequency drift due to thermal variations

The ULE cavity is subjected to residual thermal variations that remain after the high thermal isolation of the hosting vacuum chamber. This noise is coupled to the 674 nm beam frequency by expansion of the cavity and shifting of its resonance frequency to which the laser is locked. Figure 23 shows the variation in the laser frequency vs the temperature in the vicinity of the cavity. The laser frequency drift is measured by the frequency of the rf signal that was introduced to the AOM, which, kept the beam in resonance with the ion transition. This, while keeping the laser locked to the cavity. The corresponding temperature values were measured by a thermistor which was mounted, inside the vacuum chamber, next to the cavity. From knowing the cavity length, the frequency response slope shows that the cavity thermal expansion coefficient is on the order of 10^{-8} °K^{-1}. This is also the ratio between the cavity change in frequency and its zero temperature resonance frequency $\Delta f/f$ per one Kelvin degree (up to a minus sign). By the second derivative of this curve we can tell that the cavity would reach it zero expansion point at temperature of 21 °C, two Celsius degrees bellow its current working temperature. Thermal variations lead to a drift, of the ULE cavity resonance frequency, in a typical rate of 10 Hz/sec. To compensate for this drift

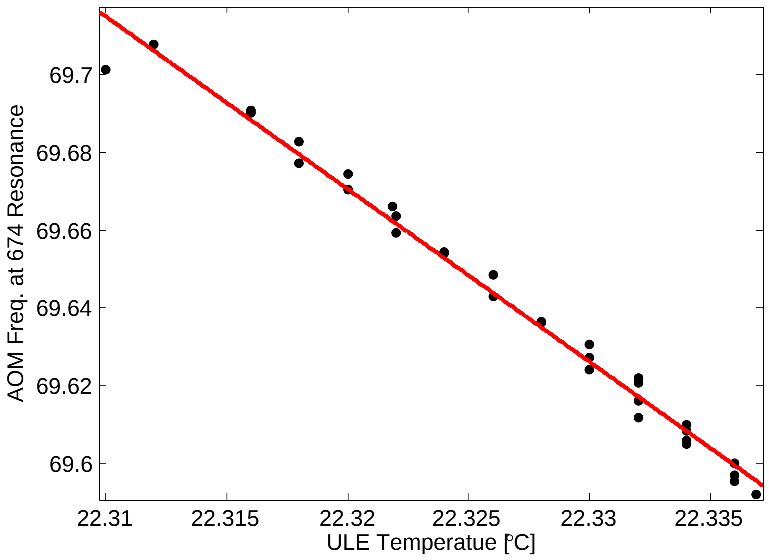

Figure 23: The 674 nm laser frequency vs. the ULE cavity temperature. The measurements were taken by tuning the beam AOM frequency to be in resonance with the optical qubit transition. This while keeping the laser locked to the cavity. Cavity temperature was measured by a nearby thermistor.

the cavity resonance was calibrated, by a periodic low-power ($\Omega \simeq 1$ kHz) scan of the optical qubit transition, by the 674 nm beam. This scan repeats every two minutes. Before every application of the 674 nm beam the current cavity resonance detuning from the qubit transition is estimated by a linear extrapolation over the most recent two consecutive calibration results. This keeps the 674 nm beam maximal off detuning from resonance within boundaries of 1 kHz.

4.6.2 The 674 nm laser fast linewidth

To estimate the 674 nm laser fast linewidth Ramsey interferometry was applied on an optical qubit. This interferometry is highly susceptible to decoherence which is induced by phase mismatch between the qubit and the manipulating radiation. Under the assumption that the beam frequency noise is stationary, the Ramsey interferometry coherence time is counter proportional to the beam fast linewidth [48].

In a Ramsey experiment the qubit is excited by two $\pi/2$ pulses that are seperated by a varying delay. For each delay time the experiment is repeated for different relative phase between the two pulses. In terms of the Bloch picture, the first pulse rotates the Bloch vector from the initial $|0\rangle$ qubit state to the equator. When the driving field and the qubit are phase matched the second pulse will rotate the Bloch vector further to the $|1\rangle$ state with an efficiency which oscillates with its phase. The amplitude of these oscillations, i.e. the fringes contrast (in analogy to two slits optical interferometry), is proportional to the phase variance that is accumulated during the wait time between the pulses. Overall, in a Ramsey interferometry, only a single π pulse is applied on the qubit. It is equivalent to a half of a Rabi nutation. Due to the short interaction time between the laser beam and the qubit, this measurement is less susceptible to the qubit population distribution between the vibration modes energy levels (as occurs in a measurement of Rabi oscillations, in section 4.5).

Figure 24 (a) shows the fringes contrast decay of an optical qubit Ramsey measurements. Insets (b) and (c) show two fringes phase scan that were taken after Ramsey arm times of 5 and 500 μsec, respectively. The fringes were recorded by scanning the second $\pi/2$ pulse phase, using the phase of rf signal which was sent to the acusto-optical frequency shifter, and measuring the qubit $|D\rangle$ state population correspondingly. These measurements are susceptible to phase noise components that their period time is of the order of the Ramsey arm time. The coherence decay half life time is due to the linewidth of the 674 nm beam fast linewidth. A 1600 μsec exponential 1/e life time indicates a laser fast linewidth of 80 Hz.

4.6.3 Fast phase noise of the 674 nm laser

Beam phase noise is an incoherent source of radiation which might couple to the qubit. For optical qubit, this noise is dominant in the servo "bumps" that are localized in two lobes around the carrier frequency. This noise is responsible for unwanted off-resonance shelving of the qubit population from the $|S\rangle$ state to the $|D\rangle$ state. Figure 25(a) shows locking circuit error signal spectrum, of the 674 nm beam, as was taken by an rf spectrum analyzer. The servo "bumps" can be easily spotted symmetrically around DC. This kind of excitation can be seen in Figure 25(b), measured on a single trapped ion. It shows the correlation between the beam phase noise energy spectrum to the population shelving around the carrier transition. Even when the carrier frequency is detuned from resonance, some portion of the noise PSD overlaps with the carrier transition and causes off-resonant shelving of population. This excitation rate is linearly proportional to the beam power.

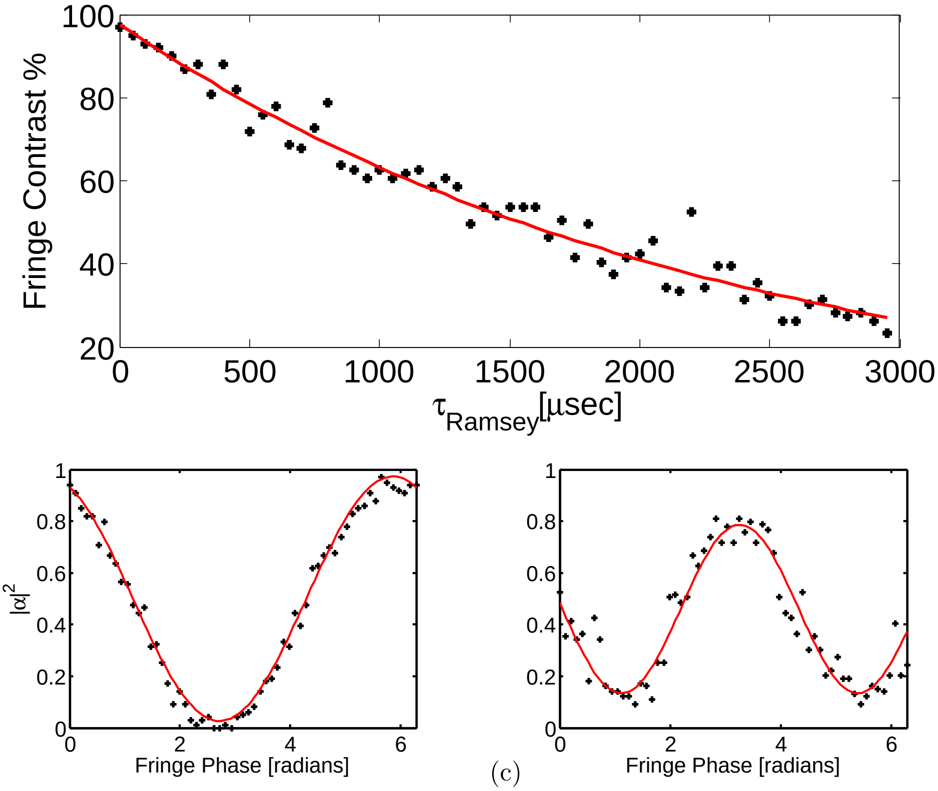

(a)

(b)

(c)

Figure 24: Optical qubit Ramsey measurements. (a) The fringe contrast decay with increase in time between the two 674 nm beam $\pi/2$ times. (b), (c) Two fringes that were taken at arm times of 5 and 500 μsec. The coherence half life time of 1600 μsec stand for a beam carrier mainlobe width of 80 Hz.

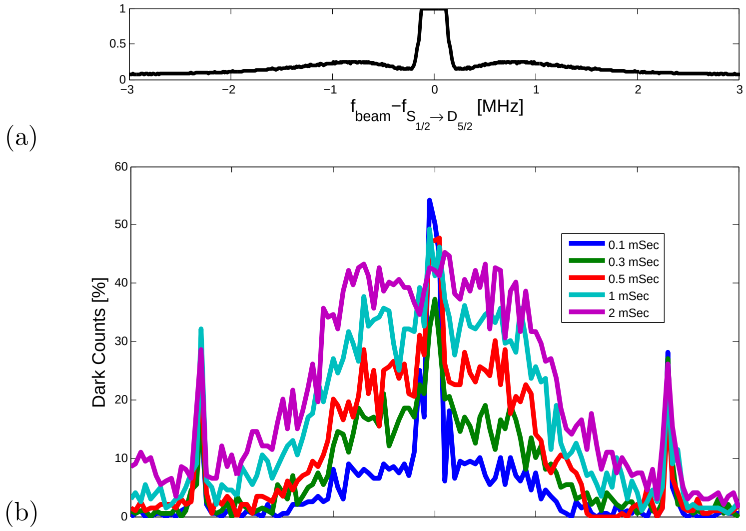

Figure 25: (a) Servo "bumps", in the laser frequency lock error-signal, that manifest the beginning of frequency oscillations due to positive feedback in the diode locking circuit. (b) Scan of the an ion $S_{1/2} \rightarrow D_{5/2}$ line by the noisy 674 beam. Phase noise shelve population while the beam carrier is off-resonance from the line.

This effect can be modeled by the theory of TLS interaction with a phase fluctuating beam [49]. The noisy phase can be introduced to the optical Bloch equations. Under the RWA these equations can be written as:

$$\begin{aligned}
\dot{\rho}_1 &= -i\frac{\Omega_0}{2}\left(e^{i\phi(t)}\rho_3 - e^{-i\phi(t)}\rho_2\right) + \Gamma\rho_4, \\
\dot{\rho}_2 &= -i\delta\rho_2 - i\frac{\Omega_0}{2}\left(\rho_4 - \rho_1\right)e^{i\phi(t)} - \frac{\Gamma}{2}\rho_2, \\
\dot{\rho}_3 &= i\delta\rho_3 + i\frac{\Omega_0}{2}\left(\rho_4 - \rho_1\right)e^{-i\phi(t)} - \frac{\Gamma}{2}\rho_3, \\
\dot{\rho}_4 &= i\frac{\Omega_0}{2}\left(e^{i\phi(t)}\rho_3 - e^{-i\phi(t)}\rho_2\right) - \Gamma\rho_4. \qquad (4.6.1)
\end{aligned}$$

Here, $\phi(t)$ it the time dependent field phase, $\rho_1 = |D\rangle\langle D|$,$\rho_2 = |D\rangle\langle S|$,$\rho_3 = |S\rangle\langle D|$ and $\rho_4 = |S\rangle\langle S|$. Figure 26 shows a result of a numerical simulation which demonstrates the dynamics of the qubit population under Eq. (4.6.1). A phase noise was generated in the simulation by filtering white Gaussian noise through band pass filter around 700 kHz with a FWHM of 180 kHz. The generated phase noise amplitude was calibrated such that the phase standard deviation was 0.6 rad. In the

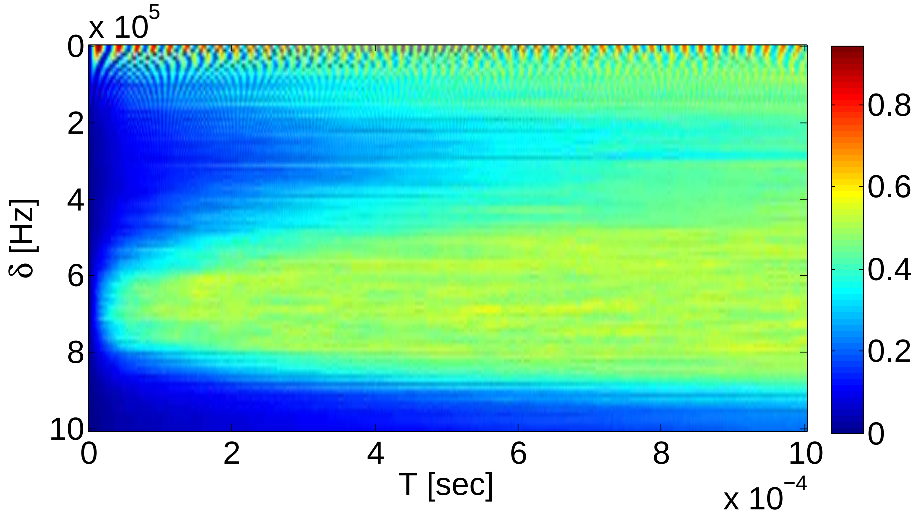

Figure 26: Simulation results of an optical qubit dynamics under the optical Bloch equations, the color values stand for the $|D\rangle$ population. Here the beam phase noise PSD was concentrated around 700 kHz. In correspondence the off-resonance shelving became dominant in this beam detuning.

simulation the qubit state was initialized to the $|S\rangle$ state, the $|D\rangle$ state population was calculated by numerically integrating the Bloch equations for varying times. The results were averaged over 100 realization of the noise signal. At low δ, far from the noise spectrum, coherent Rabi oscillations of the qubit are observed. As δ reached the noise spectrum dominant PSD the overlap between the qubit resonance and noise energy lead to gradual shelving to the $|D\rangle$ state. This transition saturates when the qubit population become roughly equally distributed between the two qubits.

4.7 Ground State Cooling

Trapped ions can be cooled beyond the Doppler-cooling limit down to, approximately, their oscillations ground state of motion ($\bar{n} = 0$ for specific trap oscillation mode). The protocol of Ground State Cooling (GSC) [8] employees rad-sideband transitions that remove phonons of the vibration mode which is being cooled. Figure 27 shows a schematic drawing of the electronic population transfer during GSC. The 674 nm beam frequency is tuned to the first vibration mode red sideband of the optical qubit carrier transition. this transition removes phonons to satisfy energy conserva-

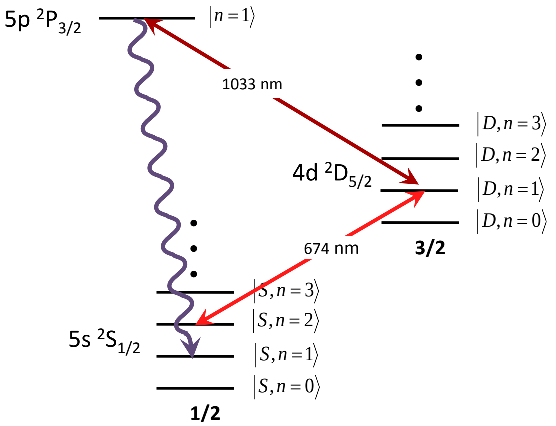

Figure 27: Schematic draw of the applied beams and the ion electronic population transfer during ground state cooling of the ion. Here $|n\rangle$ is the energy level number of the vibration mode which is being cooled.

tion with the absorbed photon. Simultaneously, the 1092 nm repumper evacuates population from the $|D\rangle$ state to the $5p^2P_{3/2}$ state. Spontaneous decay from the $P_{3/2}$ state returns the electronic population to the cooling cycle. Ground state cooling can be only initiated for ions in the Lamb-Dike regime. This ensures that the probability for vibration enhancement (i.e. transition of the type $|5p^2P_{3/2}, n\rangle \rightarrow |5s^2S_{3/2}, n \pm 1\rangle$) in a spontaneous scattering event is negligible (equal to η^2). To keep the 674 nm beam in resonance with the vibration mode red-sideband when shined simultaneously with the 1092 nm repumper one has to compensate for the light shift it induces. This shift was found, under the specified 1092 nm beam intensity, 70 kHz to the red of the $|S\rangle \rightarrow |D\rangle$ red-sideband transition frequency.

As GSC progresses the ion vibration dissipates to the ground level $|n = 0\rangle$. Therefore, the probability for phonon loss (gain) in red (blue) sideband transition decreases (increases). This is manifested by the corresponding sidelobes asymmetry in the $|S\rangle \rightarrow |D\rangle$ line spectroscopy. Figure 28 shows the emerging asymmetry in the sidelobes heights as a result of 2 msec GSC of the ion axial mode of vibration. The scanning pulse duration was 90 μsec which is the π pulse time for Rabi oscillations on the ion blue-sideband transition, as can be seen in Fig. 29 (a). The vibration mode mean occupation number can be approximately estimated by the imbalance between the two sidebands as $\bar{n} = P_{RSB}/(P_{BSB} - P_{RSB})$, where, P_{RSB} and P_{BSB} are the heights of the post-cooling mode sidelobes. Here 95% of the qubit population was in the axial vibration mode ground level and the mean occupation number of this mode was $\bar{n}_z = 0.1$.

A vibration mode heating rate, which is induced by the trap [50], can be measured by first GSC and then waiting for a variable time before measuring the sideband imbalance. The increase in $\bar{n}$ vs time can thus be evaluated. Figure 30 (a) shows the change in the axial mode red and blue sidelobes heights as the ion is heated, just by being trapped and without the application of Doppler cooling. Figure 30 (b) shows the increase in $\bar{n}$ as was deduced from the evolving asymmetry of the sidelobes. This trap heating rate was measured to be $\dot{\bar{n}}_z = 0.0158/\text{msec}$.

4.8 Zeeman qubit Ramsey interferometry

Ramsey measurements were also taken using the Zeeman qubit. Here the phase difference between the two $\pi/2$ pulses was achieved by detuning the first pulse frequency relative to the carrier. This lead to a phase drift along the measurement arm time. Unlike the optical case here the second pulse phase was not scanned but remained fixed. These measurements results show decaying oscillations due to a fluctuating magnetic field which jitters the qubit energy gap. However, this decay is due to decoherence of the qubit with respect to the coherent rf signal. Figure 31 (a) shows Ramsey fringes decay for Zeeman qubit without any effort to stabilize or account for the fluctuating magnetic fields in the lab. The coherence half life time in his case is 50 μsec. Triggering a measurement by the power line zero crossing, in Fig. 31 (b), shows an increase in the coherence half life time to $\simeq$1 msec. This is due to the fixed magnetic field, and therefore also qubit energy separation, in which all the measurements were taken. Engaging the magnetic stabilization servo system showed a coherence half life time of $\simeq$600 μsec, as can be seen in Fig. 31 (c). To stretch the qubit coherence beyond this level dynamic decoupling methods were used. By modulating the qubit Bloch vector during the Ramsey wait time a coherence time of 1.4 sec was demonstrated [51].

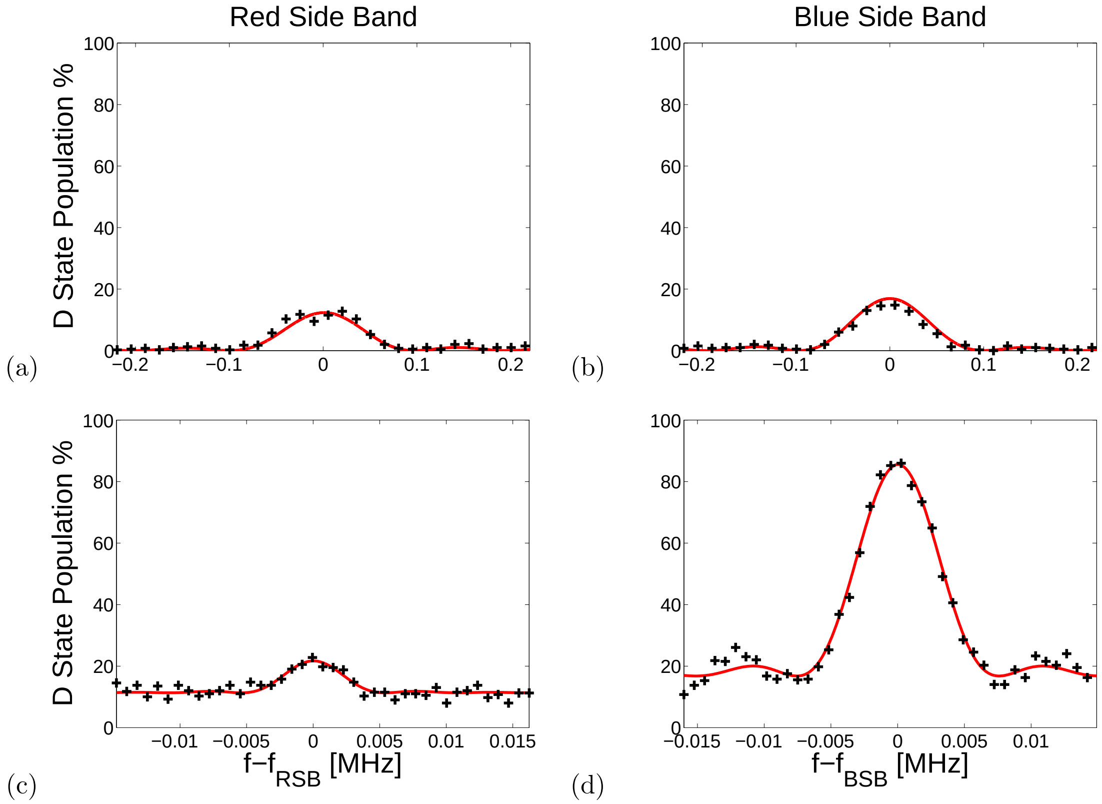

Figure 28: Cooling of a single ion to the axial vibration mode ground level. Symmetric (a) red- and (b) blue-sidebands of the vibration mode before GSC testify on equal probability for phonon absorption and emission of relatively hot state. Post GSC asymmetric (c) red- and (d) blue sidebands represent 95% occupation of the mode ground level by the ion population. The cooled sidelobes are biased by 12% shelving because of the off-resonance shelving which was induced by the long (2 μsec) shelving beam.

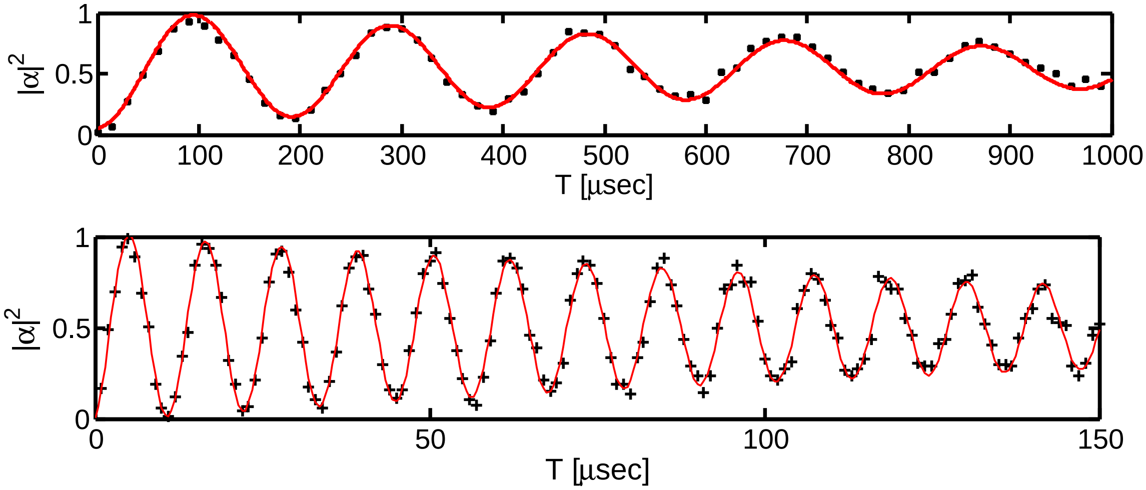

(a)

(b)

Figure 29: Ground state cooled Rabi oscillations by (a) blue-sideband transition and (b) carrier transition. Occupation, of the majority qubit population, of the ground state remove decoherence due to dispersion of the Rabi oscillations frequencies of different oscillator levels. The carrier transition coherence half life time was extended to 150 μsec.

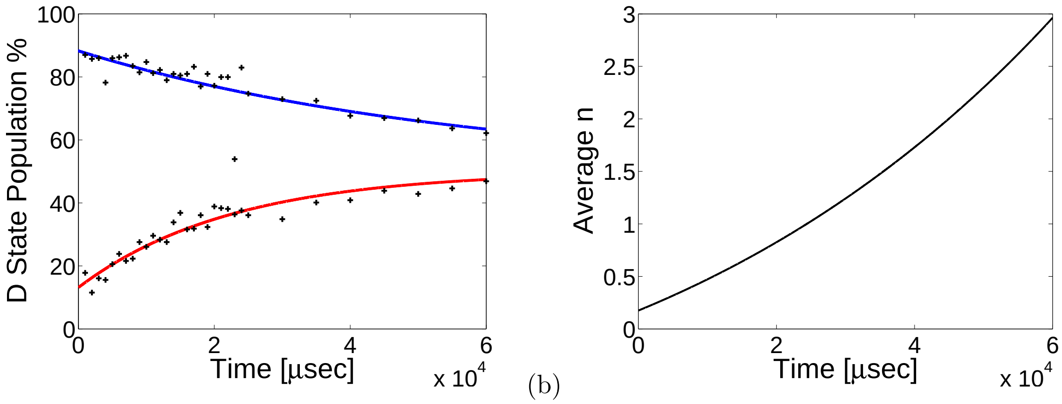

(a)

(b)

Figure 30: Trap heating rate was measured by (a) monitoring the red and blue sidbands height after GSC. (b) The raise in the vibration mode mean occupation number. Heating rate of $\dot{\bar{n}}_z = 0.0158/\text{msec}$ was measured for this trap and the vibration mode.

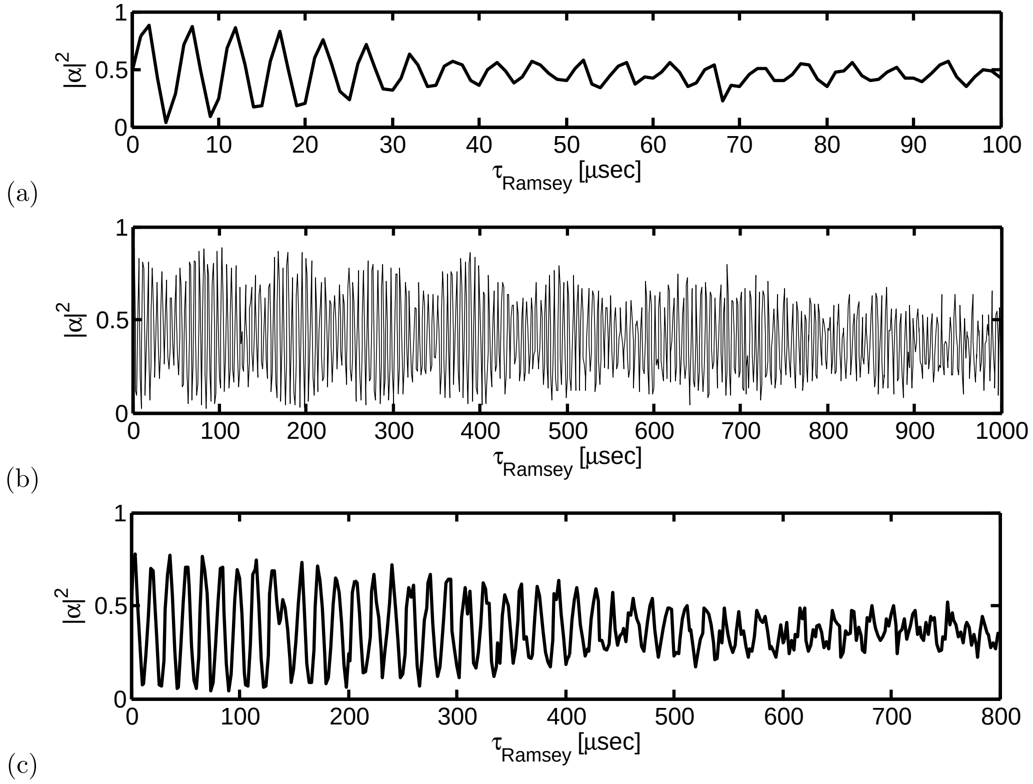

Figure 31: Ramsi measurements of the Zeeman qubit (a) without any consideration in the applied magnetic field, (2) by triggering the experiment by the grid signal and (3) when the magnetic field stabilization systems works

5 Two qubits entanglement

The paradigm of quantum computation relies on the ability to encode information into multi-qubit states. The necessary requirement for this encoding is the ability to entangle two-qubits parties. An example for such an entangling operation is the Controlled-NOT (CNOT) gate. A CNOT gate rotates, by π, one of the two qubits (the target qubit) state conditioned on the other qubit (the control qubit) state. The CNOT gate is a member in a set of gates that span every unitary operation which can be applied to the collective state of array of qubits [16]. This section describes our implementation of the Sørensen-Mølmer entangling gate which is also known as the σ_ϕ phase entangling gate and is equivalent, by single qubit rotations, to a CNOT gate. This gate is applied on two crystallized trapped $^{88}\mathrm{Sr}^+$ ions that vibrate in joint normal modes. The ions axial stretch mode is selected to negotiate between the optical qubits internal states. Following the gate, the two qubits state coherences are measured to estimate the gate fidelity. We reached a gate fidelity of 0.84 which is limited by the frequency noise of the 674 nm laser.

5.1 The Sørensen-Mølmer (σ_ϕ) entangling gate

The Sørensen-Mølmer [19, 52] entangling gate operates on an initial two qubits state $|\psi_i\rangle = |SS\rangle$ and generates the entangled state $|\psi_E\rangle = 1/\sqrt{2}\left(|SS\rangle + e^{i\phi_E}|DD\rangle\right)$, where, ϕ_E is the entanglement phase. The gate couples the $|SS\rangle$ and the $|DD\rangle$ states while destructive interference suppresses amplitude transfer to the odd parity $|SD\rangle$ and $|DS\rangle$ states. Interference is achieved by driving the ions with a state dependent force. The ions travers a different path through the phase space, conditioned on their internal state. As a result, each collective state accumulates a different geometric phase. By tuning this force magnitude one can tailor the phase difference among the eigenstates to achieve the destructive interference. This force is applied, for the gate duration T_g, by the qubits resonant beam. The gate eigenstates $|\uparrow_\phi\rangle$ and $|\downarrow_\phi\rangle$ are the eigenstates of the operator $\sigma_\phi = \cos(\phi)\sigma_x + \sin(\phi)\sigma_y$, $|\uparrow_\phi\rangle$ and $|\downarrow_\phi\rangle$ are two orthogonal states on a single qubit Bloch sphere equator, where, $|\uparrow_\phi\rangle = 1/\sqrt{2}\left(|D\rangle - e^{-i\phi}|S\rangle\right)$ and $|\downarrow_\phi\rangle = 1/\sqrt{2}\left(|D\rangle + e^{-i\phi}|S\rangle\right)$. For this reason this gate is also known as the σ_ϕ phase gate.

Practically, the gate is a pulse of the 674 nm beam which is modulated close to one of the ion crystal motional mode frequencies to generate a bi-chromatic field [22]. The beam lower (higher) frequency is red (blue) detuned from the selected vibration mode red (blue) sideband by ε. Each of the beam frequencies has a coupling strength Ω to the qubits states, since they co-propagate they share the same Lamb-Dicke parameter η with the vibration mode. The gate phase ϕ is determined by the relative phase between the two frequencies of the beam. Figure 32(a) shows a diagram which describes, using energy levels structure, the qubits population transfer by the gate. The interaction Hamiltonian between this beam and the two qubits in the presence of a single vibration mode (of frequency ω_1) is written as [53]:

$$H_I^{SM} = \hbar\Omega\left(\left(e^{-i\delta t} + e^{i\delta t}\right) e^{i\eta\left(ae^{-i\omega_1 t} + a^\dagger e^{i\omega_1 t}\right)}\left(S_+^{(1)} + S_+^{(2)}\right) + h.c.\right), \tag{5.1.1}$$

where, δ is the beam modulation frequency, $S_+^{(1)}$ and $S_+^{(2)}$ are, respectively, the spin raising operators for the 1^{st} and 2^{nd} qubits, respectively. A comprehensive analysis of this interaction influence on the qubits is given in [54]. Here a simplified aspect of this interaction, in which the beam does not couple to the qubit carrier transition, will be discussed. In the Lamb-Dicke regime H_I^{SM} can be well approximated by,

$$H_I^{SM} \simeq -\hbar\eta\Omega\left(a^\dagger e^{i(\omega_1-\delta)t} + ae^{-i(\omega_1-\delta)t}\right) S_y, \tag{5.1.2}$$

where, $S_y = S_y^{(1)} + S_y^{(2)} = \hat{\sigma}_y \otimes \hat{I} + \hat{I} \otimes \hat{\sigma}_y$ is the two qubit rotation operator around the y-axis (here $\phi = \pi/2$). This Hamiltonian eigenstates are $|+y\rangle = 1/\sqrt{2}\left(|D\rangle + i|S\rangle\right)$ and $|-y\rangle = 1/\sqrt{2}\left(|D\rangle - i|S\rangle\right)$. In this basis the qubits initial state is:

$$|\psi_i\rangle = |SS\rangle = -1/2\left(|-y,-y\rangle - |-y,+y\rangle - |+y,-y\rangle + |+y,+y\rangle\right) \tag{5.1.3}$$

The states dynamics under this Hamiltonian was solved analytically [52] using the corresponding propagator:

$$U^{SM}(t) = D\left(\alpha(t)S_y\right)e^{\Phi(t)S_y^2}, \tag{5.1.4}$$

where D is the displacement operator, α is the displacement caused by the force which is applied on the ions and is given by $\alpha(t) = (\eta\Omega/\varepsilon)\left(e^{i\varepsilon t} - 1\right)$. It can be seen that the displacement depends on the S_y eigenvalues of the gate eigenstates. This propagator displaces the qubits wavefunction in the phase space. As can be seen in Fig. 32 (b) a state motion in phase space is a circle. The ions state accumulates a phase $\Phi(t)$, where, $\Phi(t) = \eta^2\Omega^2/\varepsilon\left(t - \sin(2\varepsilon t)/(2\varepsilon)\right)$. The gate is accomplished when the entanglement between the qubits internal state and the motional state is removed, i.e. when $\alpha = 0$ at the end of a full cycle. This occurs when the gate time reaches an integer multiple of $2\pi/\varepsilon$. Then, the propagator is reduced to $U(T_g) = e^{2\pi\eta^2(\Omega^2/\varepsilon^2)S_y^2}$. By setting the beam coupling

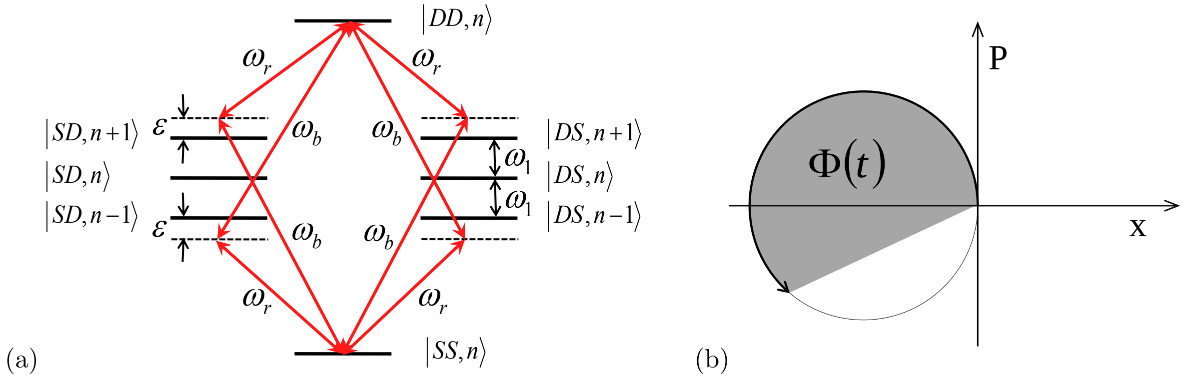

Figure 32: (a) A diagram of the bichromatic entangling beam interaction with the qubits state during the gate operation. Here $\omega_r = \omega_1 - \delta$ and $\omega_b = \omega_1 + \delta$. (b) The accumulated phase $\Phi(t)$ of the wavefunction trajectory in the vibration mode phase space. This image is in the rotating frame of the mode harmonic oscillator.

strength to $\Omega = \varepsilon/(2\eta)$ the accumulated phase during the gate operation is $\Phi(T_g) = \pi/2$. The even parity eigenstates gain a phase i relative to the odd parity eigenstates, the gate preforms [55]:

$$\begin{aligned}
|-y,-y\rangle &\rightarrow |-y,-y\rangle, \\
|-y,+y\rangle &\rightarrow i|-y,+y\rangle, \\
|+y,-y\rangle &\rightarrow i|+y,-y\rangle, \\
|+y,+y\rangle &\rightarrow |+y,+y\rangle.
\end{aligned} \tag{5.1.5}$$

As a results, the qubits internal state following the gate application is, up to a global phase,

$$|\psi_f\rangle = -1/2\left(|-y,-y\rangle - i|-y,+y\rangle - i|+y,-y\rangle + |+y,+y\rangle\right) = 1/\sqrt{2}(|SS\rangle - |DD\rangle). \tag{5.1.6}$$

The state $|\psi_f\rangle$ is a maximally entangled state, with, $\phi_E = \pi$. The gate fidelity is measured by the overlap of the qubits states with the $|\psi_E\rangle$ state, in this case $F = \langle\psi_E|\psi_f\rangle\langle\psi_f|\psi_E\rangle = 1$. Figure 33 shows the result of a numerical simulation of the qubits state ρ propagating under the entangling gate operation. For practical reasons that will be further elaborated, Fig. 33 (a) shows the probabilities $P_0 = \langle SS|\rho|SS\rangle$, $P_1 = \langle SD|\rho|SD\rangle + \langle DS|\rho|DS\rangle$ and $P_2 = \langle DD|\rho|DD\rangle$. This simulation was a numerical integration of the interaction Hamiltonian (5.1.2). Figure 33 (b) shows the gate fidelity F buildup vs. time. It can be seen that after a propagation time of $t\omega_1 = 250$ the

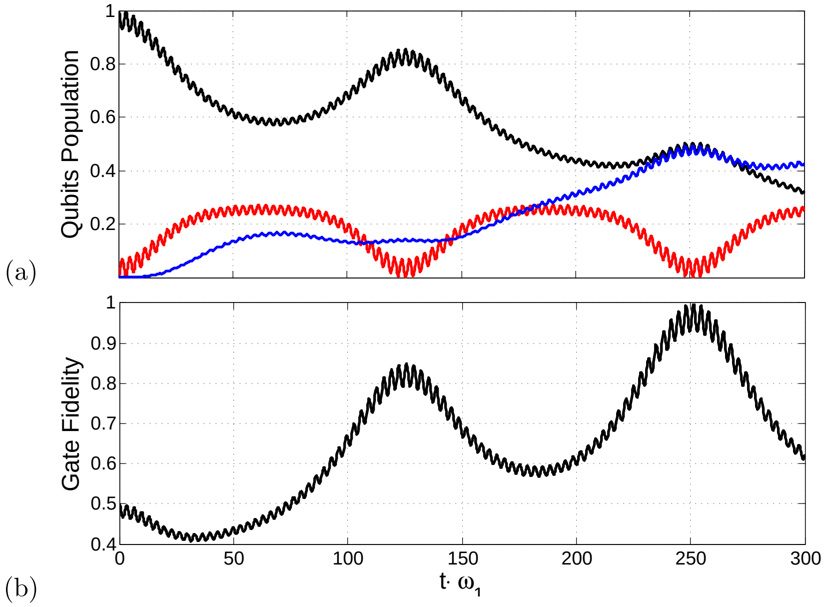

Figure 33: (a) The two qubits population p_0 (black), p_1 (red) and p_2 (blue) propagation under the Sørensen-Mølmer phase gate. These plots are the result of a numerical simulation which applied the gate propagator with the parameters: $\eta = 0.1$, $\omega_1 = (2\pi) \cdot 159$ kHz, $\varepsilon = (2\pi) \cdot 795$ Hz. $\Omega = (2\pi) \cdot 28$ kHz. (b) The gate entangling fidelity, which, reaches a maximal value of 1 at $t\omega_1 = 250$.

qubits state reaches the maximally entangled state. The fast and small oscillation, in these plots, are due to coupling between the gate beams and the carrier transition. Experimentally, until now, the maximal gate fidelity which was achieved by the optical Sørensen-Mølmer (σ_ϕ) entangling gate was 0.993 [22].

5.2 Working with two ions

The entangling gate requires two trapped ions. Generally speaking, the methods that were described for trapping, cooling an coherently manipulating a single ion are valid, as well, for two trapped ions. Even though Coulomb repulsion sets the ions a few μm apart, their equilibrium positions are covered by the laser beams. The readout process of two ions is limited for reading the p_0, p_1 and p_2 populations only. In the case of a single "bright" ion, we cannot distinguish between the $|SD\rangle$ and $|DS\rangle$ states. Figure 34 shows the detected photons histogram for readout of states superposition.

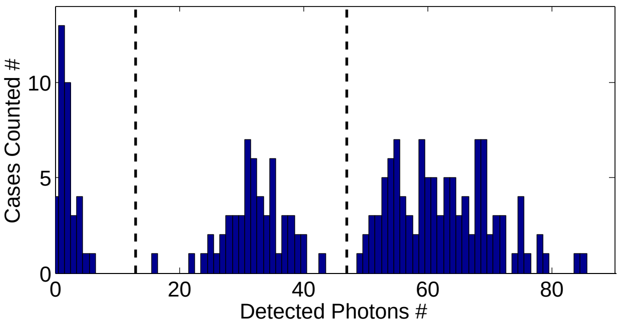

Figure 34: A histogram of detected photons number of two qubits state which is a mixed of $p_0 = 0.18$, $p_1 = 0.27$ and $p_2 = 0.54$. It was measured with 200 readout repetitions of this state. The thresholds at $n = 13$ and $n = 47$ separate the p_0, p_1 and the p_2 populations, respectively.

The three histogram lobes stand for the three different populations.

The two trapped ions crystal has six normal modes. Each of the three single-ion vibration modes becomes a center-of-mass (COM) vibration mode of the two ions crystal. Three additional modes are stretch motions where the ions oscillate out of phase and the distance between the ions oscillates. The axial stretch mode frequency is $\sqrt{3}$ times the COM axial mode frequency. Figure 35 shows the absorption spectrum of two ions near the $|S\rangle \rightarrow |D\rangle$ transition frequency. It was measured by scanning the 674 nm beam frequency and monitoring the dark counts percentage, i.e. p_2. The additional stretch modes of the crystal are manifested as additional sidelobes to the transition spectrum. Figures 36 (a) and (b) show Rabi oscillations of the two qubits populations on the carrier and the stretch mode blue sideband transitions, respectively. For the blue sideband transition these oscillations were recorded after ground state cooling of the mode. In order to avoid beating of the Rabi oscillations one has to equalize the qubits coupling to the 674 nm beam. By iterating the Rabi oscillations, while manually tuning the beam position, the beam intensities over the two ions were balanced.

5.3 The entangling gate measurement

Two optical qubits internal states were entangled by the Sørensen-Mølmer (σ_ϕ) entangling gate. The axial stretch mode was chosen for the gate bus. The trap endcaps common voltage was set to 50

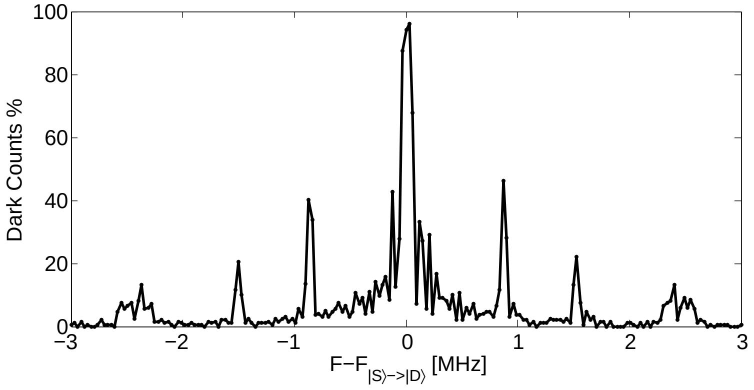

Figure 35: Absorption spectrum of two qubits $|S\rangle \rightarrow |D\rangle$ transition. Here the axial COM and stretch modes of vibration are at frequencies of 870 kHz and 1.51 MHz, respectively.

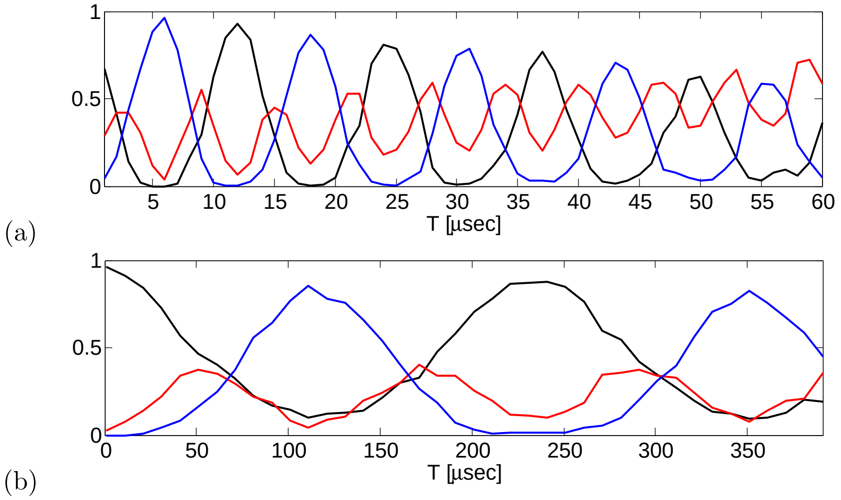

Figure 36: Rabi oscillations on the (a) carrier (b) axial stretch mode transitions. The stretch mode oscillator population was cooled to the ground state before measuring the oscillations.

V to set the axial COM and stretch vibration mode frequencies to 0.97 and 1.7 MHz, respectively. The axial stretch mode has several advantages over the COM mode for the entangling operation:

1. The heating rate of this mode is minimal since it takes large electric gradients to drive this mode.
2. This mode is spectrally further separated from the carrier transition and therefore the off-resonant shelving rate due to the 674 nm servo bump is reduced.

On the other hand, this mode Lamb-Dicke parameter, though being larger then those of the radial modes, is smaller then the Lamb-Dicke parameter of the COM mode. Before applying the gate the axial common and stretch modes populations were cooled to their ground state. The 674 nm beam was split to two frequencies by driving its acusto-optical switch by two rf signals that were 5 kHz detuned from the stretch mode sidebands. The two harmonics had an equal coupling strength to the qubit carrier transition which was $\Omega = (2\pi) \cdot 256$ kHz. The gate pulse was shaped to raise and fall smoothly in a time constant of ~ 10 μsec. This was done to minimize the effect of coupling between the gate beam to the carrier transition [54]. After initializing the qubits, the gate pulse was applied for intervals between 20 to 300 μsec. For each interval duration this procedure was repeated for 200 times for the populations p_0, p_1 and p_2 readout. Measurements results are shown in Fig. 37. The first evidence for entanglement was spotted for gate pulse duration of $T_g = 170$ μsec. There, the p_1 population reached a minimal value of $p_1 = 0.1$. The p_0 and p_2 populations were the same and equal to $\simeq 0.45$.

A complete characterization of the gate performance requires two-qubits process tomography [56]. Here we only measure the gate fidelity in achieving the target entangled state in Eq. 5.1.6. To distinguish an entangled state ρ from a mixed state one has to measure the coherences between the $|SS\rangle$ and $|DD\rangle$ states. The entangled state generation fidelity is,

$$F = \langle \Psi_E \mid \rho \mid \Psi_E \rangle = \frac{1}{2}\left(\rho_{44} + 2\rho_{14}\sin(\phi_E - \phi_{14}) + \rho_{11}\right), \tag{5.3.1}$$

where, $\rho_{11} = |DD\rangle\langle DD|$, $\rho_{44} = |SS\rangle\langle SS|$, $\rho_{14} = abs(|DD\rangle\langle SS|)$ and $\phi_{14} = arg(|DD\rangle\langle SS|)$. The coherence ρ_{14} is measured by applying, following the gate pulse, a phase varying $\pi/2$ pulse and monitoring the resulting state parity $P = p_0 + p_2 - p_1$. This parity equals:

$$P = 2Re(\rho_{23}) - 2\rho_{14}\cos(2\phi_{rot} - \phi_{14}), \tag{5.3.2}$$

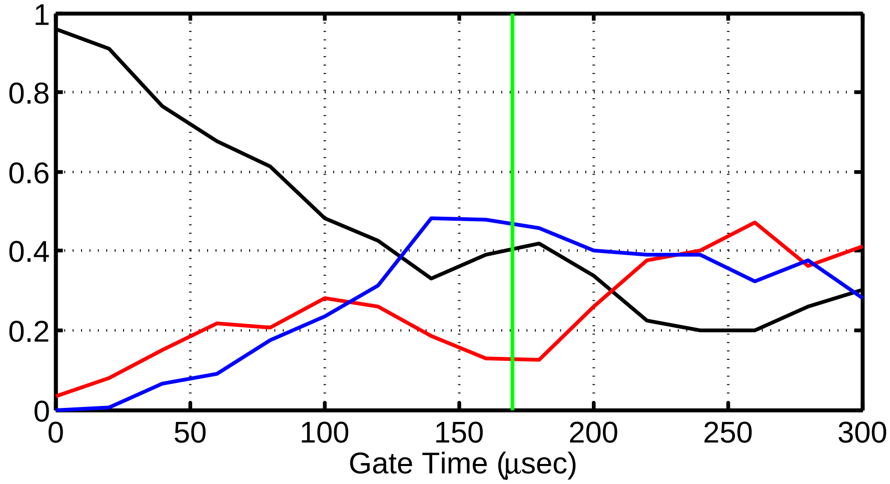

Figure 37: The two qubits population evolution under the entangling gate beam. After 170 μsec the p_1 reaches a minimal value which is a sign for entanglement. Further analysis of this state is given be parity flopping. With time, due to off-resonant shelving the qubits populations converge to a steady state.

where, $\rho_{23} = |DS\rangle\langle SD|$ is assumed to be 0 and ϕ_{rot} is the $\pi/2$ pulse phase. Hence, ρ_{14} can be extracted by measuring the parity oscillations amplitude with respect to the following pulse phase. Figure 38 shows parity oscillations that were measured after applying the entangling gate for T_g. Here $\rho_{14} = 0.39$ and the total entangling gate fidelity is $F = 0.84$.

The entangling gate performance was limited by fast phase noise and frequency drift of the 674 beam. This off-resonant population shelving rate is linearly proportional to the beam power whereas the gate time decreases at the inverse of the power square root. Servo bumps therefore cause less damage using weaker pulses and longer gates. On the other hand the accuracy with which the laser frequency has to be set should be much better than $1/T_g$. Not to suffer too much from our laser frequency drift and 1 kHz uncertainty we would like to push for stronger pulses and faster gates. Eventually, a compromise of $T_g = 170\ \mu sec$ balanced between these two contradicting requirements.

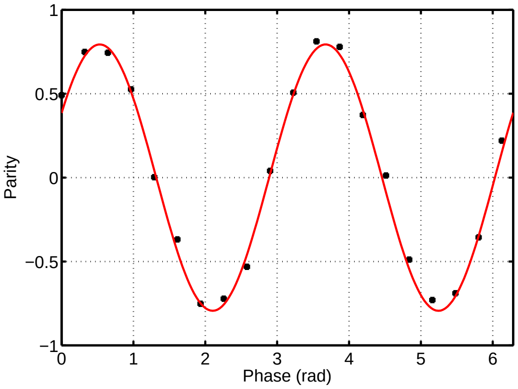

Figure 38: Parity flops of the qubits post-entangling-pulse state. These were achieved with a following phase varying $\pi/2$ pulse. The oscillations amplitude allow extracting of the coherence ρ_{14}. Gate fidelity was measured to be 0.84.

6 Emergence of a measurement basis

A single trapped ion is a well isolated, and relatively simple, system which is a good platform for investigating fundamental physical phenomena. A major class of such experiments are the realization of open quantum systems that interact with their environment. In this section we study the process of a quantum system measurement. Following a measurement the system state is projected on predefined states that compose the measurement basis. According to decoherence theory [26, 28] this basis is determined by the interaction Hamiltonian of the system and its environment. System states other then the measurement-basis states become entangled with the environment state by the interaction. When the environment degrees of freedom are traced out, these states decohere to mixed states. The measurement basis states are, on the other hand, invariant to interacting with and tracing over the environment. They are also referred to as the system-environment pointer states. This measurement mechanism is the origin of classicality in physics.

The spin of the valence electron of a single trapped ion is our quantum system. During spontaneous scattering the electron is transferred between two different orbitals, the spin state is measured only in the ground level to which the electron eventually decays. The environment with which the spin interacts are the electro-magnetic modes of 422 nm scattered photons. The spin is coupled to the environment by spontaneous emission of photons while decaying from the $P_{1/2}$ level to the ground state. In the following described experiments we excite the $S_{1/2} \rightarrow P_{1/2}$ transition, and measuring the qubit evolution as the a photon is emitted spontaneously. Measurements are analyzed for two cases: (1) Under continuous photon scattering in all directions, (2) when post-selecting a single photon scattering event with a specific $\vec{k}$-vector. In the second case it is shown that, a measurement basis emerges in the qubit Hilbert space. Quantum Process Tomography (QPT) (see appendix A) is used to analyze the qubit evolution due to the photon scattering.

6.1 Photon scattering on the $S_{1/2} \rightarrow P_{1/2}$ transition

The interaction of atoms with photons can be described by photon absorption and emission (scattering) accompanied by electronic excitation and decay on an internal transition, respectively. Here we focus on the process of spontaneous 422 nm photons scattering by a single trapped ion on its $S_{1/2} \rightarrow P_{1/2}$ transition. Since the $^{88}\mathrm{Sr}^+$ isotope has no nuclear spin, the $S_{1/2}$ and $P_{1/2}$ levels are both spin 1/2 manifolds, as can be seen in Fig. 39 (a). As will be further elaborated, absorption of $\hat{\pi}$ polarized photon flip the spin state, by π around the $\hat{z}$ axis. A Zeeman qubit which is either in the $|\uparrow\rangle$ state or the $|\downarrow\rangle$ state will not be affected by these photons absorption, as can be seen in Fig. 39 (b). Figure 39 (c) shows spontaneous photon emission decay channels of the electron spin. The electron excitation by the laser, followed by spontaneous photon emission, returns the electron to the two-fold ground-state manifold. In terms of spin evolution, spontaneous photon scattering can therefore formally be described as a non-unitary, yet trace-preserving, operation. It is therefore convenient to think of the coupling between these manifolds as a quantum map that is composed of spin 1/2 (Pauli) operators.

The electromagnetic field couples the $S_{1/2}$ and $P_{1/2}$ levels via the dipole interaction Hamiltonian, $\mathbf{H}_{int} = -e\vec{\mathbf{r}} \cdot \vec{\mathbf{E}}$, were, $e\vec{\mathbf{r}}$ is the electric dipole operator. Here we use the quantized electric field operator:

$$\vec{\mathbf{E}} = i\sqrt{\frac{\hbar\omega}{2V\varepsilon_0}} \sum_{\vec{k},E} \left(\vec{E} e^{i\vec{k}\vec{R}} \otimes \mathbf{a}_{\vec{k},\vec{E}} - \vec{E}^* e^{-i\vec{k}\vec{R}} \otimes \mathbf{a}^\dagger_{\vec{k},\vec{E}} \right), \tag{6.1.1}$$

where $\mathbf{a}_{\vec{k},\vec{E}}$ and $\mathbf{a}^\dagger_{\vec{k},\vec{E}}$ are photon annihilation and creation operators, respectively, $\vec{E}$ is the photon polarization and $\vec{k}$ is its wave-vector. Here $\vec{R}$ is the atomic center-of-mass location which determines the electromagnetic field phase, and is considered here as a classical coordinate rather than a quantum operator. In the following we will focus of the process of electron decay which is followed by photon emission. However, as will be shown later, this algebra is also valid for the process of

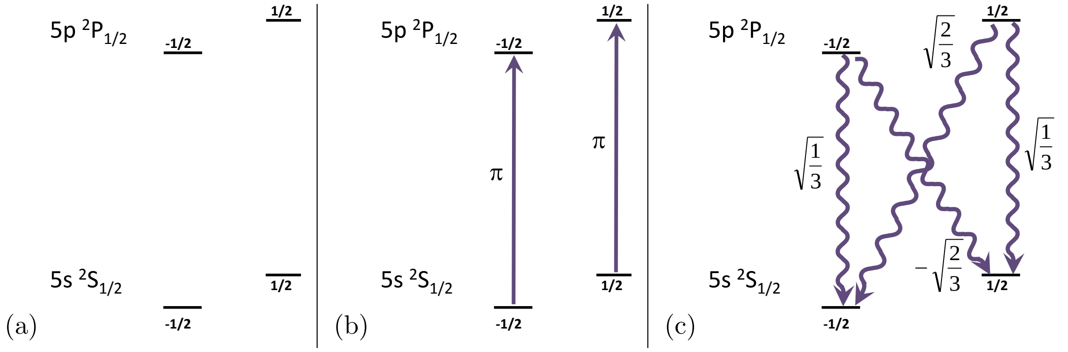

Figure 39: (a) The $J = 1/2$ manifolds of the $S_{1/2}$ and $P_{1/2}$ levels. (b) Absorption of a $\hat{\pi}$ polarized photon by the ion maps a Zeeman qubit state directly to the $P_{1/2}$ level, but changes the phase between them by π. (c) The process of spontaneous decay re-distributes the $P_{1/2}$ level population between the ground level manifold. The Clebsch-Gordan coefficient of each transition is written beside it.

photon absorption and electron excitation. The interaction Hamiltonian for photon emission can be written as:

$$\mathbf{H}_{\vec{k},emm} = ie\sqrt{\frac{\hbar\omega}{2V\varepsilon_0}}\sum_E \left(\vec{\mathbf{r}}\cdot\vec{E}^*\right)e^{-i\vec{k}\vec{R}}\otimes\mathbf{a}^{\dagger}_{\vec{k},\vec{E}}. \tag{6.1.2}$$

Note that $\mathbf{a}^{\dagger}_{\vec{k},\vec{E}}$ acts in the photonic part of Hilbert space while $\vec{\mathbf{r}}$ acts on the electronic part of Hilbert space, which is a tensor product of the electron motion and spin. The product $\vec{\mathbf{r}}\cdot\vec{E}^*$ can be written using spherical coordinates $\vec{\mathbf{r}}\cdot\vec{E}^* = \sum_q \mathbf{r}^*_q E^*_q$, where $q = \{-1, 0, 1\}$. Using the Wigner-Eckart theorem the operator components $\mathbf{r}_q$ can be reduced to

$$\langle j', m'|\mathbf{r}_q|j, m\rangle = \frac{\langle l'||\mathbf{r}||l\rangle}{\sqrt{2j'+1}}\langle l, 1; q, m|l', m'\rangle, \tag{6.1.3}$$

where, l, s and j are the orbital, spin and total angular momentum numbers, respectively. The primed variables stand for the excited states while the unprimed variables stand for the ground states. The term $\langle l, 1; q, m|l', m'\rangle$ is the Clebsch - Gordan coefficient. In this work $l = l' = 0$ and $j = j' = 1/2$, and it can be shown that the operation of the different $\mathbf{r}$ components in the spin part of Hilbert space can be written using the Pauli matrices:

$$\begin{aligned}\mathbf{r}_0 &= \sqrt{\frac{1}{2}}\sqrt{\frac{1}{3}}\langle S_{1/2}||\mathbf{r}||P_{1/2}\rangle\sigma_z,\\ \mathbf{r}_{\mp1} &= \mp\sqrt{\frac{1}{2}}\sqrt{\frac{2}{3}}\langle S_{1/2}||\mathbf{r}||P_{1/2}\rangle\sigma^{\pm} =\\ &\mp\frac{1}{2}\sqrt{\frac{1}{2}}\sqrt{\frac{2}{3}}\langle S_{1/2}||\mathbf{r}||P_{1/2}\rangle\left(\sigma_x \pm i\sigma_y\right).\end{aligned}$$

The electric field polarization components can, correspondingly, be written in Cartesian coordinates:

$$\hat{E}_0 = \hat{E}_z, \qquad \hat{E}_{\pm1} = \frac{1}{\sqrt{2}}\left(\hat{E}_x \pm i\hat{E}_y\right).$$

Plugging this to the emission Hamiltonian, at $\vec{R} = 0$ and for some fixed $\vec{k}$ gives:

$$\mathbf{H}_{\vec{k},emm} = ie\sqrt{\frac{\hbar\omega}{2V\varepsilon_0}}\langle S_{1/2}||\mathbf{r}||P_{1/2}\rangle\left[\left(\vec{\sigma}\cdot\vec{E}_1^*\right)\otimes\mathbf{a}^\dagger_{\vec{k},\vec{E}_1} + \left(\vec{\sigma}\cdot\vec{E}_2^*\right)\otimes\mathbf{a}^\dagger_{\vec{k},\vec{E}_2}\right] \tag{6.1.4}$$

This Hamiltonian implies that emission of a linearly polarized photon by the ion is followed by a spin rotation around the emitted photon polarization vector. In an experiment, measurement of the spin is conditioned on emitted photon detection. Formally, if $\mathbf{U}(t)$ is the unitary evolution then at short times $\mathbf{U}(t) = \exp(-i\mathbf{H}t/\hbar) \approx 1 - i\mathbf{H}t/\hbar \ldots$. By using a weak excitation pulse and conditioning our measurement on a single photon detection event we post-select events generated by a single application of $-i\mathbf{H}t/\hbar$. Emission of a photon with a wave vector $\vec{k}$ is described by the operator:

$$\hat{U}_{ems} = (\vec{\sigma}\cdot\vec{E}_1)^\dagger \otimes \hat{a}^\dagger_{\vec{k},\vec{E}_1} + (\vec{\sigma}\cdot\vec{E}_2)^\dagger \otimes \hat{a}^\dagger_{\vec{k},\vec{E}_2}, \tag{6.1.5}$$

where $\vec{E_1}$, $\vec{E_2}$ are the basis for the emitted photon polarization, $\hat{a}^\dagger_{\vec{k},\vec{E}_1}$ and $\hat{a}^\dagger_{\vec{k},\vec{E}_2}$ are, respectively, the creation operators of scattered photons. This operator is applied on the wavefunction $|\Psi\rangle = |\psi\rangle \otimes |0\rangle_{\vec{k}}$, where, $|\psi\rangle$ is the spin initial state and $|0\rangle_{\vec{k}}$ stands for a vacuum state of the photons mode with that specific $\vec{k}$-vector. Correspondingly, a single photon absorption applies the operator

$$\hat{U}_{abs} = (\vec{\sigma}\cdot\vec{E}_i) \otimes \hat{a}_{\vec{E}_i} \tag{6.1.6}$$

to the spin-photon wavefunction, where, $\vec{\sigma}$ is a Pauli matrices vector, $\vec{E}_i$ is the incident photon electric field and $\hat{a}_{\vec{E}_i}$ is the incident photon annihilation operator. The two-qubit (spin and photon) initial wavefunction, before the scattering process, is defined as $|\Psi\rangle = |\psi\rangle \otimes |1\rangle_i$, where, $|1\rangle_i$ stands for a single incident photon. For $\hat{\pi}$ polarized photons this operator can be written as

$$\hat{U}_{abs} = \sigma_z \otimes \hat{a}_{\vec{E}_z}, \tag{6.1.7}$$

which, clearly, rotates the electron spin around the $\hat{z}$ axis following photon absorption.

6.2 Continuous photon scattering

We start with measurement of the ion spin state evolution when photon are shown continuously scattered in random directions. This experiment geometry and axes are shown in Fig. 40 (a). A comprehensive analysis of the process is achieved by QPT of the spin evolution following scattering of a 422 nm photons. The measurements were taken in the following steps:

1. The qubit was optically pumped to the $|\uparrow\rangle$ state and either remained there or, by a consecutive rf pulse, was brought to one of the $|\downarrow\rangle$ (by a π pulse), $|\hat{x}\rangle = 1/\sqrt{2}(|\uparrow\rangle + |\downarrow\rangle)$ (by a $\pi/2$ pulse) and $|\hat{y}\rangle = 1/\sqrt{2}(|\uparrow\rangle + i|\downarrow\rangle)$ (by a $\pi/2$ pulse at 90° delay relative to $|\hat{x}\rangle$) states. The pulse frequency was on resonance with the Zeeman manifold splitting which was 3.5 MHz due to a static magnetic field of 1.25 Gauss.
2. A 422 nm, $\hat{\pi}$ polarized, beam pulse excited the electron to the $P_{1/2}$ level. The pulse power was was calibrated, in a pre-preformed experiment, to scatter a single photon, on average, for an exposure time of 3.9 μsec.
3. The qubit state was measured on either one of the $\hat{z}$, $\hat{x}$ and $\hat{y}$ bases. Measurements in the $\hat{x}$ and $\hat{y}$ bases were preformed by applying a rf pulse on the qubit, in an opposite phase to the corresponding state initialization pulses, before the qubit readout.

The excitation pulse duration was scanned between the times that are required for scattering 0.1 to 3 photon on average. For each pulse time 12 different measurement types (the four initial states times the three measurement axes) were taken. Figure 41 (a-c) shows QPT results for pulse durations for scattering of 0.03, 0.34 and 0.65 photons on average. The reconstructed scattering process matrix χ allows for the reconstruction of the post-scattering state of every initial spin state. The figure insets show collapse of the Bloch sphere, which represents all the initial pure state, to the sphere center. It can be seen that, in this case, the collapse of the initial symmetric sphere along the $\hat{z}$ axis is faster then on the sphere equator. This implies that the qubit superposition is ruined faster then its coherence due to photons scattering. The qubit decoherence can be considered as the consequence of superposition of many scattering events, each with its own photon $\vec{k}$ vector and polarizations. The qubit state is flipped by each scattering event around a random axis and, on average, converges to the sphere origin.

The qubit decoherence rate was quantified with a Ramsey experiment. In this measurement, between the two Ramsey $\pi/2$ pulses, an excitation pulse was applied. Figure 41 (d) shows the decay in the Ramsey fringes contrast with respect to the excitation pulse duration. This decay is proportional to the collapse of the qubit Bloch sphere equator. The coherence half life time was measured to be equivalent for the excitation pulse duration which is needed for scattering 0.6 photons.

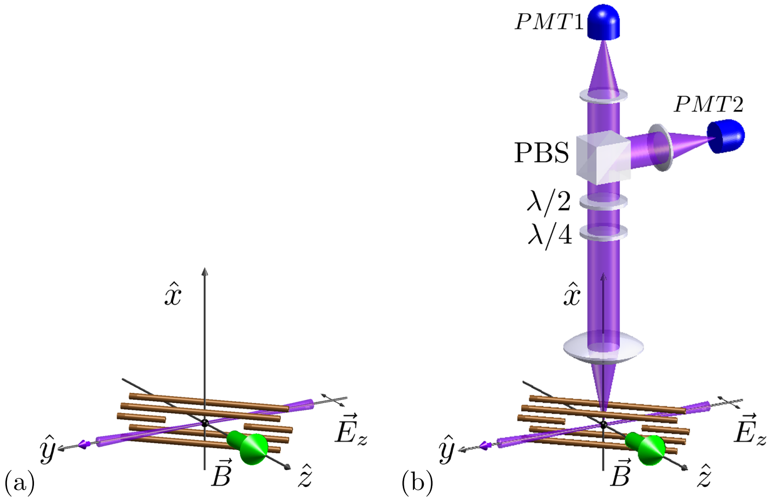

Figure 40: Two demonstrations of the scattering photons experiments. In the case of continuous and isotropic photon scattering (a) the scattered photon direction of propagation was ignored. For the single scattering mode measurement (b) the imaging system was "introduced". Only scattering events that lead to photon detection were post-selected.

6.3 Post selected single-photon scattering events

The case in which a single photon was scattered with a well defined $\vec{k}$-vector was isolated. Here it is done by post-selecting events where a single scattered photon was detected, i.e. was scattered toward the imaging system objective along the $\hat{x}$ axis, as can be seen in Fig. 40 (b). In this special case the scattered photon $\vec{k}$-vector is perpendicular to both the direction of the absorbed photon

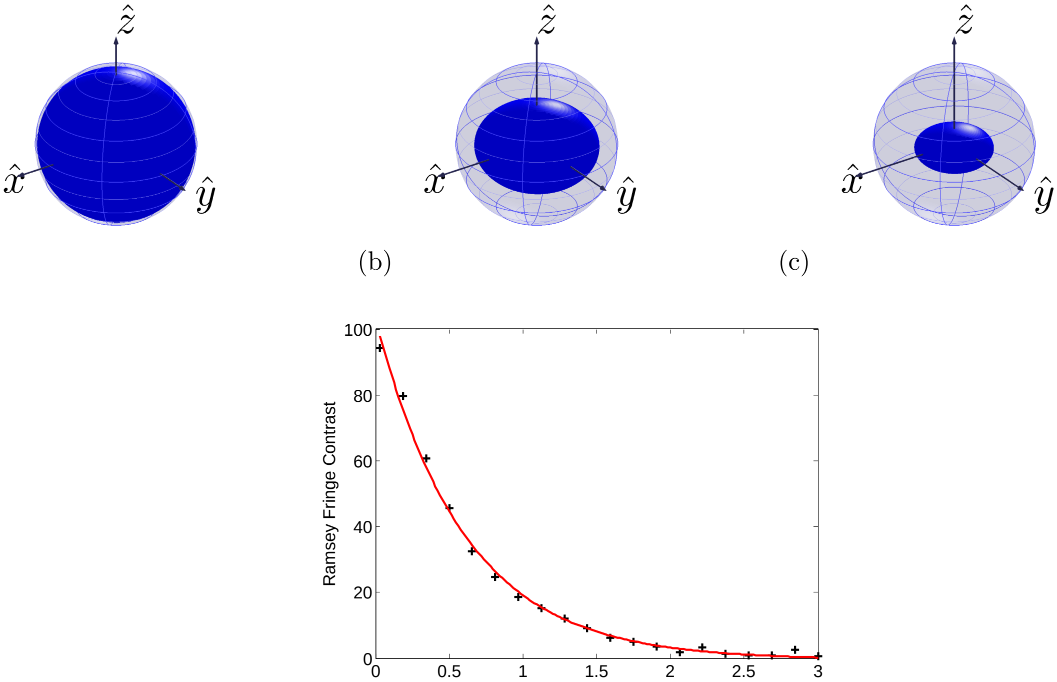

(a) (b) (c)

(d)

Figure 41: Single spin Bloch sphere collapse after scattering. Here we show the surface onto which all pure spin states are mapped after (a) 0.03, (b) 0.34, (c) 0.65 photons were scattered on average. (d) Ramsey fringes contrast as function of the exposure time of the ion to the excitation beam, Calibrated by the average number of scattered photons. The half time of the qubit coherence was equivalent for the time for scattering 0.6 photons. The Ramsey fringe contrast is equal to the Bloch spheres radius in the XY plane.

and its polarization. We expect a pointer basis to emerge for any $\vec{k}$-vector direction of the scattered photon. To see this, it is instructive to study the reduced spin evolution using a circular photon polarization basis. The two spin operators that correspond to the scattered photon polarization components in Eq. 6.1.5, $\vec{\sigma} \cdot \vec{E}^*_{\pm} = \sigma_{\mp}$, are the spin ladder operators in the $\vec{k}$ direction. This means that spin states that initially point along the emitted photon propagation direction can emit circularly polarized photons but only with the helicity parallel their spin. Following emission of a circularly polarized photon, the spin direction reverses but remains aligned with the photon $\vec{k}$ vector. This is a simple manifestation of angular momentum conservation in the photon emission process. Using the spin $\vec{k}$ direction and circular photon polarization as a basis, the combined spin-photon state following scattering can be written as,

$$U_{ems}(\alpha|\hat{k}\rangle + \beta|-\hat{k}\rangle) \otimes |0\rangle_{\vec{k}} = \alpha|-\hat{k}\rangle \otimes |E_+\rangle_{\vec{k}} + \beta|\hat{k}\rangle \otimes |E_-\rangle_{\vec{k}}. \tag{6.3.1}$$

Here $|\pm\hat{k}\rangle$ represent states of a spin pointing in the $\pm\hat{k}$ direction and $|E_\pm\rangle_{\vec{k}}$ represent states of a single, right or left circularly polarized, photon with wave vector $\vec{k}$.

Spin states pointing in the $\hat{k}$ direction therefore constitute a good pointer-state basis. They are classically correlated with the emitted photon polarization, whereas any superposition of such states becomes entangled with it. Starting from a superposition of spin pointer states and tracing over the scattered photon polarization the spin state will evolve into a statistical mixture. When starting in this spin direction, however, photon scattering, theoretically, does not induce entropy increase [26].

In our setup configuration, to evaluate spin evolution in the full scattering process, one has to account for photon absorption as well (Eq. (6.1.7). The spin-photon combined state evolves under,

$$\begin{aligned} U_{int} &= \sigma_{(+,x)}\sigma_z \otimes a^\dagger_{\vec{k},\vec{E}_+} + \sigma_{(-,x)}\sigma_z \otimes a^\dagger_{\vec{k},\vec{E}_-} \\ &= |-\hat{x}\rangle\langle -\hat{x}| \otimes a^\dagger_{\vec{k},\vec{E}_+} + |\hat{x}\rangle\langle \hat{x}| \otimes a^\dagger_{\vec{k},\vec{E}_-}, \end{aligned} \tag{6.3.2}$$

where $\vec{\sigma}_{(\pm,x)} = \sigma_y \mp i\sigma_z$ are the spin raising and lowering operators in the $\hat{x}$ direction, $|-\hat{x}\rangle = 1/\sqrt{2}(|\uparrow\rangle + |\downarrow\rangle)$. The spin of the ion is therefore projected along the emitted photon direction every time a photon with a circular polarization is detected. The post-scattering spin state, calculated by tracing over the scattered photon degrees of freedom, is

$$\rho_{spin} = |\alpha|^2|\hat{x}\rangle\langle\hat{x}| + |\beta|^2|-\hat{x}\rangle\langle -\hat{x}|. \tag{6.3.3}$$

Here α and β, are the initial spin amplitudes in the $\hat{x}$ and $-\hat{x}$ directions respectively. Equation (6.3.3) represents, in general, an incoherent mixture of states, into which the initial spin states evolve. It suggests that the spin state will decohere unless it is initialized in the $|\hat{x}\rangle$ or $|-\hat{x}\rangle$ states. In the Bloch sphere geometric representation this operation maps the surface of the sphere onto the $\hat{x}$ axis.

We monitored this collapse of the Bloch sphere using QPT, conditioned on a scattered photon detection. In these measurements the excitation beam was a weak, 100 nsec, 422 nm pulse. The ion scattered a photon from this beam with a probability between 0.05-0.1. This working point was set to minimize the probability for multi photons scattering before detection. The imaging system PMTs were gated simultaneously with the excitation pulse to minimize the number of false dark counts (typical dark counts rate per PMT is 100 Hz). The imaging system objective collects roughly 1% of the scattered photons. The overall detection efficiency of scattered photons (including elements transmission and the PMTs quantum efficiency) was measured to be roughly 1/400. The excitation pulse had to be repeated for 6000 times, on average, for detection of a single photon. In all the following measurements, we post-selected only those repetitions of the experiment where the PMTs indicated that a single photon was recorded. In 85-90% of these events a single photon was indeed scattered, whereas in the remaining 10%-15% of events detection was generated either by a dark count of the PMT or a single detected photon out of a scattered pair.

Figure 42 shows the results of QPT of a single spin (Zeeman qubit) collapse following the scattering of a single photon toward the imaging system. Typically, process tomography is performed in a frame of reference that is rotating along with the spin. However, spin evolution due to photon scattering is determined by directions in the lab frame of reference. To faithfully perform state tomography in the lab frame we perform state tomography stroboscopically with the spin Larmor precession. To this end, rather than analyzing all recorded events, we limited our analysis to events that occurred within a $2\pi/32$ radian phase interval. The direction of the spin at the moment of scattering in these events was spread over an angular span which equals this phase interval around the $\hat{x}$ direction. Choosing other phase intervals of similar width yield identical results that are rotated around $\hat{z}$ as is shown in section 6.3.1. In these limits, experiments were repeated until 900 successful repetitions, i.e. ones in which a photon was detected, were recorded for each measurement type (the combination of the spin initial state and the post-process measurement basis). Figure 42(a) plots the absolute value of the entries of the reconstructed process matrix. It is written using the basis elements $|\hat{x}\rangle\langle\hat{x}| = (I+\sigma_x)/2$, $|-\hat{x}\rangle\langle-\hat{x}| = (I-\sigma_x)/2$ (projections on the $|\pm\hat{x}\rangle$ states), $-i\sigma_y$ and σ_z. In agreement with Eq. (6.3.2), the process matrix is found to be mostly composed of nearly equal contributions of projections on the $|+\hat{x}\rangle$ and $|-\hat{x}\rangle$ states.

The reconstructed process matrix can be used to evaluate all the post-scattering spin states. Geometrically these states are represented by a surface onto which the Bloch sphere collapses, shown in Fig. 42(b) and Fig. 42(c). An elongated ellipsoid clearly marks the emergence of a spin measurement basis. Here we have chosen the direction along which the pointer basis emerges to be the $\hat{x}$ axis, thus coinciding this coordinate system with the lab coordinate system, shown in Fig. 40

(b). Discussion of this ellipsoid shape is given in subsection 6.3.2.

The amount of spin decoherence due to photon scattering can be quantified by calculating the von Neumann entropy of post-scattering states; $S(\rho) = -\mathrm{Tr}[\rho \ln(\rho)]$. Furthermore, in decoherence theory, a criteria for pointer states is that their entropy does not increase due to their coupling to the environment. We calculated the entropy of all reconstructed final states. Figure 42(d) shows a color map of this final-state entropy plotted over the Bloch sphere of the corresponding initial states. As seen in the figure, spin states along the $\hat{x}$ direction indeed experience the minimal increase in entropy.

6.3.1 Process tomography in the lab frame of reference

The ion electronic spin preforms Larmor precession around the static magnetic field direction. In a frame rotating with the spin, the lab axes $\hat{x}$ and $\hat{y}$ rotate around the $\hat{z}$ axis at the Larmor precession frequency of 3.5 MHz. The detected photon scattering direction however is fixed by the setup imaging system, in the lab frame. Therefore, to observe the Bloch sphere collapse on a basis aligned with the detected photon $\vec{k}$-vector direction we preformed process tomography, in the lab frame of reference, stroboscopically with the spin precession rather than in a frame rotating with it. A local oscillator, which was synchronized with the spin rotation frequency, triggered the rf pulses with which we preformed spin rotations and was used to generate the pulse. The spin direction within the Larmor precession cycle at the time the photon was scattered was estimated by the local oscillator phase at the photon time of detection. It is extracted by a time-to-amplitude converter (TAC) which is periodically reset by the local oscillator zero crossing, and triggered by the PMT whenever a photon is detected. Figure 43 shows the distribution of local oscillator phases recorded at different photon detection events, spanned between 0 to 2π radians. Here 2π corresponds to a delay of 285 nsec between the local oscillator zero crossing and the photon detection event. Restricting process tomography to events that occurred during a given phase window results in a collapse of the Bloch sphere on an elongated ellipsoid. The lower part of Fig. 43 shows the different ellipsoids that result from post-selection of different phase windows marked by the different colors. The main axis of the resulting ellipsoids lies in the sphere equatorial ($\hat{x}$-$\hat{y}$) plane. The angle of the ellipsoid main axis from the $\hat{x}$ axis is given by the mean phase in the phase acceptance window.

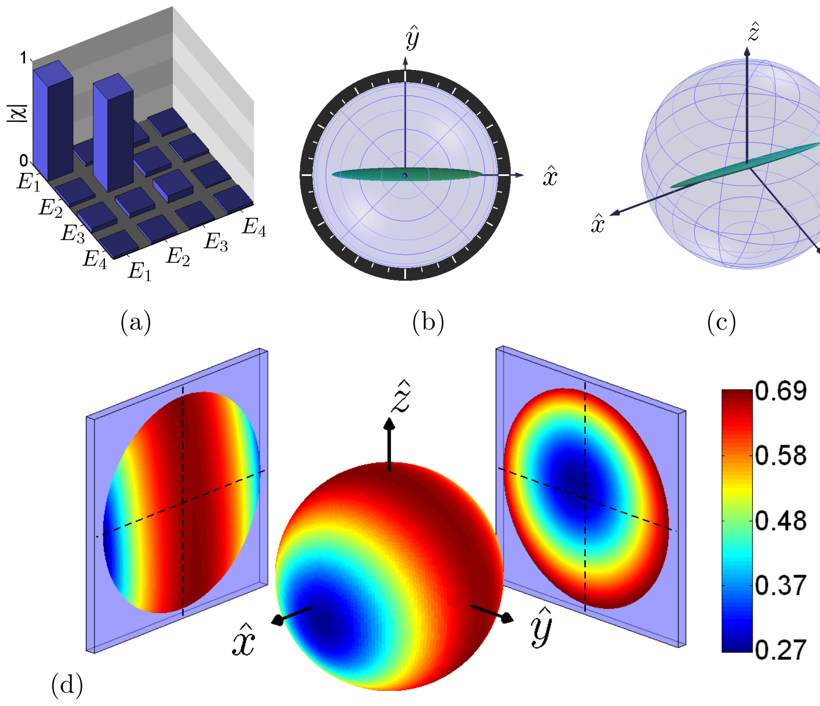

(a) (b) (c)

(d)

Figure 42: Collapse of the Bloch sphere.(a) The absolute value of the elements of the reconstructed process matrix. The basis used here is $E_1 = |\hat{x}\rangle\langle\hat{x}| = (I + \sigma_x)/2$, $E_2 = |-\hat{x}\rangle\langle-\hat{x}| = (I - \sigma_x)/2$ (projections on the $|\pm\hat{x}\rangle$ states), $E_3 = -i\sigma_y$ and $E_4 = \sigma_z$. As seen, the process is mainly composed of equal contributions of projections on the $\hat{x}$ direction. Two view points; (b) along the z axis and (c) at 45° to the $\hat{z}$ axis of the surface on which the Bloch sphere of initial spin states collapses, following photon scattering. The resulting elongated ellipsoid, clearly marks the emergence of a spin measurement basis. (d) The von Nuemann entropy of post-scattering spin states. This is also the increase in entropy due to photon scattering. The states on the tip of the emergent basis (pointer states) acquire the minimal amount of entropy, in accordance with the predictability sieve criteria in decoherence theory. Equal superpositions of pointer states, on the other hand, acquire almost the maximal possible entropy demonstrating that, without any knowledge on the scattered photon, the process of photon scattering is in general irreversible.

6.3.2 Characterization of the pointer states ellipsoid

The pointer states ellipsoid in Fig. 42(b) has an aspect ratio of 1:11 between its axes on the equator surface. This ratio is dictated by the width of the local oscillator phase acceptance window, the

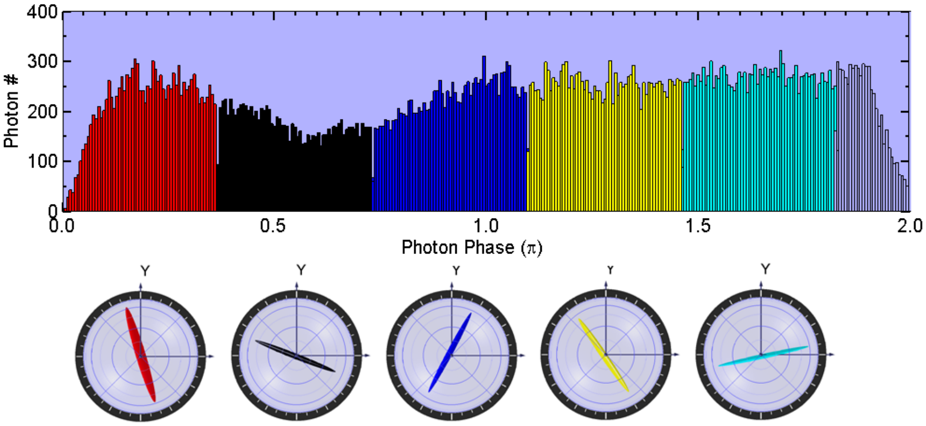

Figure 43: The distribution of spin Larmor precession phases at photon detection times. This distribution was divided to five phase windows marked by the different colors. Preforming QPT using events that were post-selected from each group yields the corresponding ellipsoids shown on the bottom part of the figure. All ellipsoids lie largely in the x-y plane, and the angle of their main axis from the x direction equals the average phase in the selected window.

finite N.A. of our photon collection lens and quantum projection noise. Figure 43 shows the surface on which the Bloch sphere is projected as a function of the phase acceptance window width, which is marked in magenta on the corresponding distributions. As seen, the aspect ratio of the ellipsoid tends to one when the phase acceptance window is large enough. When all phases are accepted the resulting ellipsoid is a disk in the equatorial plane [57]. The width of all spheroids in the $\hat{z}$ direction is roughly consistent with projection noise. To model the process matrix following scattering of a single photon we average the ideal process matrix $\chi_{\vec{k}(\theta,\phi)}$ over different photon scattering directions in the rotating frame. This matrix describes the process which is applied on the spin given that a photon was scattered in the $\vec{k}\,(\theta,\phi)$ direction. In the $\{I,\sigma_x,-i\sigma_y,\sigma_z\}$ basis [58] it is defined as:

$$\chi_{\vec{k}(\theta,\phi)}=\frac{1}{4}\begin{bmatrix} a & b & c & 0 \\ b^{*} & d & e & 0 \\ c^{*} & e^{*} & f & 0 \\ 0 & 0 & 0 & 0 \end{bmatrix},$$

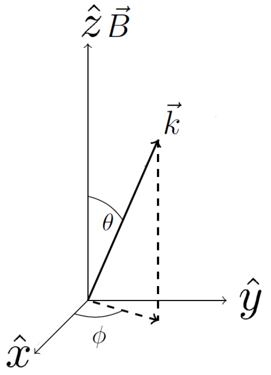

Figure 44: $\vec{k}$-vector orientation in the lab frame of reference.

where,

$$
\begin{aligned}
a &= 2\sin^2(\theta) \\
b &= i\sin(2\theta)\sin(\phi) \\
c &= -\sin(2\theta)\cos(\phi) \\
d &= 2\cos^2(\phi) + 2\cos^2(\theta)\sin^2(\phi) \\
e &= i(\sin(2\phi)\cos^2(\theta) - \sin(2\phi)) \\
f &= 2\cos^2(\phi)\cos^2(\theta) + 2\sin^2(\phi).
\end{aligned}
$$

Here θ and ϕ are the the scattered-photon $\vec{k}$-vector nutation and precession angles, respectively, relative to the $\hat{z}$ axis, as can be seen in Fig. 44. Photons are collected through our imaging system numerical aperture (NA) of 0.31. This result in a $\vec{k}$-vectors distribution, furthermore, the size of the phase acceptance window $[-\phi_{LO}{:}\phi_{LO}]$ determines the width of a square distribution of scattering directions in the rotating frame.

$$\chi_{scatt} = \int_{-\phi_{LO}}^{\phi_{LO}} d\phi' \int_{-\theta_{max}}^{\theta_{max}} d\theta' \chi_{\vec{k}(\theta',\phi')}. \tag{6.3.4}$$

Here θ' and ϕ' are the spherical angles (starting at $\hat{x}$ for $\theta' = \pi/2$ and $\phi' = 0$) and $\theta_{max} = \pi/2 + \sin^{-1}(NA)$ is the maximally possible scattered photon $\vec{k}$-vector orientation to be detected. Figure 46 shows the aspect ratio of the ellipsoid in the equatorial plane. Solid line is calculated using Eq. 6.3.4 and red crosses are given by a fit of and ellipsoid surface to the data shown in Fig. 45 (a)-(k). The two are seen to be in a good agreement.

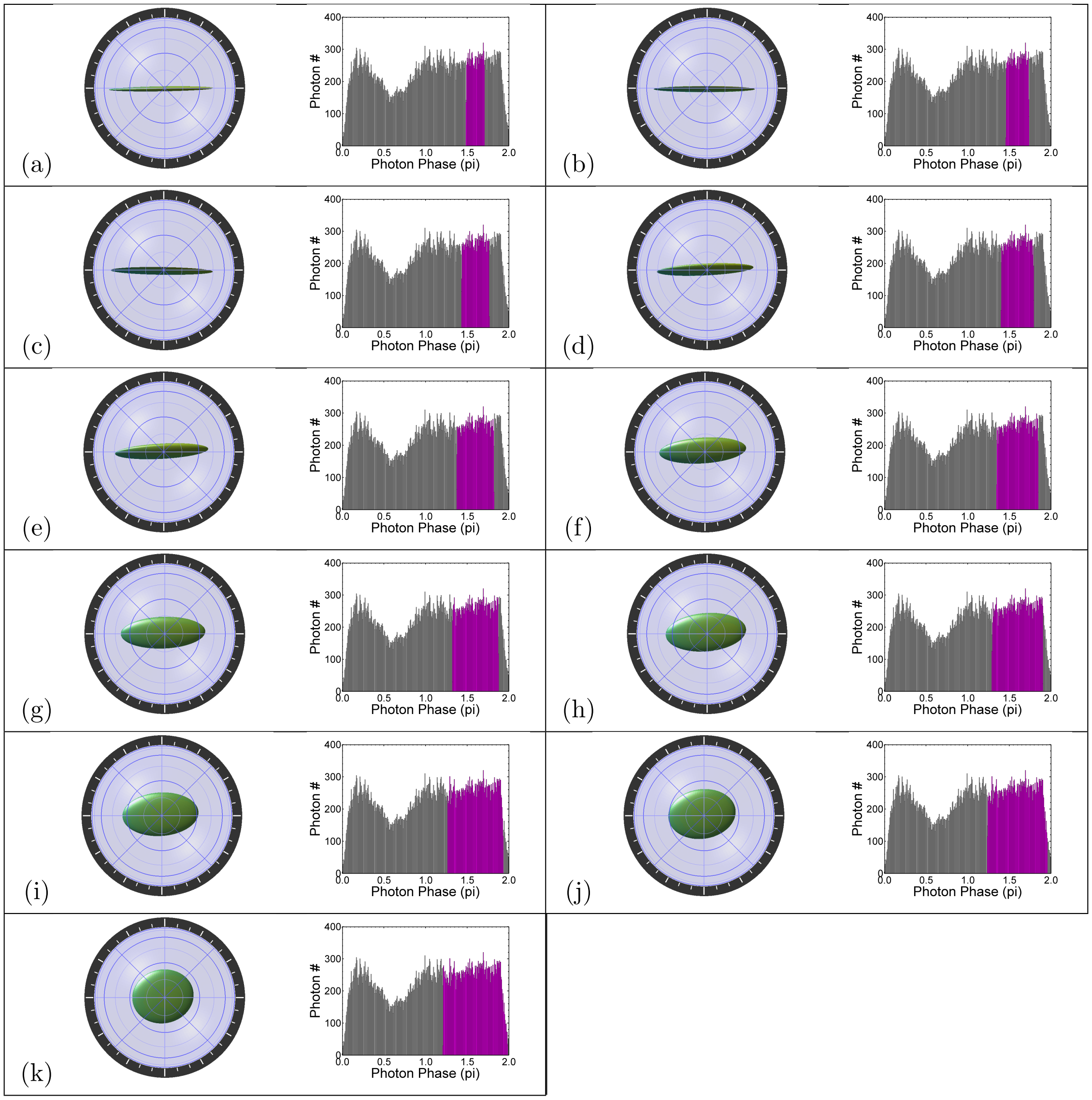

Figure 45: The measured ellipsoid shape vs the the scattered photons phase range. The figures are given for a phase range of (a)40° (b)50° (c)60° (d)70° (e)80° (f)90° (g)100° (h)110° (i)120° (j)130° (k)140°. Marked in purple are the corresponding photon phase window.

6.4 Measurement Basis emergence

In order to prove that the $|\pm\hat{x}\rangle$ states on the poles of the emerging ellipsoid are a measurement basis, one needs to show that these states are classically correlated with the scattered photon polarization.

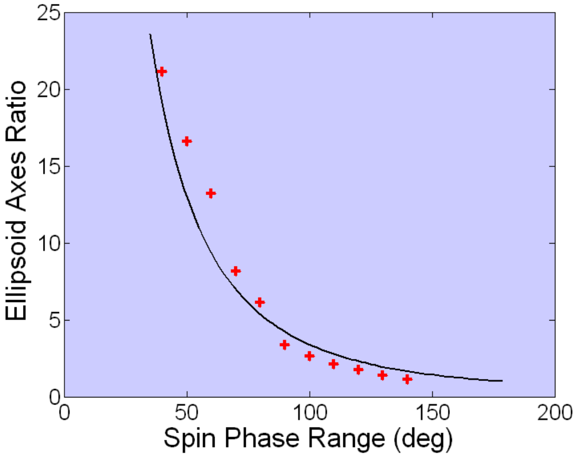

Figure 46: The measured ellipsoid aspect ratio, in the $\hat{x}-\hat{y}$ plane, vs the scattering events phase range. Red crosses show measurements. The black line is a numerical simulation result.

For this purpose, we analyzed the polarization of photons that were scattered by different initial spin states. According to Eq. 6.3.2, the $|\pm\hat{x}\rangle$ states scatter photons with a pure circular polarization, whereas other initial spin states become entangled with the photon polarization. The later case leads to a statistical mixture of photon polarization measurement outcomes.

Figure 47 shows the results of our photon polarization measurements. For these measurements we used the polarization analysis components of the imaging system that include the PRU and PBS as can be seen in Fig. 8 (b). The quarter-wave retardation plate was aligned such that it transformed the $|E_{\pm}\rangle$ states to an orthogonal linear basis. The proceeding half-wave plate rotated this linear polarization with respect to the PBS basis. The two PMT monitored the two PBS ports. Figure 47(a) shows the probability of photon detection on a given port of the PBS vs. the half-wave plate rotation angle. Here, the spin is initialized to the $|\hat{x}\rangle$ (red filled circles) or $|-\hat{x}\rangle$ (black filled circles) states. As expected from a pure polarization state, this probability sinusoidally oscillates as the polarization is rotated. The blue and magenta solid lines are a sinusoidal fit to our data. Furthermore, whenever the two wave-plates transform the emitted circular polarization to match the PBS basis, a clear correlation between the measured polarization and the initial spin state is observed. For example, at a half-wave plate rotation angle of 57 degrees, indicated by the vertical dashed line, a 0.75 correlation between the PMT on which the photon was detected and

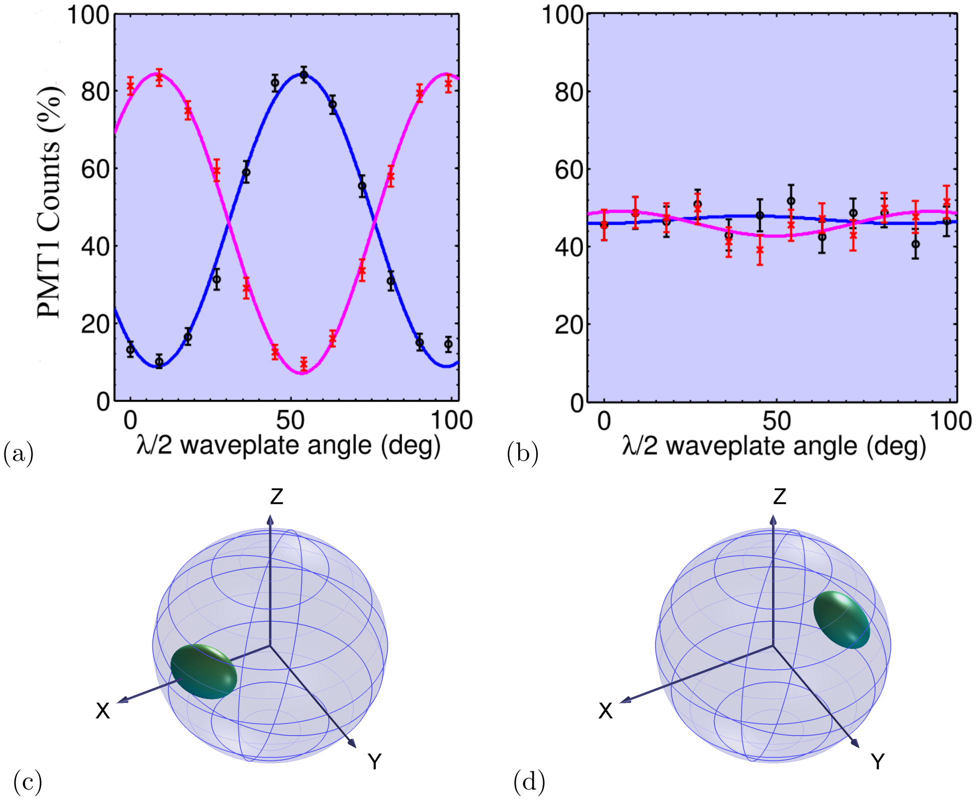

Figure 47: Spin measurement via photon polarization detection. Quarter-wave retardation plate is oriented such that the circular polarization of scattered photons is transformed into linear. The figures abscissa is the angle of the half-wave retardation plate, that is subsequently rotating the photon polarization direction with respect to that of the PBS. (a) The probability of detecting photons on one port of the PBS vs. the half-wave plate angle, when the spin is initialized to the $|\hat{x}\rangle$ (red filled circles) or $|-\hat{x}\rangle$ (black filled circles) pointer states. Solid lines are sinusoidal fit to the data. As seen, these spin states scatter circularly polarized photons. Furthermore, when the half-wave plate orients the photon polarization detection with the PBS basis, the two spin states can be discriminated with 75% fidelity. (b) Same as (a), only with the spin initialized in the $|\pm Y\rangle$ states. Starting in this spin state, the spin and photon become entangled. Photons arriving to the PBS therefore carry a statistical mixture of polarization states. The probability of a photon to be measured on a given port of the PBS is hence independent of rotations. Alternatively we performed QPT conditioned on the detection of right or left circularly polarized photons. The surface onto which the Bloch sphere collapses in these two cases is shown in (c) and (d), respectively. As expected, the Bloch sphere collapsed on the $|\hat{x}\rangle$ and $|-\hat{x}\rangle$ states.

the initial spin direction is found. Figure 47(b) presents similar data with the spin initialized to the $|\pm\hat{y}\rangle$ states ($|-\hat{y}\rangle = 1/\sqrt{2}(|\uparrow\rangle - i|\downarrow\rangle)$). As expected from a fully mixed polarization state, the photon detection probability on a given PBS port is independent of polarization rotation indicating a lack of classical correlation between the photon polarization state and the initial spin state. An alternative measurement is shown in which QPT was performed conditioned on the detection of right or left circularly polarized photons is shown in Fig. 47(c) and (d), respectively. It can be seen that on detection of right (left) circularly-polarized photon the initial Bloch sphere indeed collapsed to the $|\hat{x}\rangle$ ($|-\hat{x}\rangle$) state.

6.5 Atom-photon entanglemet

The post-scattering spin states entropy serves as a predictability sieve [26] for the scattered photons polarization states. Figure 47 shows an analysis of scattered photons polarization states for the four pre-scattering spin states $|\pm\hat{x}\rangle$,$|\pm\hat{y}\rangle$. In this analysis the $\lambda/4$ retardation plate was fixed to convert left and right circular polarization states to two linear orthogonal states. Measurements were taken by scattering photons while rotating the $\lambda/2$ retardation plate and monitoring, simultaneously, the PBS two output ports. In Fig. 47(a) it can be seen that initial $|\pm\hat{x}\rangle$ states scattered photons with predictable, and orthogonal, polarization states. In contradiction, no spin-photon correlation was found when photons that were scattered by initial spin states $|\pm\hat{y}\rangle$, in Fig. 47(b). For these states, the scattering process created mixed spin and the photon polarization states. The correlation between the scattered photons polarization state an the spin pre-scattering $|\pm\hat{x}\rangle$ states makes these states a measurement basis. This basis is also known as the system pointer basis [28]. A more comprehensive analysis of this basis emergence was achieved by preforming a two-qubit quantum state tomography (QST) over the spin and photon polarization post-scattering states. Figure 48 shows these two parties joint density matrices for the six different pre-scattering spin states $|\uparrow\rangle$, $|\downarrow\rangle$, $|\pm\hat{x}\rangle$ and $|\pm\hat{y}\rangle$. The initial spin states $|\pm\hat{x}\rangle$ resulted in almost separable density matrix which can be approximately written as a tensor product of the two parties pure states. The scattering process, for the rest of the spin initial states, resulted in non-sparable density matrices in which the two parties states were entangled. The post-scattering two parties degree of entanglement was evaluated by the concurrence monotone [59]. Figure 49 shows a map of post-scattering concurrence values projected on the spin corresponding pre-scattering states. This map was calculated by reconstructing arbitrary two parties post-scattering state based on the Fig.

48 measurements. Spin-photon states entanglement reached a maximal value of 0.75. This map is similar to the increase in entropy of spin state due to scattering which is presented in Fig. 42(d).

Starting with an initial spin state other than $|\pm\hat{x}\rangle$ we have seen that both the spin state and the photon polarization-state decohere into statistical mixtures. This decoherence is the result of spin-photon entanglement. To observe this entanglement we preformed quantum state tomography of the combined spin-photon state. Figures 48(a)-(f) present the reconstructed spin-photon density matrices for six different initial spin states, $|\uparrow\rangle$,$|\downarrow\rangle$,$|\pm\hat{x}\rangle$,$|\pm\hat{y}\rangle$. The density matrices are plotted using the $|\pm\hat{x}\rangle$ and $|E_{\pm}\rangle$ states as a basis. As seen, scattering events in which the spin was initialized along $\hat{x}$ have a single dominant entry on the diagonal and therefore represent approximately separable states. Alternatively, spin states that were initially oriented along the $\hat{y}$ or $\hat{z}$ directions, resulted in highly entangled states.

We quantified the amount of atom-photon entanglement using the concurrence entanglement monotone, $C(\rho)$ [59]. All atom-photon final density matrices were evaluated by linear combinations of the six reconstructed density matrices. Figure 49 presents a color map of the calculated concurrence values plotted on the Bloch sphere of initial spin states. As seen, the minimum entanglement (C $<$ 0.03) is along the $\hat{x}$ direction. The concurrence monotonically increases up to its maximum value of roughly 0.7 along the sphere circumference in the $\hat{y}\hat{z}$ plane, in consistence with the observed entropy increase shown in Fig. 42(d).

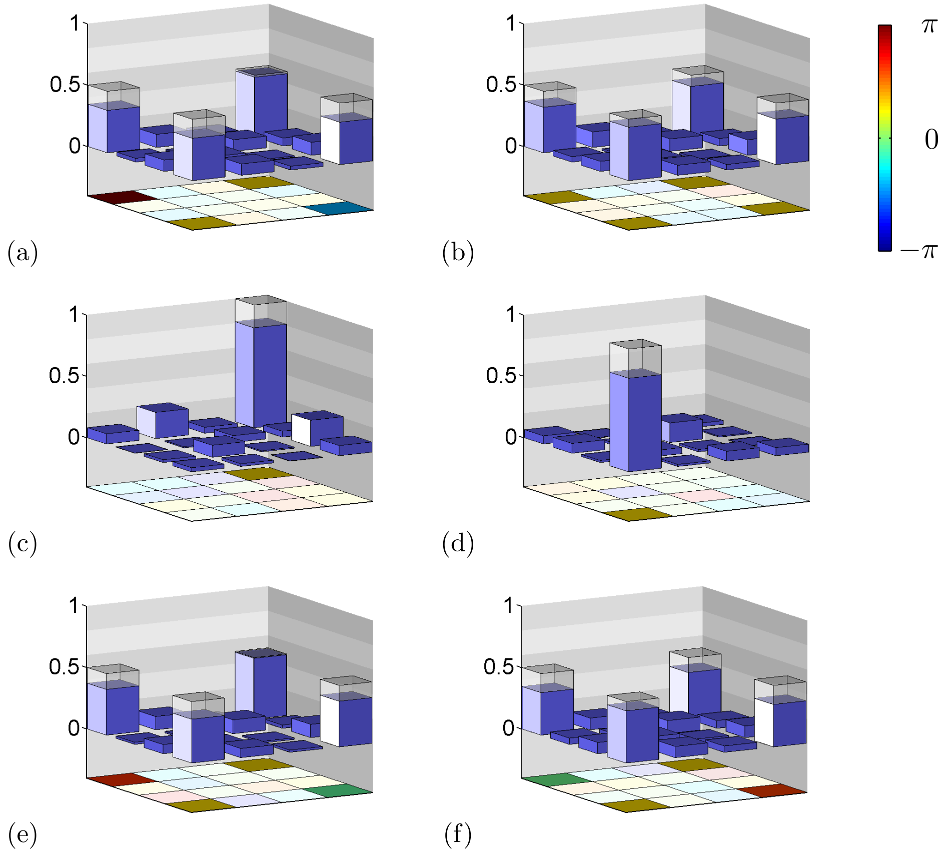

Figure 48: State tomography of spin-photon states. Centered around the collapsed spin ellipsoid are six reconstructed spin-photon density matrices. The different density matrices are post-scattering states where the spin was initialized in different initial direction. The different spin initial states are (starting from the top and clockwise) $|\uparrow\rangle$, $|-\hat{x}\rangle$, $|\hat{y}\rangle$, $|\downarrow\rangle$,$|\hat{x}\rangle$ and $|-\hat{y}\rangle$. The density matrices are written in the basis of product states of $|\pm\hat{x}\rangle$ and $|E_{\pm}\rangle$ spin and polarization states. The solid bars are absolute values of entries of the reconstructed density matrices whereas the transparent bars correspond to the values predicted by Eq.6.3.2. The phases of the different entries are represented by different colors bellow the bars and according to the color map on the right. As seen, the $|\pm\hat{x}\rangle$ pointer states have a single significant matrix element and therefore represent non-entangled states. States orthogonal to the pointer state basis are seen to be highly entangled with the scattered photon polarization.

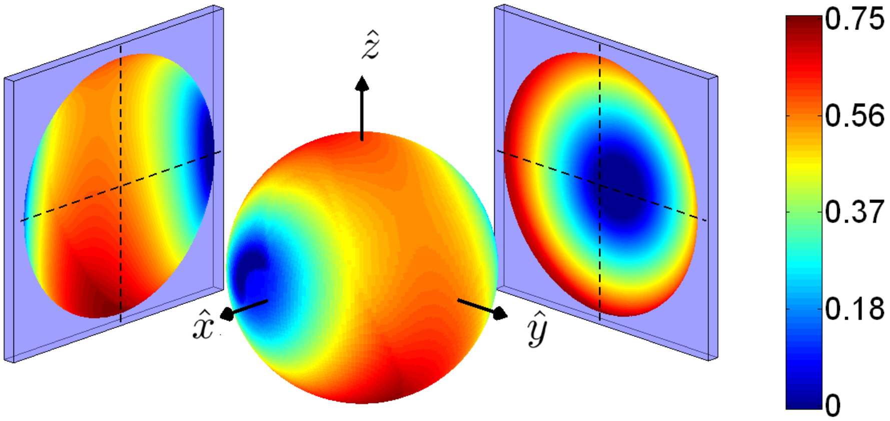

Figure 49: A color map of the measured concurrence of every post-scattering spin-photon state. The map is plotted on the Bloch sphere of all initial spin directions. Two projections of the sphere - on the $\hat{y}\hat{z}$ and $\hat{z}\hat{x}$ planes are shown as well. Pointer states along the $\hat{x}$ direction are seen to be minimally entangled with the scattered photon polarization.

7 Summary

In this work we have demonstrated coherent control of single trapped $^{88}\mathrm{Sr}^{+}$ ions. Ions were trapped by a linear Paul trap inside an ultra high vacuum chamber. An array of optical beams is used to photo-ionize neutral Sr atoms and to manipulate the electronic states of the trapped ions. Both optical and Zeeman qubits were encoded in the internal states of these trapped ions. The optical qubit was manipulated by a narrow line-width laser beam, the Zeeman qubit was manipulated by a rf fields that were resonant with the Zeeman splitting. Single qubit coherent operations such as Rabi oscillations and Ramsey interferometry were demonstrated for both qubit types. Qubits readout was preformed by resonance fluorescence where, for the Zeeman qubit case, readout was preceded by electron shelving of one of the qubit states to the ion metastable level. We also demonstrated resolved sideband cooling of the ions. following this cooling 95% of the ions population occupied the ground state of their center-of-mass vibration mode.

Two trapped ions internal states were entangled by a Sørensen-Mølmer (σ_ϕ) entangling gate. For the gate bus we used the two ions common stretch vibration mode. The qubits entangled population fraction was quantified by a parity scan of the qubits post-gate state. A gate entangling fidelity of 0.84 was measured for a gate time of 170 μsec. This fidelity was limited by frequency drifts of the entangling beam and fast phase noise which came with it. Removing this noise would contribute dramatically to the performance of the entangling gate.

An emergence of a measurement basis following photon scattering, by a single ion, was demonstrated. This basis states were unaffected by the scattering process. An entanglement between the photon polarization state and the qubit state was measured for pre-scattering spin states that are not aligned with this basis. By being resilient to spontaneous photon scattering, pointer states are resemble to stationary "dark state". The evolution of a quantum system. following its convergence to these states, stops. Therefore these states can span a DFS for encoding of quantum information. The establishment of such subspaces is an important contribution to the effort to preform quantum information processing.

8 Declaration

I declare that this thesis entitled ”Ion-Ion and Ion-Photon Entanglement in Trapped Ions System” is a record of the bonafide research work done by me under the supervision of Dr. Roee Ozeri, Senior Scientist, Department of Complex Physics, The Weizmann Institute of Science, Israel.

Yinnon Glickman

The Weizmann Institute of Science
August 28, 2012

A Quantum process tomography

Quantum process tomography (QPT) [58] is a method for characterization of quantum operations that are applied on a quantum system. Non-unitary operations are abstraction of an environment influence on a system to which it couples. Formally, these operations are expressed by a linear map of the system initial state to a final, post-process, state. Continuous interactions are treated, by this method, by examining the system states at several time instances. In section 6.1 it is the environment state which triggers the system post-process tomography. QPT extracts the investigated operation elements by probing the process with a known set of initial quantum states and analyzing, using quantum state tomography, the corresponding post-process final states. One can define an arbitrary basis in which the operation elements will be represented, however, spanning this basis by intuitive basic operations, like spin rotations and the identity operation, can give a clear insight on the physical mechanism behind the operation. The number of measurements that are required for full QPT scales as d^4, where, d is the system dimension ($d = 2N$ for a system which is composed of N TLS, like spins). This power law becomes very consuming when one deals with large systems. Several suggestions where raised for tackling this issue [60, 61] by measuring only critical operations of the process and estimating the rest.

A.1 QPT theory

The algebraic theory behind quantum operations and QPT is developed comprehensively in [58], part of it is given here. By the operator sum representation a process ε which is applied on an open quantum system can be described as a linear combination of operators

$$\varepsilon(\rho) = \sum_k E_k \rho E_k^\dagger, \tag{A.1.1}$$

where, ρ is the $d \times d$ density matrix which represents the system initial state. The operation elements E_k manifest the environment influence on the system, they are called Kraus operators and are normalized as $\sum_k E_k^\dagger E_k = I$. These operators are unknown to us, the system observers. The purpose of QPT is to estimate them using measurement. The Kraus operators can be spanned by an arbitrary basis of operations that spans the system Hilbert space. If $\tilde{E}_m$ is our chosen working basis, each of the operation elements can be written as

$$E_k = \sum_m e_{km} \tilde{E}_m, \tag{A.1.2}$$

where, e_{km} is the weight of each operator in the chosen basis in representing the kth operation element. Using this definition the process (A.1.1) can be rewritten, in our basis, for producing the post-process system density matrix ρ'

$$\rho' = \varepsilon(\rho) = \sum_{mn} \tilde{E}_m \rho \tilde{E}_n^\dagger \chi_{mn}. \tag{A.1.3}$$

The matrix χ_{mn} is called the process matrix, it is defined as $\chi_{mn} = \sum_i e_{im} e_{in}^*$. This matrix is an hermitian matrix which encapsulates all the process features, given that it is a trace preserving process. In QPT the process is probed with initial set of states ρ_j. By measuring the corresponding post-process final states ρ'_j one can reconstruct the process matrix χ. Both ρ_j and every $\{m, n\}$ combination of $\tilde{E}_m \rho \tilde{E}_n^\dagger$ can be spanned by another set of density matrices ρ_k that form a basis for the system state,

$$\begin{aligned} \rho'_j &= \sum_k \lambda_{jk} \rho_k, \\ \tilde{E}_m \rho_j \tilde{E}_n^\dagger &= \sum_k \beta_{jk}^{mn} \rho_k. \end{aligned} \tag{A.1.4}$$

This joint basis allows us to introduce these two equations

$$\sum_k \lambda_{jk} \rho_k = \rho'_j = \sum_k \sum_{mn} \chi_{mn} \beta_{jk}^{mn} \rho_k. \tag{A.1.5}$$

This expression can be simplified by introducing general indices p and q that accept the values $p, q = 0, 1, ..., (m \cdot n - 1)$. Each value of p and q stands for a single $\{m, n\}$ and $\{j, k\}$ combination, respectively. Therefore, for every k, equation (A.1.5) can be written as

$$\sum_p \beta_q^p \chi_p = \lambda_q. \tag{A.1.6}$$

The process matrix can be reconstructed by multiplying the inverse of β by the vector λ, i.e. $\chi_p = \sum_q (\beta_q^p)^{-1} \lambda_q$. To avoid singularity of β, which can arise from noisy measurements, one can use β generalized inverse instead of the regular inverse matrix for this calculation.

For determining a d dimensional process matrix one has to set $d^4 - d^2$ free parameters. For a cluster of N spins these parameters can be extracted by a probing the process with 4^N initial states that are all the combinations of the form

$$\rho = |s_1\rangle\langle s_1| \otimes |s_2\rangle\langle s_2| \otimes \cdots \otimes |s_N\rangle\langle s_N| \qquad |s_i\rangle \in \{|\uparrow\rangle, |\downarrow\rangle, |x\rangle, |y\rangle\}. \tag{A.1.7}$$

Each system final state, which is the post-process state of every one of these initial states, has to be read after being rotated by 3^N rotations groups. These rotations groups are all the permutations of the form

$$R = R_i^1(\pi/2) \cdot R_i^2(\pi/2) \cdots R_i^N(\pi/2), \tag{A.1.8}$$

where $i \in \{x, y, z\}$ and R_i^j stands for rotation operator around the i axis of the j^{th} spin. It takes 4 (16) systems initial states that are post-processes measured after 3 (9) rotations for QPT of one (two) qubit.

A.2 Optical pumping QPT

A single qubit QPT was demonstrated for the optical pumping process. A Zeeman qubit was initialized to the $|\uparrow\rangle$, $|\downarrow\rangle$, $|X\rangle$ and $|Y\rangle$ states before being exposed to the optical pumping σ^+ beam. For different exposure times, between 0 to 50 μsec, a QST was preformed on the qubit. Figure 50 shows the optical pumping process matrices foe 6 instances of the process. The process matrices are given in the "rotations" basis where $E_1 = I$, $E_2 = \sigma_x$, $E_3 = -i\sigma_y$ and $E_4 = \sigma_z$. Given the process which lead to each instance system state it was numerically applied on initial pure states that cover the Bloch sphere. Beside each process matrix in Fig. 50 one can see the equivalent state of the Bloch sphere which collapses due to optical pumping induced projection of all system states to the $|\uparrow\rangle$ state.

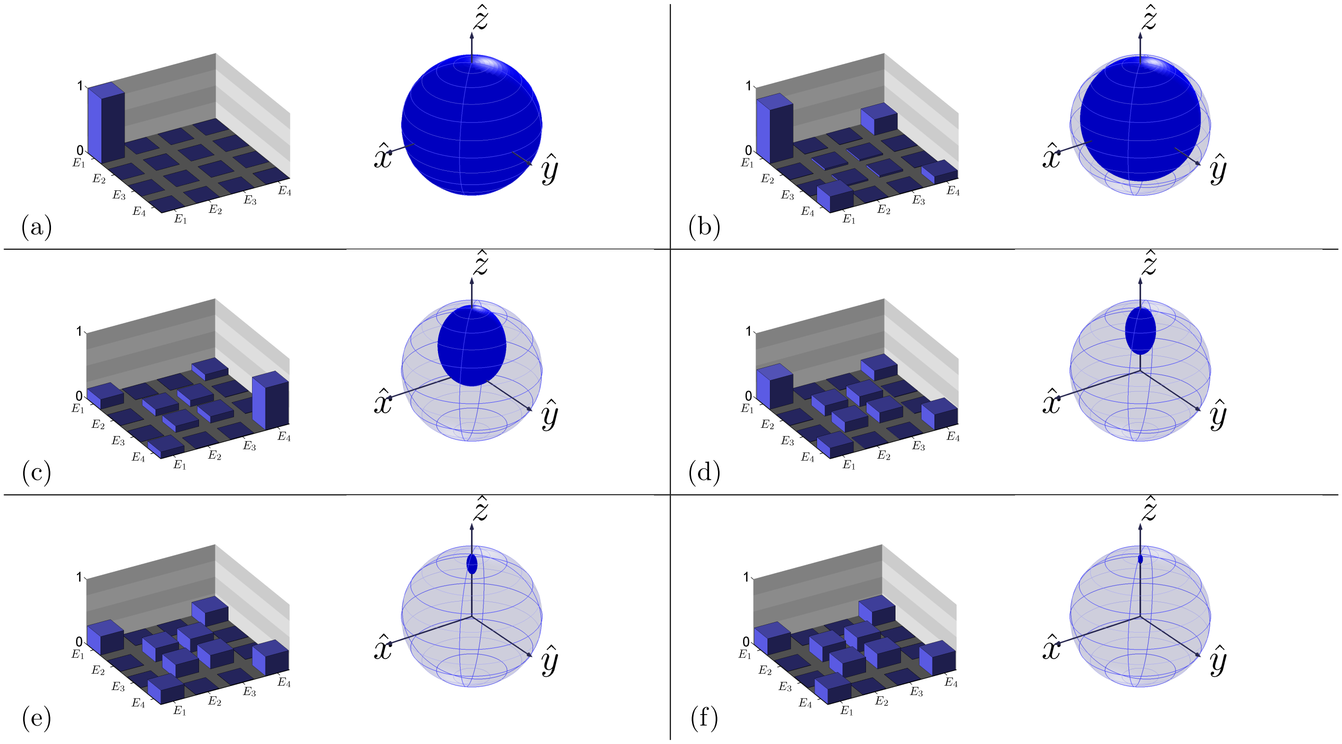

Figure 50: QPT of a qubit Bloch sphere dynamics under optical pumping. Snapshots are taken after an optical pumping time of (a) 0, (b) 2, (c) 10, (d) 20, (e) 35 and (f) 50vμsec. Note that before the optical pumping beam was introduced, in (a), no process was applied on the system and therefore the equivalent process includes only unity operation elements. The process matrices are given in the basis $E_1 = I$, $E_2 = \sigma_x$, $E_3 = -i\sigma_y$ and $E_4 = \sigma_z$.

References

[1] R. C. Thompson, *Spectroscopy of trapped ions*, Adv. Atom. Mol. Opt. Phys. 31, 63 (1993).

[2] W. Paul, *Electromagnetic traps for charged and neutral particles*, Rev. Mod. Phys. 62 531 (1990).

[3] H. Dehmelt. *Radiofrequency spectroscopy of stored ions*, Adv. Atom. Mol. Opt. Phys. 3, 53 (1967).

[4] D. J. Wineland, H. G. Dehmelt, Bull. Am. Phys. Soc. 20, 637 (1975).

[5] D. J. Wineland, R. E. Drullinger, F. L. Walls, Phys. Rev. Lett. 40, 1639 (1978).

[6] K. Toyoda, H. Naka, H. Kitamura, H. Sawamura, S. Urabe, *Sideband-resolved spectroscopy on the* $4^2S_{1/2}$-$3^2D_{5/2}$ *transition in single calcium ions by use of fundamental waves of diode lasers*,Opt. Lett. 29, 11, 1270 (2004).

[7] F. Diedrich, J. C. Bergquist, W. M. Itano, D. J. Wineland, *Laser Cooling to the Zero-Point Energy of Motion*, Phys. Rev. Lett. 62, 403 (1989).

[8] C. Monroe, D. M. Meekhof, B. E. King, S. R. Jefferts, W. M. Itano, D. J. Wineland, P. Gould, *Resolved-Sideband Raman Cooling of a Bound Atom to the 3D Zero-Point Energy*, Phys. Rev. Lett. 75, 4011 (1995).

[9] W. Nagourney, J. Sandberg, H. G. Dehmelt, *Shelved Optical Electron Amplifier: Observation of Quantum Jumps*, Phys. Rev. Lett. 56, 2797 (1986).

[10] T. Sauter, W. Neuhauser, R. Blatt, P. E. Toschek, *Observation of Quantum Jumps*, Phys. Rev. Lett. 57, 1696 (1986).

[11] J. C. Bergquist, R. G .Hulet, W. M. Itano, D. J. Wineland, *Observation of Quantum Jumps in a Single Atom*, Phys. Rev. Lett. 57, 1699 (1986).

[12] P. W. Shor, in *Proceedings of the 35th Annual Symposium on Foundations of Computer Science*, S. Goldwasser, Ed. (IEEE Computer Society, Los Alamitos, CA, 1994), p. 116.

[13] L. K. Grover, *Quantum mechanics helps in searching for a needle in a haystack*, Phys.Rev. Lett. 79, 325 (1997).

[14] D. S. Abrams, S. Lloyd, *Simulation of many-body Fermi systems on a universal quantum computer*, Phy. Rev. Lett. 79, 2586 (1997). arXiv:quant-ph/9703054.

[15] D. P. DiVincenzo, *The physical implementation of quantum computation*, arXiv:quant-ph/0002077 (2000).

[16] A. Barenco, C. H. Bennett, R. Cleve, D. P. DiVincenzo, N. Margolus, P. Shor, T. Sleator, J. A. Smolin, H. Weinfurter, *Elementary gates for quantum computation*, Phys. Rev. A, 53, 5, 3457 (1995).

[17] L. Allen, J. H. Eberly, *Optical Resonance and Two-Level Atoms*, Dover: New York (1987).

[18] J. I. Cirac, P. Zoller, *Quantum computation wiht cold trapped ions*, Phys. Rev. Lett., 74, 4091 (1995).

[19] A. Sørensen, K. Mølmer, *Quantum computation with ions in thermal motion*, Phys. Rev. Lett. 82, 9, 1971 (1999).

[20] F. S. Kaler, H. Haffner, M. Riebe, S. Gulde, G. P. T. Lancaster, T. Deuschle, C. Becher, C. F. Roos, J, Eschner, R. Blatt, *Realization of the CiracZoller controlled-NOT quantum gate*, Nature, 422, 408 (2003).

[21] C. A. Sackett, D. Kielpinski, B. E. King, C. Langer, V. Meyer, C.J. Myatt, M. Rowe, Q. A. Turchette, W. M. Itano, D. J. Wineland, C. Monroe, *Experimental entanglement of four particles*, Nature 404, 256 (2000).

[22] J. Benhelm, G. Kirchmair, C. F. Roos, R. Blatt, *Towards fault-tolerant quantum computing with trapped ions*, Nat. Phys., doi:10.1038/nphys961 (2008).

[23] W. K. Hensinger,S. Olmschenk, D. Stick, D. Hucul, M. Yeo, M. Acton,L. Deslauriers, C. Monroe, *T-junction ion trap array for two-dimensional ion shuttling, storage, and manipulation*, Appl. Phys. Lett., 88, 034101 (2006).

[24] Q. A. Turchette, D. Kielpinski, B. E. King, D. Leibfried, D. M. Meekhof, C. J. Myatt, M. A. Rowe, C. A. Sackett, C. S. Wood, W. M. Itano, C. Monroe, D. J. Wineland, *Heating of trapped ions from the quantum ground state*, Phys. Rev. A, 61, 063418 (2000).

[25] M. Barrett, B. L. DeMarco, T. Schaetz, V. Meyer, D. Leibfried, J. Britton, J. Chiaverini, W. M. Itano, B. M. Jelenkovic, J. D. Jost, C. Langer, T. Rosenband,D. J. Wineland, *Sympathetic cooling of 9Be+ and 24Mg+ for quantum logic*, Phys. Rev. A 68, 042302-1 - 042302-7 (2003).

[26] W. H. Zurek, *Decoherence, einselection, and the quantum origins of the classical*, Rev. Mod. Phys. 75, 715 (2003).

[27] M. Brune, E. Hagley, J. Dreyer, X. Matre, A. Maali, C. Wunderlich, J. M. Raimond, S. Haroche, *Observing the Progressive Decoherence of the "Meter" in a Quantum Measurement*, Phys. Rev. Lett. 77, 4887 (1996).

[28] W. H. Zurek, *Pointer basis of quantum apparatus: Into what mixture does the wave packet collapse*, Phys. Rev. D 24, 1516 (1981).

[29] D. Kielpinski, V. Meyer, M. A. Rowe, C. A. Sackett, W. M. Itano, C. Monroe, D. J. Wineland, *A Decoherence-Free Quantum Memory Using Trapped Ions*, Science 291, 1013 (2001).

[30] C. Langer, R. Ozeri, J. D. Jost, J. Chiaverini, B. DeMarco, A. Ben-Kish , R. B. Blakestad, J. Britton, D. B. Hume, W. M. Itano, D. Leibfried, R. Reichle, T. Rosenband, T. Schaetz, P. O. Schmidt, D. J. Wineland, *Long-Lived Qubit Memory Using Atomic Ions*, Phys. Rev. Lett. 95, 060502 (2005).

[31] D. W. Jordan, P. Smith, *Nonlinear ordinary differential equations*, Oxford, Great Clarendon Street, Oxford (1999).

[32] P. K. Ghosh, *Ion traps*, Clarendon Press (1995).

[33] C. F. Ross, *Ph.D. Thesis - Controlling the quantum state of trapped ions*, der Leopold-Franzens-Universität Innsbruk (2000).

[34] C. Cohen-Tannoudji, *Atomic motion in laser light.* In *Foundamental system in quantum optics*, Les Houches, Session LIII. Elsevier Publishers (1990).

[35] D. J. Wineland, W. M. Itano, *Laser cooling of atoms*, Phys. Rev. A, 20, 1521 (1979).

[36] S. Stenholm, *The semiclassical theory of laser cooling*, Rev. Mod. Phys. 58, 699 (1986).

[37] N. Akerman, S. Kotler, Y. Glickman, A. Keselman, R. Ozeri, *Quantum control of* $^{88}Sr^{+}$ *in a miniature linear Paul trap*, App. Phys. B 107, 4, 1167 (2012). DOI: 10.1007/s00340-011-4807-6.

[38] N. Akerman, S. Kotler, Y. Glickman, Y. Dallal, A. Keselman, R. Ozeri, *Single-ion nonlinear mechanical oscillator*, Phys. Rev. A 82, 061402 (2010).

[39] W. Alt, arXiv:physics/0108058v1 (2001).

[40] K. Vant, J. Chiaverini, W. Lybarger, D. J. Berkeland, arXiv:quant-ph/0607055 v1 (2006).

[41] E. D. Black, *An introduction to Pound-Drever-Hall laser frequency stabilization*, Am. Jour. Phys. 20, 1, 87, DOI: 10.1119/1.1286663 (2001).

[42] A. A. Madej, L. Marmet, J.E. Bernard, *Rb atomic absorption line reference for single* Sr^{+} *laser cooling systems*, Appl. Phys. B 67, 229 (1998).

[43] A. G. Sinclair, M. A. Wilson, P. Gill, *Improved three-dimensional control of a single strontium ion in an endcap trap*,Opt. Comm. 190, 193 (2001).

[44] A. Kesselman, *Ph.D. Thesis - High fidelity ion qubit state detection.* The Weizmann Institue of Science (2009).

[45] H. Dehmelt, *Proposed* 10^{14} $\Delta\nu > \nu$ *laser fluorescence spectroscopy on* Ti^{+} *mono-ion osclillator II*, Bull. Am. Phys. Soc. 20, 60 (1975).

[46] A. Kesselman, Y. Glickman, N. Akerman, S. Kotler, R. Ozeri, *High-fidelity state detection and tomography of a single-ion Zeeman qubit* (2011), NJP, doi:10.1088/1367-2630/13/7/073027.

[47] D.F. V. James, *Quantum dynamics of cold trapped ions with application to quantum computation*, App. Phys. B 66, 181?190, (1998).

[48] C. W. Chou, D. B. Hume, M. J. Thorpe, D. J. Wineland, T. Rosenband, *Quantum coherence between two atoms beyond* $Q = 10^{1}5$,Phys. Rev. Lett. 106, 160801 (2011).

[49] G. S. Agarwal, *Quantum statistical theory of optical-resonance phenomena in fluctuating laser fields*, Phys. Rev. A 18, 4, 1940 (1978).

[50] F. Diedrich, J. C. Bergquist, W. M. Itano, D. J. Wineland, *Laser Cooling to the Zero-Point Energy of Motion*, Phys. Rev. Lett. 62, 403 (1989).

[51] S. Kotler, N. Akerman, Y. Glickman, A. Keselman, R. Ozeri, *Single-ion quantum lock-in amplifier*, Nature 473, 61 (2011).

[52] A. Sørensen, K. Mølmer, *Entanglement and quantum computation with ions in thermal motion*, PRA 62, 022311 (2000).

[53] G. Kirchmair, J. Benhelm, F. Zhringer, R. Gerritsma, C. F. Roos, R. Blatt *Deterministic entanglement of ions in thermal states of motion*, NJP, 11 023002 (2009), doi:10.1088/1367-2630/11/2/023002.

[54] C. F. Roos, *Ion trap quantum gates with amplitude-modulated laser beams*, NJP 10, 013002 (2008), doi:10.1088/1367-2630/10/1/013002.

[55] P. J. Lee, K-A Brickman, L. Deslauriers, P. C. Haljan, L-M Duan, C. Monroe, *Phase control of trapped ion quantum gates*, J. Opt. B 7, S371 (2005).

[56] D. F. V. James, P. G. Kwiat, W. J. Munro, A. G. White, *Measurement of qubits*, PRA 64, 052312 (2001), DOI: 10.1103/PhysRevA.64.052312.

[57] N. Akerman, S. Kotler, Y. Glickman, R. Ozeri, *Quantum correction of photon-scattering errors* arXiv:1111.1622 (2011).

[58] M. A. Nielsen, I. L. Chuang, *Quantum Computation and Quantum Information*, Cambridge University Press (2000).

[59] M. B. Plenio, S. Virmani, *An introduction to entanglement measures*, Quant. Inf. Comput. 7, 1 (2007).

[60] A. Shabani, R. L. Kosut, M. Mohseni, H. Rabitz,M. A. Broome, M.P. Almeida, A. Fedrizzi, A. G. White, *Efficient Measurement of Quantum Dynamics via Compressive Sensing*, Phys. Rev. Lett. 106, 100401 (2011).

[61] M. P. A. Branderhorst, J. Nunn, I. A. Walmsley, R. L. Kosut, *Simplified quantum process tomography*, NJP 11, 115010 (2009).